

LBNL-43276

UCB-PTH-99/22

Big-Bang Nucleosynthesis with High-Energy Photon Injection

by

Erich Nielsen Holtmann

B.A. (University of California, Berkeley) 1992

M.A. (University of California, Berkeley) 1994

A dissertation submitted in partial satisfaction of the

requirements for the degree of

Doctor of Philosophy

in

Physics

in the

GRADUATE DIVISION

of the

UNIVERSITY OF CALIFORNIA, BERKELEY

Committee in charge:

Professor Mary K. Gaillard, Chair

Professor Hitoshi Murayama

Professor James Graham

Spring 1999

The dissertation of Erich Nielsen Holtmann is approved:

Chair

Date

Date

Date

University of California, Berkeley

Spring 1999

Big-Bang Nucleosynthesis with High-Energy Photon Injection

©1999

by

Erich Nielsen Holtmann

Abstract

Big-Bang Nucleosynthesis with High-Energy Photon Injection

by

Erich Nielsen Holtmann

Doctor of Philosophy in Physics

University of California, Berkeley

Professor Mary K. Gaillard, Chair

The theory of big-bang nucleosynthesis (BBN) is one of the most important predictions of the union of Friedmann-Robertson-Walker (FRW) cosmology with the Standard Model of elementary particle physics. Historically, BBN has enjoyed success in predicting the primordial abundances of the light elements; however, recent improvements in the observations of these elements (some of which appear to conflict with the predictions of standard BBN) have rekindled interest in non-standard scenarios of BBN. In my dissertation, I consider the effects of long-lived, radiatively decaying particles on BBN neglecting the hadronic branching ratio of these particles. The high-energy photons emitted in the decays of these particles may photodissociate the light elements that were synthesized during BBN. By comparing the resulting theoretical light-element abundances to the primordial abundances deduced from observation, I derive constraints on the properties

of long-lived, radiatively decaying particles. Taking into account the recent controversies regarding the observations of the light-element abundances, I perform my analysis for various combinations of the measurements. I also discuss several models that predict such radiatively decaying particles, and I derive constraints on such models.

To Andrew

Contents

1	Introduction	1
1.1	Summary of FRW Cosmology and Thermodynamics	4
1.2	Summary of Standard Big-Bang Nucleosynthesis	11
1.3	History of BBN Theory	18
2	X-Decay and Photon Injection	24
2.1	Photon Spectrum	25
2.2	Resulting Abundances	27
2.3	Uncertainties and Linear Propagation of Error	31
3	Observed Light-Element Abundances	42
3.1	D/H in Quasar Absorption Systems	43
3.2	^4He	44
3.3	$\log(^7\text{Li}/\text{H})$	46
3.4	$\log(^6\text{Li}/\text{H})$	47
4	Statistical Analysis of Theory and Observation	49
4.1	Analysis	49
4.2	Results	52
4.3	Additional Constraints	58

5	Analysis Based on Proto-Solar Observations	74
5.1	Proto-Solar Data on $(D+{}^3\text{He})/\text{H}$ and ${}^3\text{He}/\text{H}$	75
5.2	Proto-Solar Analysis	76
5.3	Results	79
6	Models	90
6.1	Gravitino	90
6.2	Bino	92
6.3	Modulus	95
7	Conclusion	105

List of Figures

1.1	SBBN prediction of the abundances of the light elements, as functions of time, for $\eta = 3 \times 10^{-10}$	16
1.2	SBBN prediction of the abundances of the light elements. The solid lines are the central values of the predictions, and the dotted lines represent the one- σ uncertainties. The boxes and lines with arrows denote the one- σ observational constraints. The gray box indicates $(D+{}^3\text{He})/\text{H}$; the black boxes in the second panel indicate D/H	23
2.1	Photon spectrum $f_\gamma = dn_\gamma/dE_\gamma$ for several background temperatures T_γ^{BG}	36
2.2	Abundance of D in the $m_X Y_X$ vs. τ_X plane with (a) $\eta = 2 \times 10^{-10}$, (b) $\eta = 4 \times 10^{-10}$, (c) $\eta = 5 \times 10^{-10}$, and (d) $\eta = 6 \times 10^{-10}$	37
2.3	Same as Fig. 2.2, except for ${}^3\text{He}$	38
2.4	Same as Fig. 2.2, except for ${}^4\text{He}$	39
2.5	Same as Fig. 2.2, except for ${}^6\text{Li}$	40
2.6	Same as Fig. 2.2, except for ${}^7\text{Li}$	41

4.1	C.L. in the $m_X Y_X$ vs. τ_X plane, for low value of ${}^4\text{He}$ and low value of D/H. I take (a) $\eta = 2 \times 10^{-10}$, (b) $\eta = 4 \times 10^{-10}$, (c) $\eta = 5 \times 10^{-10}$, and (d) $\eta = 6 \times 10^{-10}$. The shaded regions are $y_6/y_7 \gtrsim 0.5$, and the darker shaded regions are $y_6/y_7 \gtrsim 1.3$	61
4.2	C.L. in the $m_X Y_X$ vs. η plane for various values of τ_X , for low value of ${}^4\text{He}$ and low value of D/H.	62
4.3	Contours of C.L. projected along the η axis, for low value of ${}^4\text{He}$ and low value of D/H.	63
4.4	Predicted abundances of ${}^4\text{He}$, D/H, ${}^7\text{Li}/\text{H}$ and ${}^6\text{Li}/\text{H}$ at $\tau_X = 10^6$ sec and $m_X Y_X = 5 \times 10^{-10}$ GeV. I have indicated the regions that are favored by the low ${}^4\text{He}$ and low D/H observations. The dotted line denotes the 95% C.L., and the shaded region denotes the 68% C.L. The predicted ${}^6\text{Li}$ abundance is two orders of magnitude larger than it is in SBBN.	64
4.5	Same as Fig. 4.1, except for low value of ${}^4\text{He}$ and high value of D/H. . .	65
4.6	Same as Fig. 4.2, except for low value of ${}^4\text{He}$ and high value of D/H. . .	66
4.7	Same as Fig. 4.3, except for low value of ${}^4\text{He}$ and high value D/H. . . .	67
4.8	Same as Fig. 4.1, except for high value of ${}^4\text{He}$ and low value of D/H. . .	68
4.9	Same as Fig. 4.2, except for high value of ${}^4\text{He}$ and low value of D/H. . .	69
4.10	Same as Fig. 4.3, except for high value of ${}^4\text{He}$ and low value of D/H. . .	70
4.11	Same as Fig. 4.1, except for high value of ${}^4\text{He}$ and high value of D/H. . .	71
4.12	Same as Fig. 4.2, except for high value of ${}^4\text{He}$ and high value of D/H. . .	72

4.13	Same as Fig. 4.3, except for high value of ${}^4\text{He}$ and high value of D/H .	73
5.1	95% C.L. in the $m_X Y_X$ vs. τ_X plane, for low value of ${}^4\text{He}$, and proto-solar $(\text{D}+{}^3\text{He})/\text{H}$ and ${}^3\text{He}/\text{H}$. The allowed regions lie (a) inside the contours, and (b,c) below and to the left of the contours. I take (a) $\eta = 2 \times 10^{-10}$, (b) $\eta = 4 \times 10^{-10}$, (c) $\eta = 5 \times 10^{-10}$, and (d) $\eta = 6 \times 10^{-10}$. The shaded regions are $y_6/y_7 \gtrsim 0.5$, and the darker shaded regions are $y_6/y_7 \gtrsim 1.3$.	84
5.2	95% C.L. in the $m_X Y_X$ vs. η plane for various values of τ_X , for low value of ${}^4\text{He}$, and proto-solar $(\text{D}+{}^3\text{He})/\text{H}$ and ${}^3\text{He}/\text{H}$. The allowed regions lie within the contours.	85
5.3	95% C.L. contour projected along the η axis, for low value of ${}^4\text{He}$, and proto-solar $(\text{D}+{}^3\text{He})/\text{H}$ and ${}^3\text{He}/\text{H}$. The allowed region lies below and to the left of the contour.	86
5.4	Same as Fig. 5.1, except for high value of ${}^4\text{He}$. The solid line is the 95% C.L.; the dotted line is the 68% C.L.	87
5.5	Same as Fig. 5.2, except for high value of ${}^4\text{He}$. The solid line is the 95% C.L.; the dotted line is the 68% C.L.	88
5.6	Same as Fig. 5.3, except for high value of ${}^4\text{He}$. The solid line is the 95% C.L.; the dotted line is the 68% C.L.	89

6.1	Contours of 95% C.L., yielding an upper bound on the reheating temperature, as a function of the gravitino mass. QAS data are used for the observed D/H ratio.	99
6.2	Contours of 95% C.L., yielding an upper bound on the reheating temperature, as a function of the gravitino mass. Proto-solar data are used for the observed D/H and (D+ ³ He)/H ratios.	100
6.3	Contours of 95% C.L., yielding an upper bound on the gravitino mass, as a function of the right-handed slepton mass. QAS data are used for the observed D/H ratio.	101
6.4	Contours of 95% C.L., yielding an upper bound on the gravitino mass, as a function of the right-handed slepton mass. Proto-solar data are used for the observed D/H and (D+ ³ He)/H ratios.	102
6.5	Contours of 95% C.L., yielding an upper bound on the the initial modulus amplitude ϕ_0 , as a function of the modulus mass. QAS data are used for the observed D/H ratio.	103
6.6	Contours of 95% C.L., yielding an upper bound on the the initial modulus amplitude ϕ_0 , as a function of the modulus mass. Proto-solar data are used for the observed D/H and (D+ ³ He)/H ratios.	104

List of Tables

1.1	The nuclear reactions responsible for the synthesis of the light elements. Uncertainties are given for the twelve most important reactions [25, 22].	22
2.1	The binding energies of some light nuclides AZ .	25
2.2	Photodissociation processes, and the one- σ uncertainty in the cross sections. Since there are no experimental data on photodissociation of ${}^7\text{Be}$, I assume in this dissertation that the rate of Reaction 13 is the same as that of Reaction 11, and that the rate of Reaction 14 is the sum of the rates of Reactions 10 and 12.	28
4.1	Upper or (lower – upper) bound on $m_X Y_X$ in units of GeV for the case of low ${}^4\text{He}$ and low D/H. Note that the C.L. is for three degrees of freedom, and η is varied to give the extreme values for $m_X Y_X$.	55
4.2	Same as Table 4.1, except for low ${}^4\text{He}$ and high D/H.	56
4.3	Same as Table 4.1, except for high ${}^4\text{He}$ and low D/H.	57
4.4	Same as Table 4.1, except for high ${}^4\text{He}$ and high D/H.	58
5.1	Upper bound on $m_X Y_X$ in units of GeV for the case of low value of ${}^4\text{He}$, and proto-solar $(\text{D}+{}^3\text{He})/\text{H}$ and ${}^3\text{He}/\text{H}$. Note that the C.L. is for four degrees of freedom, and η is varied to give the maximum values for $m_X Y_X$.	81

5.2	Same as Table 5.1, except for high ^4He	82
-----	--	----

Acknowledgements

I would like to express my sincere gratitude to my advisor, Professor Mary K. Gaillard, for her help and support. I appreciate the freedom she gave me in choosing research topics. I would like to thank Dr. Takeo Moroi for many wonderful collaborations and discussions. I would also like to thank Kazunori Kohri and Dr. Masahiro Kawasaki for collaborating with me and cross-checking my work. I would like to acknowledge Physical Review D, which refereed much of this work, and will soon publish a portion of this thesis as Ref. [35]. I am grateful to Anne Takizawa and Donna Sakima of the physics department at U.C. Berkeley, and Luanne Neumann, Barbara Gordon, and Mary Kihanya at LBNL for help with administrative work.

Finally, but not least, I would like to thank Andrew Utiger for his loving support and encouragement.

Chapter 1

Introduction

Since it was first proposed by Gamow [1], big-bang nucleosynthesis (BBN) has become an important test of both the Standard Model (SM) of particle physics, and of the standard Friedmann-Robertson-Walker (FRW) cosmology. Currently, BBN provides a more precise test of the FRW big-bang cosmology than either measurements of the Cosmic Microwave Background Radiation (CMBR) [2], or direct measurements of the expansion of the universe [3].

Although BBN takes place at a temperature of about 1 MeV, it can be used to place constraints on physics at much higher energy scales. BBN currently gives the most precise determination of η , the ratio of baryons to photons. Thus, BBN constrains baryogenesis, which may take place at the Grand Unified scale ($\sim 10^{14}$ GeV).

BBN also sets constraints on exotic particles. One of BBN's more famous results is that N_ν , the number of light fermionic degrees of freedom during BBN, is equal to three, with a very small error. This suggests that there is not a fourth generation of fermions.¹ Because nucleosynthesis depends sensitively upon the

¹At present, the most precise determination of N_ν , *viz.*, 2.993 ± 0.011 , comes from measurements of the Z boson width in e^+e^- colliders [4]. Based on recent astronomical data, however, paradoxical statements have been made, such as, “ N_ν must be less than 2.” In this dissertation,

particle content of the big-bang plasma, BBN can also be used to place severe constraints upon the number density of heavy, non-relativistic particles, such as monopoles, gravitinos, and moduli. This endeavor has a long history [5].

In this thesis, I shall use BBN to set constraints on a specific class of exotic particles: massive ($\sim O(100 \text{ GeV})$), long-lived ($\sim 10^6 \text{ sec}$) particles that interact with other particles only very weakly (*e.g.*, through gravitation). I explore the possibility that BBN with these particles could agree with observations better than standard BBN.

These particles have lifetimes so long that they decay after the BBN of the light elements (D, ^3He , ^4He , etc.), so they and their decay products may affect the thermal history of the universe. In particular, if the long-lived particles decay into photons, then the emitted high-energy photons induce electromagnetic cascades and produce many soft photons. If the energy of these photons exceeds the binding energies of the light nuclides, then photodissociation may profoundly alter the light element abundances. Thus, I can impose constraints on the abundance and lifetime of long-lived particles, by considering the photodissociation processes induced by its decay. There are many works on this subject, such as the constraints on massive neutrinos and gravitinos obtained by the comparison between the theoretical predictions for and the observations [6, 7, 8, 9, 10] of the light-element abundances.²

I will consider these data and provide another interpretation.

²As pointed out in Ref. [11], even if the parent particle decays only into photons, these photons will produce hadrons with a branching ratio of at least 1%. However, since there are no data

In my thesis, I go beyond previous works in several ways:

1. I use more recent data for the light-element abundances and for the neutron lifetime;
2. I use a statistical analysis (proposed by Steigman and Tosi [12]) to include the abundance of ^3He in my constraints in a manner insensitive to the considerable uncertainty in the chemical evolution of ^3He ;
3. I present my results in terms of a well-defined confidence level (C.L.), thus avoiding the paradoxical statements that have plagued some previous works;
4. I include the uncertainties in the light-element abundances due to the uncertainties in the nuclear reaction rates;
5. I perform an analysis including the correlations in the light-element abundances as the nuclear reaction rates are varied. I compare this analysis to a more usual analysis in which such correlations are neglected;
6. I include the photodissociations of ^7Li and ^6Li . As I will show later, the destruction of ^7Li does not dramatically affect the predicted D and ^4He , in the region where the observed D and ^4He values are best fit. However, the ^6Li produced by the destruction of ^7Li can be two orders of magnitude

on some crucial cross sections involving ^7Li and ^7Be , I cannot include hadrodissociation in my statistical analysis. Since I have neglected hadrodissociation, my constraints may be regarded as conservative bounds.

more abundant than the standard BBN prediction of ${}^6\text{Li}/\text{H} \sim O(10^{-12})$.

I discuss the possibility that this process may be the origin of the ${}^6\text{Li}$ that is observed in some low-metallicity halo stars.

In the next section of the introduction, I review the cosmology and thermodynamics I use to simulate big-bang nucleosynthesis. After that, I discuss the standard theory of BBN (SBBN). Finally, I recount the history of SBBN and I review some non-standard extensions to SBBN.

1.1 Summary of FRW Cosmology and Thermodynamics

Since BBN is an inevitable consequence of FRW “big-bang” cosmology, I will first summarize this model [13]. The assumption that the universe is homogeneous and isotropic leads one to the Robertson-Walker metric:

$$d\tau^2 = dt^2 - a^2(t) \left[\frac{dr^2}{1 - kr^2} + r^2 d\theta^2 + r^2 \sin^2 \theta d\phi^2 \right]. \quad (1.1)$$

The parameter k is equal to $+1, 0$, and -1 in closed, flat, and open universes, respectively. The function $a(t)$ is the scale factor of the universe. To find the time evolution of the scale factor, one must assume an energy-stress tensor $T^\mu{}_\nu$ for the universe and use Einstein’s equations:

$$R^\mu{}_\nu - \frac{1}{2} R^\lambda{}_\lambda g^\mu{}_\nu = T^\mu{}_\nu / M_*^2 + \Lambda g^\mu{}_\nu, \quad (1.2)$$

where $M_* = 1/\sqrt{8\pi G} \simeq 2.4 \times 10^{18}$ GeV is the reduced Planck mass. Λ is the cosmological constant; it is equivalent to a vacuum energy density. In terms of

the scale factor a , the Ricci tensor is

$$R^\mu{}_\nu = \begin{bmatrix} -3\frac{\ddot{a}}{a} & 0 & 0 & 0 \\ 0 & -\frac{\ddot{a}}{a} - 2\frac{\dot{a}^2}{a^2} - 2\frac{k}{a^2} & 0 & 0 \\ 0 & 0 & -\frac{\ddot{a}}{a} - 2\frac{\dot{a}^2}{a^2} - 2\frac{k}{a^2} & 0 \\ 0 & 0 & 0 & -\frac{\ddot{a}}{a} - 2\frac{\dot{a}^2}{a^2} - 2\frac{k}{a^2} \end{bmatrix}. \quad (1.3)$$

I will assume that the universe behaves as a perfect fluid with energy density ρ and pressure p :

$$T^\mu{}_\nu = \text{diag}(\rho, -p, -p, -p), \quad (1.4)$$

This is consistent with the assumptions of a homogeneous, isotropic universe. (Note: I absorb the cosmological constant Λ into a contribution to $T^\mu{}_\nu$ of the form $\rho = \Lambda M_*^2$ and $p = -\Lambda M_*^2$.) With this energy-stress tensor, the Einstein equation can be decomposed into its $\mu = \nu = i$ component:

$$2\frac{\ddot{a}}{a} + \frac{\dot{a}^2}{a^2} + \frac{k}{a^2} = -\frac{p}{M_*^2}. \quad (1.5)$$

and its $\mu = \nu = 0$ component:

$$\frac{\dot{a}^2}{a^2} + \frac{k}{a^2} = \frac{\rho}{3M_*^2}. \quad (1.6)$$

The latter equation is known as the Friedmann equation. It is used to find the time evolution of the scale factor. Thus, Einstein's equations predict in general a dynamic universe $\dot{a} \neq 0$; Hubble's observations of the red-shifts of galaxies imply that $\dot{a} > 0$. Subtracting Eqn. (1.6) from Eqn. (1.5) yields

$$\ddot{a}/a = -\frac{\rho + 3p}{6M_*^2}, \quad (1.7)$$

so $\ddot{a}/a < 0$ as long as $\rho + 3p > 0$. (We will see that both relativistic and non-relativistic matter satisfy this last inequality.) This implies that the expansion of the universe is slowing down, so at some finite time in the past, $a \rightarrow 0$.³ This event of divergent pressure, temperature, and density is known as the “big bang.”

The Friedmann equation is usually written in a slightly different form. In terms of the expansion rate of the universe $H(t) = \dot{a}(t)/a(t)$, (known as the “Hubble parameter”), one can write the Friedmann equation as

$$\rho = 3M_*^2 H^2 + 3M_*^2 k/a^2. \quad (1.8)$$

From this equation, one sees that the “critical density” ρ_C , at which $k = 0$ (also called a “flat” universe), is given by $\rho_C = 3M_*^2 H^2$. Since our universe is nearly flat, I will find it convenient later on to use the ratio of the energy density to the critical density: $\Omega = \rho/\rho_C$.

In order to solve the Friedmann equation (1.8) for the time evolution of $H(t)$, I need the evolution of the energy density. Using the Bianchi identity for Einstein’s equations, one finds that the energy-stress tensor is conserved:

$$T^\mu{}_{\nu;\mu} = 0. \quad (1.9)$$

The $\nu = 0$ component yields the Law of Conservation of Energy:

$$d(\rho a^3) = -p d(a^3). \quad (1.10)$$

³In the theory of inflation, vacuum energy ($p = -\rho < 0$) dominates the very early universe, so $t \rightarrow -\infty$ as $a \rightarrow 0$. In any case, Einstein’s equations are invalid for $a \lesssim M_*^{-1}$ or $\dot{a}/a \gtrsim M_*$; a proper quantum theory of gravity is needed in order to extrapolate all the way back to $a = 0$.

To find the evolution of the energy density ρ , I will use the relation between ρ and the pressure p [14]. In thermal equilibrium, these quantities can be calculated using the phase-space occupancy in terms of the momentum \mathbf{p} (or the energy $E = \sqrt{\mathbf{p}^2 + m^2}$), the chemical potential μ , and the temperature T :

$$f(\mathbf{p}) = \frac{1}{\exp[(E - \mu)/T] \pm 1}, \quad (1.11)$$

where $+$ gives the Fermi-Dirac occupancy for fermions, and $-$ gives the Bose-Einstein occupancy for bosons. I can then find the energy density ρ , the pressure p , and the number density n of an ideal gas of a particle species with g internal degrees of freedom:

$$\rho = \frac{g}{(2\pi)^3} \int d^3\mathbf{p} E(\mathbf{p}) f(\mathbf{p}) \quad (1.12)$$

$$p = \frac{g}{(2\pi)^3} \int d^3\mathbf{p} \frac{\mathbf{p}^2}{3E(\mathbf{p})} f(\mathbf{p}) \quad (1.13)$$

$$n = \frac{g}{(2\pi)^3} \int d^3\mathbf{p} f(\mathbf{p}). \quad (1.14)$$

For “hot” (*i.e.* relativistic), non-degenerate matter and radiation (*e.g.*, photons), these integrals can be evaluated by using the limits

$$T \gg m, \quad T \gg \mu \quad (1.15)$$

to obtain

$$\rho_R = \begin{cases} \frac{\pi^2}{30} g T^4 & \text{(Bosons)} \\ \frac{7}{8} \frac{\pi^2}{30} g T^4 & \text{(Fermions)} \end{cases} \quad (1.16)$$

$$p_R = \rho/3 \quad (1.17)$$

$$n_R = \begin{cases} \frac{\zeta(3)}{\pi^2} g T^3 & \text{(Bosons)} \\ \frac{3}{4} \frac{\zeta(3)}{\pi^2} g T^3 & \text{(Fermions)} \end{cases} \quad (1.18)$$

For “cold” (*i.e.* non-relativistic), non-degenerate matter, the integrals can be evaluated by using the limits

$$m \gg T, \quad m \gg \mu \quad (1.19)$$

to obtain

$$n_M = g \left(\frac{mT}{2\pi} \right)^{3/2} \exp \left(\frac{-(m - \mu)}{T} \right) \quad (1.20)$$

$$\rho_M = mn \quad (1.21)$$

$$p_M = nT \ll \rho. \quad (1.22)$$

For cold matter (*viz.*, baryons, my hypothetical late-decaying particle, and electrons in the later stages of BBN), $p_M \simeq 0$, so conservation of energy (1.10) implies that the energy density red-shifts as $\rho_M \propto a^{-3}$. Hot matter (*viz.*, photons, neutrinos, and electrons/positrons in the early stages of BBN), also called radiation, has the energy-pressure relation $p_R = \rho_R/3$, so its energy density red-shifts as $\rho_R \propto a^{-4}$. (Since $\rho_R \propto gT^4$, one can also deduce that $a \propto g^{-1/4}T^{-1}$.) For vacuum energy density ($p_\Lambda = -\rho_\Lambda$), the energy density does not red-shift: $\rho_\Lambda \propto a^0$ (hence the name “cosmological constant”).

The present-day radiation energy density is usually assumed to be negligible. The cosmic microwave background radiation (CMBR) (at a temperature of $\simeq 3$ K [2]) has an energy density of $\rho_\gamma \sim 10^{-51}$ GeV, so $\Omega_\gamma \equiv \rho_\gamma/\rho_C \sim 10^{-4}$. Non-degenerate neutrinos (assumed in SBBN) would make a contribution of the same order. In order for there to be sufficient time for structure formation, any other primordial radiation component must also be negligible today. On the other

hand, luminous baryonic matter (*i.e.*, stars) makes a present-day contribution of $\Omega_{lum} \sim 1\%$, which is much greater than that of radiation.

Since radiation is negligible, the COBE measurements of the power spectrum of the CMBR can be used to constrain cold matter and vacuum energy [15] to $0.3 < \Omega_M + \Omega_\Lambda < 1.5$. Combining this with the constraint $\Omega_\Lambda \simeq \Omega_M + 0.5$ from distance measurements from supernovae [16], it has been deduced [17] that at the 95% confidence level,

$$\Omega_M = 0.25^{+0.18}_{-0.12} \quad (1.23)$$

$$\Omega_\Lambda = 0.63^{+0.17}_{-0.23} \quad (1.24)$$

Thus, today's universe is nearly flat, and it is dominated by vacuum energy or a mixture of vacuum energy and cold matter⁴.

At early times, Ω is even closer to 1 than it is today. In my dissertation, I shall be interested in the era when $T_\gamma \gtrsim 1$ keV, so that $a \sim T^{-1}$ has less than 1/300 of its present value. At those times, $\rho_M \propto a^{-3}$ and $\rho_R \propto a^{-4}$ dominate over $\rho_\Lambda \propto a^0$. In a matter-dominated (MD) or radiation-dominated (RD) universe, $\rho = Ca^{-n}$ (MD: $n = 3$; RD: $n = 4$). The Friedmann equation (1.8) can then be rewritten:

$$\dot{a}^2 = \frac{C}{3M_*^2} \frac{1}{a^{n-2}} - k. \quad (1.25)$$

As $a \rightarrow 0$, the first term on the right-hand side becomes much larger than $k = -1, 0, 1$, so one may neglect k . In this limit, the Friedmann equation then

⁴The observational data rule out the theoretical prejudice that $\Omega_\Lambda = 0$. However, it has been suggested that there may be systematic errors in the supernovae data, such as an unknown evolutionary effect; possible systematic errors are discussed in Reference [17].

simplifies:

$$\rho = 3M_*^2 H^2. \quad (1.26)$$

In the remainder of this work, I shall set $k = 0$.⁵

The final ingredient necessary to an understanding of the time evolution of the energy density and pressure is a model of particle physics. Here I will assume the Standard Model (I will consider some extensions later). In a radiation-dominated era, such as BBN, the energy density and pressure can conveniently be expressed in terms the effective number of relativistic degrees of freedom:

$$\begin{aligned} g_* &= \sum_{i=bosons} \left(\frac{T_i}{T}\right)^4 + \frac{7}{8} \sum_{i=fermions} \left(\frac{T_i}{T}\right)^4 \\ \rho_R &= \frac{\pi^2}{30} g_* T^4 \\ p_R &= \rho_R/3. \end{aligned} \quad (1.27)$$

T is the photon temperature, and T_i is the temperature of species i . For example, for $100 \text{ MeV} \gtrsim T \gtrsim 1 \text{ MeV}$, the relativistic species are photons, three generations of neutrinos, and electrons/positrons. They are all in thermal equilibrium with a common temperature T , so $g_* = 10.75$. As the temperature falls, weak reactions freeze out and the neutrinos decouple. At $T \simeq 1 \text{ MeV}$, electrons and positrons become non-relativistic and annihilate (leaving only a tiny remnant of cold electrons); their energy density is dumped into photons, thus raising the photon temperature

⁵In fact, using this limiting form of the Friedmann equation, one can see that $H^2 \propto \rho = C a^{-n}$, so $\Omega - 1 = k/a^2 H^2$ varies as $a^{n-2} \propto 1/T_\gamma^{n-2}$. Thus, Ω was very close to one, when $T_\gamma \gtrsim 1 \text{ keV}$.

relative to that of neutrinos. Entropy considerations [14] yield

$$T_\nu = \left(\frac{4}{11}\right)^{1/3} T \quad (1.28)$$

for $T \ll 1$ MeV. Thus, after electron-positron annihilation ($T \lesssim 30$ keV), $g_* = 3.36$.

1.2 Summary of Standard Big-Bang Nucleosynthesis

SBBN was first proposed by Gamow [1]. His idea was that the elements are synthesized in out-of-equilibrium processes in the early expanding universe. A subsequent refinement to his original theory is that in the early universe ($t \ll 1$ sec, $T \gg 1$ MeV), neutrons, protons, and the heavier nuclides are kept in kinetic and chemical equilibrium by rapid weak and nuclear reactions (see Table 1.1).⁶ However, as the universe expands, these reactions freeze out, one by one. (As a rule of thumb, a given reaction becomes cosmologically negligible when its rate Γ falls below the expansion rate H of the universe.) For example, one of the reactions that maintains chemical equilibrium between protons and neutrons is $p + e^- \rightleftharpoons n + \nu_e$, which (in the limit $T \gg (m_n - m_p), m_e$) has a rate of $\Gamma \simeq G_F^2 T^5$. Combining Eqns. (1.26) and (1.27) for a hot universe yields $H = \frac{\pi}{\sqrt{90}} \sqrt{g_*} \frac{T^2}{M_*}$, so

⁶I will only consider $T \ll m_W$, because the history of the *very* early universe is essentially erased by the thermal equilibration during $m_W \gg T \gg 1$ MeV. I will, however, consider some ‘leftovers’ from the very early universe: the baryon to photon ratio; and the abundance of heavy, long-lived particles.

that

$$\Gamma/H \simeq (T/0.8 \text{ MeV})^3, \quad (1.29)$$

i.e., below the freeze-out temperature $T_F \simeq 0.8 \text{ MeV}$, neutrons fall out of chemical equilibrium with protons. Similarly, each of the fusion reactions freezes out: ${}^4\text{He}$ synthesis proceeds essentially to completion (when almost all neutrons have been used up); ${}^{12}\text{C}$ production freezes out before it can begin; and trace amounts of the other light elements are left over. Finally, by $t \simeq 1 \text{ hr}$ ($T \simeq 20 \text{ keV}$), primordial nucleosynthesis is complete.

In standard big-bang nucleosynthesis, one assumes standard FRW cosmology and the Standard Model of particle physics (with three generations of massless neutrinos). Furthermore, one assumes zero neutrino chemical potentials and zero cosmological constant. These assumptions leave only one free parameter, *viz.*, the ratio η of the baryon number density to the photon number density (or, alternatively, the ratio $\Omega_b = 4 \times 10^7 \eta$ of the baryon energy density ρ_{baryon} to the critical density ρ_C). Taking the very conservative bound $\Omega_b \geq 0.006$ derived from observed luminous matter [14], and the bound $\Omega_b \leq \Omega = 1$ (since we assume a flat universe), one obtains the limits

$$1.6 \times 10^{-10} < \eta < 2.7 \times 10^{-8}. \quad (1.30)$$

Note that this range is independent of BBN. Historically, SBBN has been used to give the most precise determination of η , *viz.*, a few $\times 10^{-10}$.

In my computer simulation of BBN (based upon the code of Kawano [26]),

I follow the time evolution of the photon temperature T , the electron chemical potential μ_e , the baryon-to-photon ratio η , and the abundances of the various nuclear species (and of my hypothetical radiatively-decaying particle X). From these quantities, I can use Eqs. (1.12)–(1.22) to compute the energy densities and pressures of all the particles in the big-bang plasma: photons, neutrinos, electrons/positrons, and the nuclides (and X). To time-evolve T , μ_e , η , and the abundances, the code integrates a set of mixed partial differential equations. I will omit here the details of the equations for dT/dt , $d\mu_e/dt$, and $d\eta/dt$, except to mention that they are derived from the Friedmann equation (1.26) and Eqs. (1.12)–(1.14). The time evolution of the abundances is computed using a matrix of Boltzmann equations. For example, if the nuclide ${}^{A_i}Z_i$ has only two-body to two-body reactions of the form

$$N_i({}^{A_i}Z_i) + N_j({}^{A_j}Z_j) \rightleftharpoons N_k({}^{A_k}Z_k) + N_l({}^{A_l}Z_l), \quad (1.31)$$

then the Boltzmann equation for the abundance Y_i , the number ratio of ${}^{A_i}Z_i$ to baryons, is

$$\frac{dY_i}{dt} = \sum_{j,k,l} N_i \left(-\frac{Y_i^{N_i} Y_j^{N_j}}{N_i! N_j!} [ij]_k + \frac{Y_l^{N_l} Y_k^{N_k}}{N_l! N_k!} [lk]_j \right) \quad (1.32)$$

where $[ij]_k$ and $[lk]_j$ are the forward and backward reaction rates, respectively.

The observable results of this theoretical simulation are the abundances of the light elements. Densities are not suitable observables, because they continually decrease as the universe expands. Instead, I consider the *ratio* of number densities n (or of energy densities ρ), which can also be thought of as the number per

unit comoving (*i.e.*, moving with the general expansion) volume. Using standard notation, the quantities in which I am interested are:

$$y_2 = n_{\text{D}}/n_{\text{H}}, \quad (1.33)$$

$$y_3 = n_{\text{He}}/n_{\text{H}}, \quad (1.34)$$

$$Y = \rho_{\text{He}}/\rho_{\text{baryon}}, \quad (1.35)$$

$$y_6 = n_{\text{Li}}/n_{\text{H}}, \quad (1.36)$$

$$y_7 = n_{\text{Li}}/n_{\text{H}}. \quad (1.37)$$

where $n_{\text{Z A}}$ is the number density of the nuclide ${}^{\text{A}}\text{Z}$.

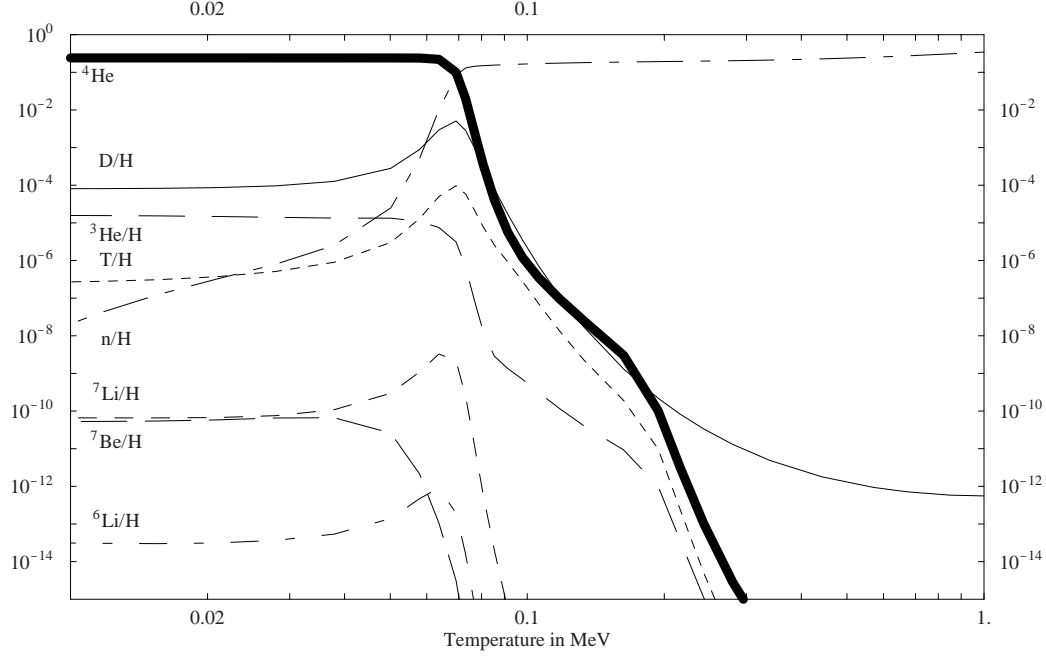
One can better understand SBBN by looking at the light-element abundances as functions of time, as shown in Fig. 1.1. At high temperatures ($T > 1$ MeV, $t < 1$ sec), all nuclides are in thermal and chemical equilibrium. Entropy is more important than binding energy in the free energy, so free protons and neutrons dominate over bound nuclei. As the temperature decreases, the weak reactions freeze out, so neutrinos decouple when $T \simeq 0.8$ MeV (see Eq. (1.29)) and neutron-proton inter-conversion ceases ($T \simeq 0.7$ MeV). At this time, the neutron-to-proton ratio is given by the Boltzmann factor $\exp(-(m_n - m_p)/T) \simeq 1/6$; after this, the n/p ratio decreases through free neutron decay $n \rightarrow p + e^- + \bar{\nu}_e$, with a lifetime of 886.7 sec [4]. At temperatures of about $T \simeq 0.5$ MeV, the abundance Y of ${}^4\text{He}$ falls below its chemical equilibrium value, because the Coulomb barrier is becoming significant relative to the temperature, and also because the abundance of helium's precursors (D, ${}^3\text{He}$, and ${}^3\text{H}$) is very small (the so-called “deuterium bottleneck”).

When $T \simeq m_e/3$, positrons and electrons annihilate into photons, thereby decreasing the baryon-to-photon ratio η by a factor of $(4/11)^{1/3}$ (see Eq. (1.28)). When $T \simeq 50$ keV, essentially all free neutrons have been bound up into ${}^4\text{He}$. By this time, free-neutron decay has reduced the n/p ratio to about $1/7$; a simple calculation shows that the ${}^4\text{He}$ abundance will be $Y \simeq 1/4$.

Primordial nucleosynthesis concludes by $T \simeq 20$ keV. The lack of a stable isotope with nuclear weight $A = 8$ prevents any double- α reactions; the triple- α reaction $3 {}^4\text{He} \rightarrow {}^{12}\text{C}$ is blocked by the Coulomb barrier. At later times, all primordial (as opposed to stellar) nuclear reactions are prevented by both the Coulomb barrier and the diluteness of the nuclei. Small remnants of D, ${}^3\text{He}$, and ${}^3\text{H}$ do not get bound up into ${}^4\text{He}$. Even smaller amounts of ${}^7\text{Li}$, ${}^7\text{Be}$, and ${}^6\text{Li}$ are synthesized in the big bang. After primordial nucleosynthesis, all remaining free neutrons soon decay into protons, ${}^3\text{H}$ β -decays into ${}^3\text{He}$ with a lifetime of 5.6×10^8 sec, and ${}^7\text{Be}$ decays through electron capture into ${}^7\text{Li}$ with a lifetime of 6.6×10^6 sec. Thus, the only abundances of interest today are those in Eqs. (1.33)–(1.37). I shall refer to these abundances (after n , ${}^3\text{H}$, and ${}^7\text{Be}$ decay) as the “primordial” abundances.

One can gain more insight into SBBN by considering the primordial abundances as functions of η , as shown in Fig. 1.2. The dependence of the abundances on η can be seen intuitively [5, 27]. The ${}^4\text{He}$ abundance is a gentle, monotonically increasing function of η . As η increases, ${}^4\text{He}$ is produced earlier because the “deuterium bottleneck” is overcome at a higher temperature due to the higher baryon

Figure 1.1: SBBN prediction of the abundances of the light elements, as functions of time, for $\eta = 3 \times 10^{-10}$.



density. Fewer neutrons have had time to decay, so more ${}^4\text{He}$ is synthesized. Since ${}^4\text{He}$ is the most tightly bound of the light nuclei, D and ${}^3\text{He}$ are fused into ${}^4\text{He}$. The surviving abundances of D and ${}^3\text{He}$ are determined by the competition between their destruction rates and the expansion rate. The destruction rates are proportional to η , so the larger η is, the longer the destruction reactions continue. Therefore, D/H and ${}^3\text{He}/\text{H}$ are monotonically decreasing functions of η . Moreover, the slope of D/H is steeper, because the binding energy of D is smaller than that of ${}^3\text{He}$.

The graph of ${}^7\text{Li}/\text{H}$ has a trough near $\eta \sim 3 \times 10^{-10}$. For a low baryon density $\eta \lesssim 3 \times 10^{-10}$, ${}^7\text{Li}$ is produced by ${}^3\text{H}(\alpha, \gamma){}^7\text{Li}$ and is destroyed by ${}^7\text{Li}(p, \alpha){}^4\text{He}$. As η increases, the destruction reactions become more efficient and the produced ${}^7\text{Li}$

tends to decrease. On the other hand, for a high baryon density $\eta \gtrsim 3 \times 10^{-10}$, ${}^7\text{Li}$ is mainly produced through the electron capture of ${}^7\text{Be}$. Because ${}^7\text{Be}$ production through ${}^3\text{He}(\alpha, \gamma){}^7\text{Be}$ becomes more effective as η increases, the synthesized ${}^7\text{Li}$ increases. The “trough” results from the overlap of these two components. The dominant source of ${}^6\text{Li}$ in SBBN is $\text{D}(\alpha, \gamma){}^6\text{Li}$. Thus, the η dependence of ${}^6\text{Li}/\text{H}$ resembles that of D/H .

I have also plotted the one- σ observational constraints on the abundances of ${}^4\text{He}$, D/H , and ${}^7\text{Li}/\text{H}$, as well as the proto-solar abundances of $(\text{D}+{}^3\text{He})/\text{H}$ and ${}^3\text{He}/\text{H}$. I will discuss the observations in detail in Chapters 3 and 5. (I have drawn two boxes for both ${}^4\text{He}$ and D/H , because the literature gives multiple, inconsistent values for both of these abundances. ${}^3\text{He}/\text{H}$ is shown as an upper bound, because the proto-solar value includes the primordial ${}^3\text{He}/\text{H}$ plus stellar ${}^3\text{He}/\text{H}$.) For now, it suffices to note that the theory gives a favored range of η for each of the observed abundances. The amount of overlap of the boxes is a rough measure of the consistency between theory and observations. In Chapters 4 and 5, I will carefully analyze the consistency between theory and observation. But from Fig. 1.2, one can see that low ${}^4\text{He}$ is consistent with high D/H (for $\eta \simeq 2 \times 10^{-10}$), and high ${}^4\text{He}$ is consistent both with low D/H and with the proto-solar data (for $\eta \simeq 5 \times 10^{-10}$). (Because of the large uncertainty in ${}^7\text{Li}/\text{H}$, ${}^7\text{Li}/\text{H}$ is consistent with all the other data.) Moreover, since the ${}^4\text{He}$ abundance has a shallow slope at high η , the high ${}^4\text{He}$ value gives a large uncertainty in η . Thus, even the high ${}^4\text{He}$ value is marginally consistent with the high D/H , for $\eta \simeq 2 \times 10^{-10}$ (this

value is determined primarily by the high D/H). However, in SBBN, low ^4He is inconsistent with low D/H.⁷

1.3 History of BBN Theory

Since Gamow’s original idea in 1946 [1], BBN has become (together with the CMBR and the direct measurement of the Hubble recession of galaxies) one of the best reasons to believe the theory of the big bang. Gamow and Alpher originally performed analytic computations of the light-element synthesis in non-equilibrium nuclear reactions in the early, rapidly expanding universe. Alpher, Follin, and Herman [28] pointed out the importance of particle reactions in determining the initial conditions for BBN, such as the initial n/p ratio; Hoyle and Taylor [29] analytically calculated the primordial ^4He abundance. Peebles [30] wrote the first computer code to track the ^4He abundance. The precursor to the code I use was written in 1967 by Wagoner, Fowler, and Hoyle [31]. Their code includes the nuclear reactions for all the light elements (see Table 1.1) and numerically integrates the mixed, partial differential equations for the abundances of the light elements. With the improved accuracy of the theory, BBN became an important test of big-bang cosmology. Other groups have written independent codes [32], thus providing checks on each others’ work. The “standard code” for BBN, written by Wagoner [33], has been improved with corrections for finite temperature and radiative effects [34].

⁷In fact, from my analysis in Chapter 4 based upon ^4He , D/H, and ^7Li , I find that this last case is excluded at the 91.5% C.L.

Kawano [26] improved the numerical integration and documentation of this code. In my research, I have modified Kawano’s version to simulate non-standard BBN with a radiatively decaying particle. K. Kohri [35] has independently modified Kawano’s code to simulate the same scenario, thus providing a check on my work (and *vice versa*).

My work on big-bang nucleosynthesis was originally motivated by the claim by Hata *et al.* [36] of a “crisis” in BBN; *viz.*, that recent light-element observations seemed to conflict with the theoretical predictions of standard BBN. Their point was that standard BBN predicts too much ^4He , if the baryon number density is determined by the D abundance inferred from solar-system observations; equivalently, standard BBN predicts too much D, if the baryon number density is determined by the ^4He observations. Inspired by this “crisis,” many people re-examined BBN. Some have kept standard BBN and argued that the systematic errors in the observations have been underestimated; others have accepted the observations and investigated non-standard BBN. Such non-standard scenarios of BBN include allowing degenerate electron neutrinos [37] (*i.e.*, a large neutrino chemical potential). Another non-standard scenario assumes a massive unstable neutrino with mass about 1 MeV and lifetime about 1 sec [38]. In a previous paper [39], I investigated a non-standard theory of BBN in which radiatively-decaying, massive particles induce electromagnetic cascades. For a certain range of parameters in our model, my colleagues and I found that the photons in these cascades destroy only D, so that the predicted abundances of D, ^3He , and ^4He fit

the observations.

However, since the “BBN crisis” was claimed, the situation concerning the observations of deuterium has become more complicated. In addition to the proto-solar and interstellar medium measurements of D/H, now the D abundances in highly red-shifted quasar absorption systems (QAS) have been measured. Because such systems show very low levels of “metals” (*i.e.*, elements heavier than ${}^4\text{He}$) such as nitrogen, oxygen, and iron, the abundance of D in these QAS is considered to be the primordial value. Both sets of D/H measurements have their problems, as I will discuss in Chapter 3.

Moreover, there are also differing determinations of the primordial ${}^4\text{He}$ abundance. Hata *et al.* used a relatively low ${}^4\text{He}$ abundance (*viz.*, $Y \simeq 0.234$, where Y is the primordial mass fraction of ${}^4\text{He}$) [40, 41]. However, a higher ${}^4\text{He}$ abundance ($Y \simeq 0.244$) has also been reported [42, 43, 44]. It has been noted that this higher observation alleviates the discrepancy with standard BBN theory [45]. The typical errors in ${}^4\text{He}$ observations are less than $\simeq 0.005$, so I have discordant data for ${}^4\text{He}$.

Since I have discordant ${}^4\text{He}$ abundances and new observations for D, the previous constraints on the radiative decay of long-lived particles must be revised. In addition, the statistical analyses on radiatively decaying particles are insufficient in the previous works. Therefore, in my dissertation, I perform a better statistical analysis of a long-lived, radiatively-decaying particle, and of the resultant photodissociations, in order to constrain the abundances and lifetimes of long-lived particles. In deriving the constraints, I use two observed values of the ${}^4\text{He}$

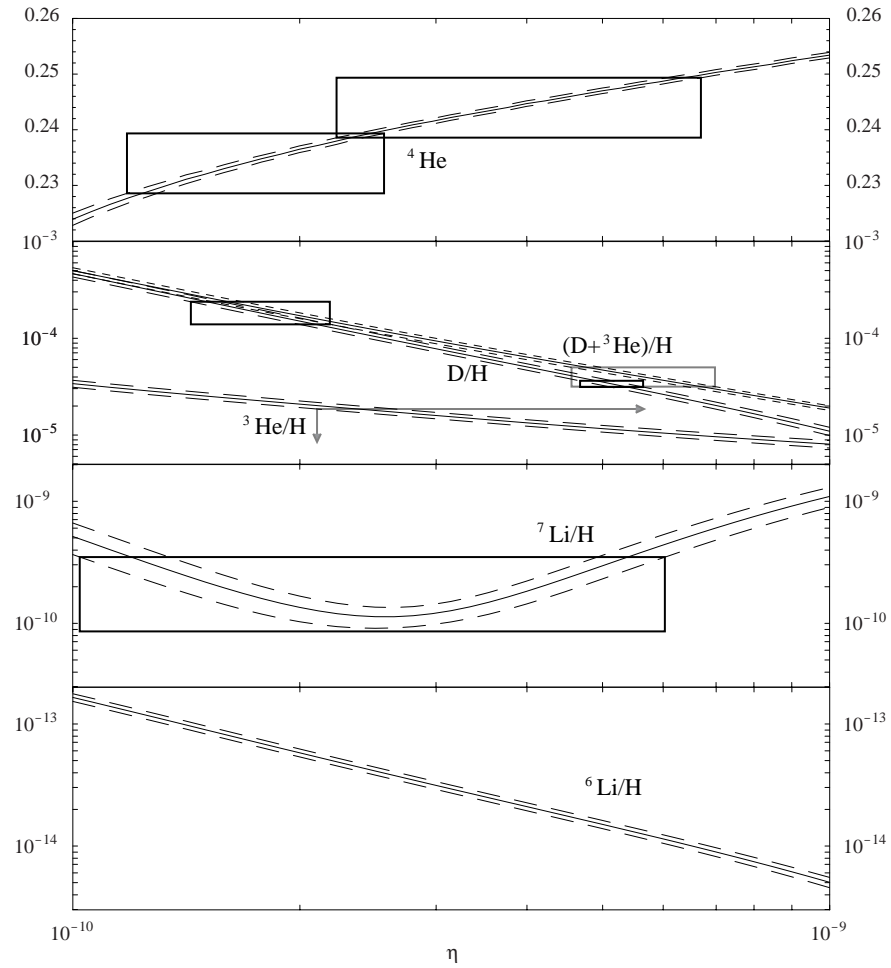
abundance (high and low), and three sets of data for the D/H abundance (high QAS D/H, low QAS D/H, and proto-solar $(D+{}^3\text{He})/\text{H}$ and ${}^3\text{He}/\text{H}$), for a total of six combinations of the observations. I use all values because I believe that it is premature to decide which data are correct. For the low measurement of the ${}^4\text{He}$ abundance and either the low QAS measurement of D/H or the proto-solar data, I show that the agreement is poor between observations and the standard BBN theory. Moreover, I show in the case of low QAS D/H that a long-lived particle with an appropriate abundance and lifetime can solve the discrepancy. In the other cases, standard BBN fits the observations, so I derive stringent constraints on the properties of long-lived particles.

In Ch. 2, I investigate how the radiative decay of a long-lived particle affects the primordial abundances of the light elements. I also discuss the uncertainties in my calculations. In Ch. 3, I review the primordial abundances that are extrapolated from observations, using QAS systems for the deuterium measurements. In Ch. 4, I describe the statistical analysis I use to compare the predicted abundances to the observed abundances, and I present the results of my analysis. In Ch. 5, I consider the observed proto-solar and interstellar-medium abundances of D and ${}^3\text{He}$, I describe how I use this information to compare to the predicted primordial abundances, and I present my results. I consider various particle-physics models for my long-lived, radiatively decaying particle in Ch. 6. Finally, Ch. 7 is devoted to discussion and the conclusion.

	Nucleosynth. Reaction	One- σ Uncertainty	Ref.
1.	$n + \rightleftharpoons p + e^- + \bar{\nu}$	1.9 sec	[4]
2.	${}^3\text{H} \rightarrow e^- + \bar{\nu} + {}^3\text{He}$		[18]
3.	${}^8\text{Li} \rightarrow e^- + \bar{\nu} + 2{}^4\text{He}$		[19]
4.	${}^{12}\text{B} \rightarrow e^- + \bar{\nu} + {}^{12}\text{C}$		[20]
5.	${}^{14}\text{C} \rightarrow e^- + \bar{\nu} + {}^{14}\text{N}$		[21]
6.	${}^8\text{B} \rightarrow e^+ + \nu + 2{}^4\text{He}$		[19]
7.	${}^{11}\text{C} \rightarrow e^+ + \nu + {}^{11}\text{B}$		[20]
8.	${}^{12}\text{N} \rightarrow e^+ + \nu + {}^{12}\text{C}$		[20]
9.	${}^{13}\text{N} \rightarrow e^+ + \nu + {}^{13}\text{C}$		[21]
10.	${}^{14}\text{O} \rightarrow e^+ + \nu + {}^{14}\text{N}$		[21]
11.	${}^{15}\text{O} \rightarrow e^+ + \nu + {}^{15}\text{N}$		[21]
12.	${}^1\text{H}(n, \gamma)\text{D}$	7%	[22]
13.	$\text{D}(n, \gamma){}^3\text{H}$		[23]
14.	${}^3\text{He}(n, \gamma){}^4\text{He}$		[23]
15.	${}^6\text{Li}(n, \gamma){}^7\text{Li}$		[24]
16.	${}^3\text{He}(n, p){}^3\text{H}$	10%	[22]
17.	${}^7\text{Be}(n, p){}^7\text{Li}$	9%	[22]
18.	${}^6\text{Li}(n, \alpha){}^3\text{H}$		[25]
19.	${}^7\text{Be}(n, \alpha){}^4\text{He}$		[23]
20.	$\text{D}(p, \gamma){}^3\text{He}$	10%	[22]
21.	${}^3\text{H}(p, \gamma){}^4\text{He}$		[25]
22.	${}^6\text{Li}(p, \gamma){}^7\text{Be}$		[25]
23.	${}^6\text{Li}(p, \alpha){}^3\text{He}$		[25]
24.	${}^7\text{Li}(p, \alpha){}^4\text{He}$	8%	[22]
25.	$\text{D}(\alpha, \gamma){}^6\text{Li}$		[25]
26.	${}^3\text{H}(\alpha, \gamma){}^7\text{Li}$	$\begin{cases} T > 10 \text{ GK} : 8.1\%; \\ T < 10 \text{ GK} : 0.29 - 0.059\theta^{1/2} \\ \quad - 0.072\theta + 0.040\theta^{3/2} - 0.0056\theta^2, \\ \quad \text{for } \theta = T/\text{GK} + 0.0419 \end{cases}$	[22]
27.	${}^3\text{He}(\alpha, \gamma){}^7\text{Be}$	$\begin{cases} T > 10 \text{ GK} : 9.7\%; \\ T < 10 \text{ GK} : 0.27 - 0.15\theta^{1/2} \\ \quad + 0.040\theta - 0.0025\theta^{3/2} - 0.0002\theta^2, \\ \quad \text{for } \theta = T/\text{GK} + 0.783 \end{cases}$	[22]
28.	$\text{D}(d, n){}^3\text{He}$	10%	[22]
29.	$\text{D}(d, p){}^3\text{H}$	10%	[22]
30.	${}^3\text{H}(d, n){}^4\text{He}$	8%	[22]
31.	${}^3\text{He}(d, p){}^4\text{He}$	8%	[22]
32.	${}^3\text{He}({}^3\text{He}, 2p){}^4\text{He}$		[25]
33.	${}^7\text{Li}(d, n\alpha){}^4\text{He}$		[25]
34.	${}^7\text{Be}(d, p\alpha){}^4\text{He}$		[25]

Table 1.1: The nuclear reactions responsible for the synthesis of the light elements. Uncertainties are given for the twelve most important reactions [25, 22].

Figure 1.2: SBBN prediction of the abundances of the light elements. The solid lines are the central values of the predictions, and the dotted lines represent the one- σ uncertainties. The boxes and lines with arrows denote the one- σ observational constraints. The gray box indicates $(D+{}^3\text{He})/\text{H}$; the black boxes in the second panel indicate D/H .



Chapter 2

X-Decay and Photon Injection

In this dissertation, I am primarily concerned with the effects of photofission of the light elements. This photofission is caused by the electromagnetic cascade initiated by the radiative decay of a massive, long-lived particle (which I shall call X). The most interesting cases are when the cascade-photon energies are comparable to the binding energies of the light nuclides (see Table 2.1); then there can be selective photofission of some nuclear species, but not of others. I therefore begin this chapter with a discussion of the photon spectrum formed in electromagnetic cascades in the big-bang plasma (see Sec. 2.1).

Once I have the photon spectrum, I then use it in a modified version of the Kawano nucleosynthesis code to calculate the light-element abundances for a range of lifetimes and abundances of X , and for a range of baryon-to-photon ratios η . I discuss my results in Sec. 2.2.

Finally, in Sec. 2.3 I discuss various sources of error in my theoretical calculations of the abundances. I estimate the error by two methods: Monte-Carlo, and linear propagation of errors. I compare the two methods, both for reliability and for efficiency.

AZ	Binding Energy (MeV)
D	2.22
${}^3\text{He}$	7.72
${}^4\text{He}$	28.3
${}^6\text{Li}$	32.0
${}^7\text{Li}$	39.2

Table 2.1: The binding energies of some light nuclides AZ .

2.1 Photon Spectrum

In order to discuss the effect of high-energy photons on BBN, I need the shape of the photon spectrum induced by the primary high-energy photons from X decay.

For $10\text{ keV} \gtrsim T \gtrsim 10\text{ eV}$, the background thermal bath of the big bang is a mixture of photons γ_{BG} , electrons e_{BG}^- , and nucleons and nuclei N_{BG} . In this bath, high-energy photons lose their energy by various cascade processes. These electromagnetic cascades induce the photon spectrum, as discussed in various literature [46]. The important processes in my case are:

- Double-photon pair creation ($\gamma + \gamma_{\text{BG}} \rightarrow e^+ + e^-$)
- Photon-photon scattering ($\gamma + \gamma_{\text{BG}} \rightarrow \gamma + \gamma$)
- Pair creation in nuclei ($\gamma + N_{\text{BG}} \rightarrow e^+ + e^- + N$)
- Compton scattering ($\gamma + e_{\text{BG}}^- \rightarrow \gamma + e^-$)
- Inverse Compton scattering ($e^\pm + \gamma_{\text{BG}} \rightarrow e^\pm + \gamma$)

(I may neglect double Compton scattering $\gamma + e_{\text{BG}}^- \rightleftharpoons \gamma + \gamma + e^-$, because Compton scattering is more important for thermalizing high-energy photons.) In our anal-

ysis of the spectrum [35], my colleagues and I numerically solved the Boltzmann equation for the spectral distribution of photons $f_\gamma(E_\gamma) \equiv dn_\gamma/dE_\gamma$, including the above interactions [8, 9].

Fig. 2.1 shows the photon spectrum for several background temperatures T . Roughly speaking, there is a large drop-off at $E_\gamma \sim m_e^2/22T$ for each temperature. Above this threshold, the photon spectrum is extremely suppressed.

The qualitative behavior of the photon spectrum can be understood in the following way. If the photon energy is high enough, then double-photon pair creation is so efficient that this process dominates the cascade. However, once the photon energy becomes much smaller than $O(m_e^2/T)$, double-photon pair creation is kinematically blocked. Numerically, this threshold is about $m_e^2/22T$, as seen in Fig. 2.1. Below this threshold, photon-photon scattering dominates. However, since the scattering rate due to this process is proportional to E_γ^3 , photon-photon scattering becomes unimportant in the limit $E_\gamma \rightarrow 0$. Therefore, for $E_\gamma \ll O(m_e^2/T)$, the remaining processes (pair creation in nuclei, Compton scattering, and inverse Compton scattering) are the most important.

The crucial point is that the scattering rate for $E_\gamma \gtrsim m_e^2/22T$ is much larger than that for $E_\gamma \ll m_e^2/22T$, since the number of targets in the former case (photons) is several orders of magnitude larger than in the latter (fermions and nuclei). This is why the photon spectrum is extremely suppressed for $E_\gamma \gtrsim m_e^2/22T$. Photons with energies above this threshold will induce electromagnetic cascades (and transfer their energy to low-energy particles) before they encounter a nu-

cleus and dissociate it. As a result, if the X particle decays in a thermal bath with temperature $T \gtrsim m_e^2/22Q$ (where Q is the binding energy of a nuclide), then photodissociation is ineffectual.

2.2 Resulting Abundances

Once the photon spectrum is formed, it induces the photodissociation of the light nuclei, which modifies the result of BBN. This process is governed by the following Boltzmann equation:

$$\begin{aligned} \frac{dn_N}{dt} + 3Hn_N = & \left[\frac{dn_N}{dt} \right]_{\text{SBBN}} - n_N \sum_{N'} \int dE_\gamma \sigma_{N\gamma \rightarrow N'}(E_\gamma) f_\gamma(E_\gamma) \\ & + \sum_{N''} n_{N''} \int dE_\gamma \sigma_{N''\gamma \rightarrow N}(E_\gamma) f_\gamma(E_\gamma), \end{aligned} \quad (2.1)$$

where n_N is the number density of the nucleus N , and $[dn_N/dt]_{\text{SBBN}}$ denotes the SBBN contribution to the Boltzmann equation. I modified the Kawano code [26] to take account of the non-thermal photon spectrum and the photodissociation processes. Using my modified code, I calculated the abundances of the light elements. The photodissociation processes I included in my calculation are listed in Table 2.2.

The abundances of light nuclides will be functions of the baryon-to-photon ratio (η), the lifetime of X (τ_X), the mass of X (m_X), and the abundance of X

	Photofission Reactions	1σ Uncert.	Threshold	Ref.
1.	$D + \gamma \rightarrow p + n$	6%	2.2 MeV	[47]
2.	${}^3\text{H} + \gamma \rightarrow n + D$	14%	6.3 MeV	[48, 49]
3.	${}^3\text{H} + \gamma \rightarrow p + 2n$	7%	8.5 MeV	[49]
4.	${}^3\text{He} + \gamma \rightarrow p + D$	10%	5.5 MeV	[50]
5.	${}^3\text{He} + \gamma \rightarrow n + 2p$	15%	7.7 MeV	[50]
6.	${}^4\text{He} + \gamma \rightarrow p + {}^3\text{H}$	4%	19.8 MeV	[50]
7.	${}^4\text{He} + \gamma \rightarrow n + {}^3\text{He}$	5%	20.6 MeV	[51, 52]
8.	${}^4\text{He} + \gamma \rightarrow p + n + D$	14%	26.1 MeV	[53]
9.	${}^6\text{Li} + \gamma \rightarrow \text{anything}$	4%	5.7 MeV	[54]
10.	${}^7\text{Li} + \gamma \rightarrow 2n + \text{anything}$	9%	10.9 MeV	[54]
11.	${}^7\text{Li} + \gamma \rightarrow n + {}^6\text{Li}$	4%	7.2 MeV	[54]
12.	${}^7\text{Li} + \gamma \rightarrow {}^4\text{He} + \text{anything}$	9%	2.5 MeV	[54]
13.	${}^7\text{Be} + \gamma \rightarrow p + {}^6\text{Li}$			
14.	${}^7\text{Be} + \gamma \rightarrow \text{anything except } {}^6\text{Li}$			

Table 2.2: Photodissociation processes, and the one- σ uncertainty in the cross sections. Since there are no experimental data on photodissociation of ${}^7\text{Be}$, I assume in this dissertation that the rate of Reaction 13 is the same as that of Reaction 11, and that the rate of Reaction 14 is the sum of the rates of Reactions 10 and 12.

relative to photons¹ before electron-positron annihilation:

$$Y_X = n_X/n_\gamma. \quad (2.2)$$

(I assume for simplicity that $X \rightarrow \gamma + \gamma$ with a 100% branching ratio. Since photofission depends upon the total amount of injected photon energy, and not upon the details of the spectrum of the injected photons, the correction if $X \rightarrow \gamma + \text{invisible}$ is trivial: simply replace $m_X Y_X$ with $\rho_{\gamma, \text{injected}}/n_{\gamma, \text{background}}$. I will discuss the effect of other decays in Section 4.3.) The abundance is essentially the number of X in a comoving volume, and it evolves with time approximately as

¹Note that this convention differs from y_i , which is the number density of nuclide i relative to that of hydrogen, and from Y , which is the energy density of ${}^4\text{He}$ relative to that of baryons.

$Y_X \simeq Y_{X0}e^{-t/\tau_X}$, except for corrections involving photon production during the electron-positron annihilation and during X -decay. My full numerical simulation is needed to properly account for these corrections.

In my numerical BBN simulations, I found that the nuclide abundances depend not on m_X and Y_X separately, but only on their product $m_X Y_X$. This is because double-photon pair creation is very efficient in moving energy from the short end of the spectrum to the long end, so the only important question is how much (not at what wavelength) photon energy is injected into the big-bang plasma. Thus, once τ_X , $m_X Y_X$, and η are fixed, I can calculate the primordial abundances of the light elements. In Figs. 2.2 – 2.6, I show these theoretical abundances y_2, y_3, Y, y_6 , and y_7 in the $m_X Y_X$ vs. τ_X plane, at fixed η .

The qualitative behaviors of the abundances can be understood in the following way. If the mass density of X is small enough, then the effects of X are negligible, and hence the results of SBBN are reproduced. However, once the mass density gets larger, the SBBN results are modified. The effects of X depend strongly upon τ_X , the lifetime of X . As I mentioned in the previous section, photons with energy greater than $\sim m_e^2/22T$ participate in pair creation before they can induce photofission. Therefore, if the above threshold energy is smaller than the nuclear binding energy, then photodissociation is ineffectual.

If $\tau_X \lesssim 10^4$ sec, then $m_e^2/22T \lesssim 2$ MeV at the decay time of X , and photodissociation is negligible for all elements. In this case, the main effect of X is on the ${}^4\text{He}$ abundances: if the abundance of X is large, its added energy density speeds

up the expansion rate of the universe, according to the Friedmann equation (1.26) (C is a constant):

$$\frac{\pi^2}{30}g_*T^4 + CT^3 = 3m_*^2H^2. \quad (2.3)$$

Thus, Eqn (1.29) is modified:

$$\Gamma/H \simeq (T/0.8 \text{ MeV})^3 - O(T^2). \quad (2.4)$$

The neutron freeze-out temperature (where $\Gamma/H = 1$) becomes higher, so the ratio of $n/p \propto \exp(-(m_n - m_p)/T)$ becomes higher. Thus, the ${}^4\text{He}$ abundance is enhanced relative to SBBN.

If $10^4 \text{ sec} \lesssim \tau_X \lesssim 10^6 \text{ sec}$, then $2 \text{ MeV} \lesssim m_e^2/22T \lesssim 20 \text{ MeV}$. In this case, ${}^4\text{He}$ remains intact, but D is effectively photodissociated through the process $\text{D} + \gamma \rightarrow p + n$. When $\tau_X \gtrsim 10^5 \text{ sec}$, $m_e^2/22T \gtrsim 7.7 \text{ MeV}$ (the binding energy of ${}^3\text{He}$), so ${}^3\text{He}$ is dissociated for $\tau_X \sim 10^5 \text{ sec}$ and large enough abundances $m_X Y_X \gtrsim 10^{-8} \text{ GeV}$. If the lifetime is long enough ($\tau_X \gtrsim 10^6 \text{ sec}$), ${}^4\text{He}$ can also be destroyed effectively. In this case, the destruction of even a small fraction of the ${}^4\text{He}$ can result in significant production of D and ${}^3\text{He}$, since the ${}^4\text{He}$ abundance is originally several orders of magnitude larger than that of D and ${}^3\text{He}$. This can be seen in Figs. 2.2, 2.3, and 2.4: for $\tau_X \gtrsim 10^6 \text{ sec}$ and $m_X Y_X \lesssim 10^{-10} \text{ GeV}$, the abundance of D and ${}^3\text{He}$ changes drastically due to the photodissociation of ${}^4\text{He}$. If $m_X Y_X$ is large enough, all the light elements are destroyed efficiently, which results in very small abundances.

So far, I have discussed the theoretical calculation of the light element abun-

dances in a model with X decay. In the next chapter, I will compare the theoretical calculations with observations, and I will derive constraints on the properties of X . But before I do that, I will discuss how I handle the uncertainties in the theoretical calculations.

2.3 Uncertainties and Linear Propagation of Error

In addition to incorporating photofission reactions into Kawano’s nucleosynthesis code [26], I also modified the code to determine the effects of the uncertainties in the rates of the photofission reactions (given in Table 2.2) and the twelve most important nucleosynthesis reactions [25, 22] (given in Table 1.1).² (The most important of these uncertainties is that of the neutron lifetime [4], because this determines the initial n/p ratio.) I use two different methods (Monte-Carlo and linear propagation of errors) to find the effects on the abundances, and I compare these methods for accuracy and efficiency.

Moreover, I also perform an analysis that includes the correlations between the abundances of different elements as each reaction rate is varied separately. Typically in the literature, such correlations are neglected without justification. However, some authors have claimed that they may be important [56]. I compare my analysis with correlations to an analysis that neglects correlations, and I show

²The other uncertainties, *e.g.*, error in the radiative and finite-temperature corrections, numerical errors in the integration algorithm, *etc.* are all limited to a fraction of a percent of the abundances. [55]

that the correlations have negligible effect in the regions of physical interest, thus justifying the usual practice of neglecting the correlations.

The first method I use to take account of the errors in reaction rates is the Monte-Carlo technique. I assume that each reaction rate is an independent random variable drawn from a Gaussian probability distribution function (p.d.f.) with a standard deviation as given in Table 1.1 or Table 2.2. Then, for each fixed value of $(\tau_X, m_X Y_X, \eta)$, I perform a multi-dimensional Monte-Carlo over the entire set of photofission and important nucleosynthesis reactions. I find that the resulting light-element abundances y_2, y_3, Y , and $\log_{10} y_7$ are distributed approximately according to independent, Gaussian p.d.f.'s.³ Therefore, the p.d.f. p^{th} for the theoretical abundances is given by the product of the Gaussian p.d.f.'s

$$p^{Gauss}(x; \bar{x}, \sigma) = \frac{1}{\sqrt{2\pi}\sigma} \exp \left[-\frac{1}{2} \left(\frac{x - \bar{x}}{\sigma} \right)^2 \right] \quad (2.5)$$

for the individual light elements:

$$\begin{aligned} p^{th}(y_2^{th}, y_3^{th}, Y^{th}, \log_{10} y_7^{th}) &= p_2^{Gauss}(y_2^{th}) \times p_3^{Gauss}(y_3^{th}) \times \\ & p_4^{Gauss}(Y^{th}) \times p_7^{Gauss}(\log_{10} y_7^{th}). \end{aligned} \quad (2.6)$$

The Monte-Carlo technique can model my assumption of Gaussian reaction-rate p.d.f.'s as accurately as I please, simply by using a sufficient number of points.

³Because of the large uncertainty in ${}^7\text{Li}$, it is more convenient to use $\log_{10} y_7^{th}$. And indeed, I find that the distribution of $\log_{10} y_7^{th}$ is fit by a Gaussian slightly better than the distribution of y_7^{th} . And because of the very poor observational data on ${}^6\text{Li}$ (see Sec. 3.4), there is no reason to be concerned with the theoretical p.d.f for ${}^6\text{Li}$, although it too is approximately Gaussian.

In practice, I use 1,000 Monte-Carlo points for each value of $(\tau_X, m_X Y_X, \eta)$ in order to obtain consistent results from simulation to simulation. Total CPU time for the entire $(\tau_X, m_X Y_X, \eta)$ parameter space (*viz.*, $31 \times 41 \times 12$ points, for $10^3 \text{ sec} \leq \tau_X \leq 10^9 \text{ sec}$, $10^{-17} \text{ GeV} \leq m_X Y_X \leq 10^{-7} \text{ GeV}$, $7.94 \times 10^{-11} \leq \eta \leq 10^{-9}$) was 118 days.

However, it has recently been demonstrated that the uncertainties in SBBN can be quantified by the much quicker method of linear propagation of errors (LPE) [57]. As a function of the parameters $\mathbf{p} = (\tau_X, m_X Y_X, \eta)$ of the theory, I approximate the change Δa_i in the abundances $a_i = (y_2, y_3, Y, \log_{10} y_7)$, when the nuclear and photofission reaction rates r_α are changed by Δr_α , as

$$\Delta a_i(\mathbf{p}) = a_i(\mathbf{p}) \sum_{\alpha} \lambda_{i\alpha}(\mathbf{p}) \frac{\Delta r_\alpha}{r_\alpha} \quad (2.7)$$

where

$$\lambda_{i\alpha}(\mathbf{p}) = \frac{\partial \ln a_i(\mathbf{p})}{\partial r_\alpha}. \quad (2.8)$$

The error matrix (“covariance matrix”) for the abundances is then

$$[\sigma^2]_{ij} = a_i(\mathbf{p}) a_j(\mathbf{p}) \sum_{\alpha} \lambda_{i\alpha}(\mathbf{p}) \lambda_{j\alpha}(\mathbf{p}) \left(\frac{\Delta r_\alpha}{r_\alpha} \right)^2. \quad (2.9)$$

The diagonal elements of $[\sigma^2]_{ij}$ are the variances in the abundances of the elements; the off-diagonal elements are related to the linear correlation coefficients $\rho_{ij} = [\sigma^2]_{ij} / \sqrt{[\sigma^2]_{ii} [\sigma^2]_{jj}}$.

With this method, I compute far fewer than the 1,000 points in reaction space $\{r_\alpha\}$ (for each value of $\mathbf{p} = (\tau_X, m_X Y_X, \eta)$) than I need in the Monte-Carlo method. Instead, I need only the abundances for the unperturbed reaction rates (one point),

and the partial derivatives of the abundances with respect to each reaction (two points per reaction):

$$\lambda_{i\alpha} \frac{\Delta r_\alpha}{r_\alpha} = a_i(r_\alpha + \Delta r_\alpha) - a_i(r_\alpha - \Delta r_\alpha) / 2a_i(r_\alpha). \quad (2.10)$$

Since I am including the uncertainties in 27 nucleosynthesis and photofission reactions, I only need to compute $2 \times 27 + 1$ points for each value of \mathbf{p} . This results in a considerable saving of CPU time.

The method of LPE assumes that $\frac{\Delta r_\alpha}{r_\alpha}$ is both small and temperature-independent. As can be seen in Tables 1.1 and 2.2, the one-sigma uncertainties Δr_α are no more than 10% of the r_α , except for the temperature-dependent reactions ${}^3\text{H}(\alpha, \gamma){}^7\text{Li}$ and ${}^3\text{He}(\alpha, \gamma){}^7\text{Be}$. Moreover, $\frac{\Delta r_\alpha}{r_\alpha}$ is independent of temperature for all reactions except ${}^3\text{H}(\alpha, \gamma){}^7\text{Li}$ and ${}^3\text{He}(\alpha, \gamma){}^7\text{Be}$. In my BBN simulation, I use a temperature-dependent $\frac{\Delta r_\alpha}{r_\alpha}$ for these two reactions to calculate $[\sigma^2]_{ij}$; in effect, I average over the thermal history of the early universe. (Namely, I compute $\lambda_{i\alpha}$ by using Eqn. 2.10.) Because the two temperature-dependent reactions do not satisfy the assumptions of LPE, I justify this method *a posteriori* by comparing its results to the results of the Monte-Carlo. In fact, my numerical calculations show that the uncertainties computed using LPE differ by less than 10% from the uncertainties computed using the Monte-Carlo throughout the theoretical parameter space⁴ for D/H, ${}^3\text{He}/\text{H}$, and ${}^4\text{He}$. For ${}^6\text{Li}$ and ${}^7\text{Li}$, the uncertainties differ by less than 16%. For my purposes, 10% is an acceptable price for the savings in CPU

⁴I have not included the regions of parameter space where the errors are so small that round-off error dominates.

time. Although LPE does not work as well for lithium, the observational errors for this element are far more important than the theoretical error.

Often in the literature, correlations between elements are neglected. *A priori*, this is not justified [56], because the off-diagonal elements of $[\sigma^2]_{ij}$ can be of the same order of magnitude as the diagonal elements, although they are often much smaller. To investigate this problem, I perform my statistical analysis comparing my theoretical calculations to the observational data, including the correlations between elements, and then I repeat the analysis neglecting the correlations (in effect, I set $[\sigma^2]_{ij} = 0$ for $i \neq j$). I find that the two analyses yield substantially the same results, thus justifying the conventional wisdom that the correlations may be neglected. Namely, I find that throughout the parameter space of $(\tau_X, m_X Y_X, \eta)$, the difference between the two cases in the confidence level (C.L.) at which theory disagrees with observation, is less than 0.3%. The reason for this close agreement between the two cases, despite regions where the correlations are not negligible, is that the correlations are significant only where theory differs from observation by many standard deviations, so that the confidence level is extremely close to 100%. When correlations are neglected, theory and observation still disagree by many standard deviations, and the C.L. is still very close to 100%.

I will discuss my method of analysis in greater detail in Ch. 4. And in Ch. 5, I will give the results of my analysis, based upon the D and ^3He abundance data from solar-system measurements. But first, I consider the other light-element measurements, including the measurements of D/H from quasar absorption systems.

Figure 2.1: Photon spectrum $f_\gamma = dn_\gamma/dE_\gamma$ for several background temperatures T_γ^{BG} .

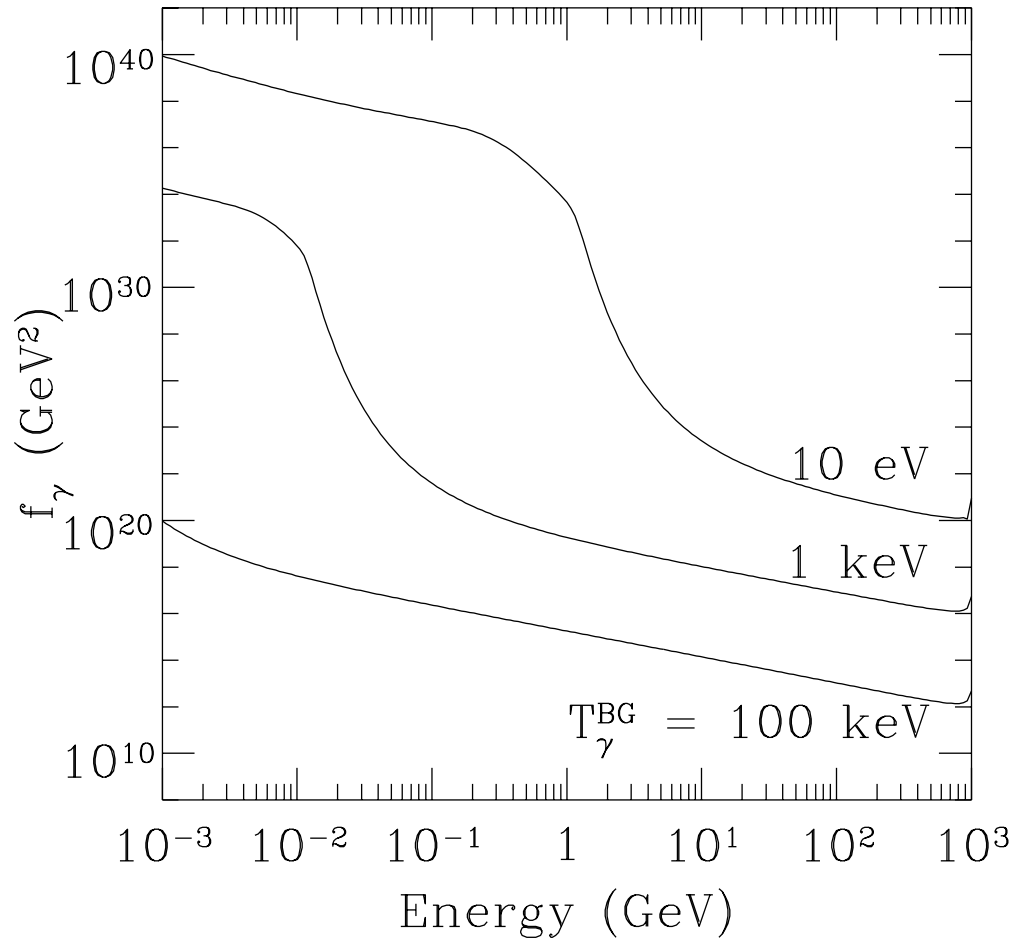


Figure 2.2: Abundance of D in the $m_X Y_X$ vs. τ_X plane with (a) $\eta = 2 \times 10^{-10}$, (b) $\eta = 4 \times 10^{-10}$, (c) $\eta = 5 \times 10^{-10}$, and (d) $\eta = 6 \times 10^{-10}$.

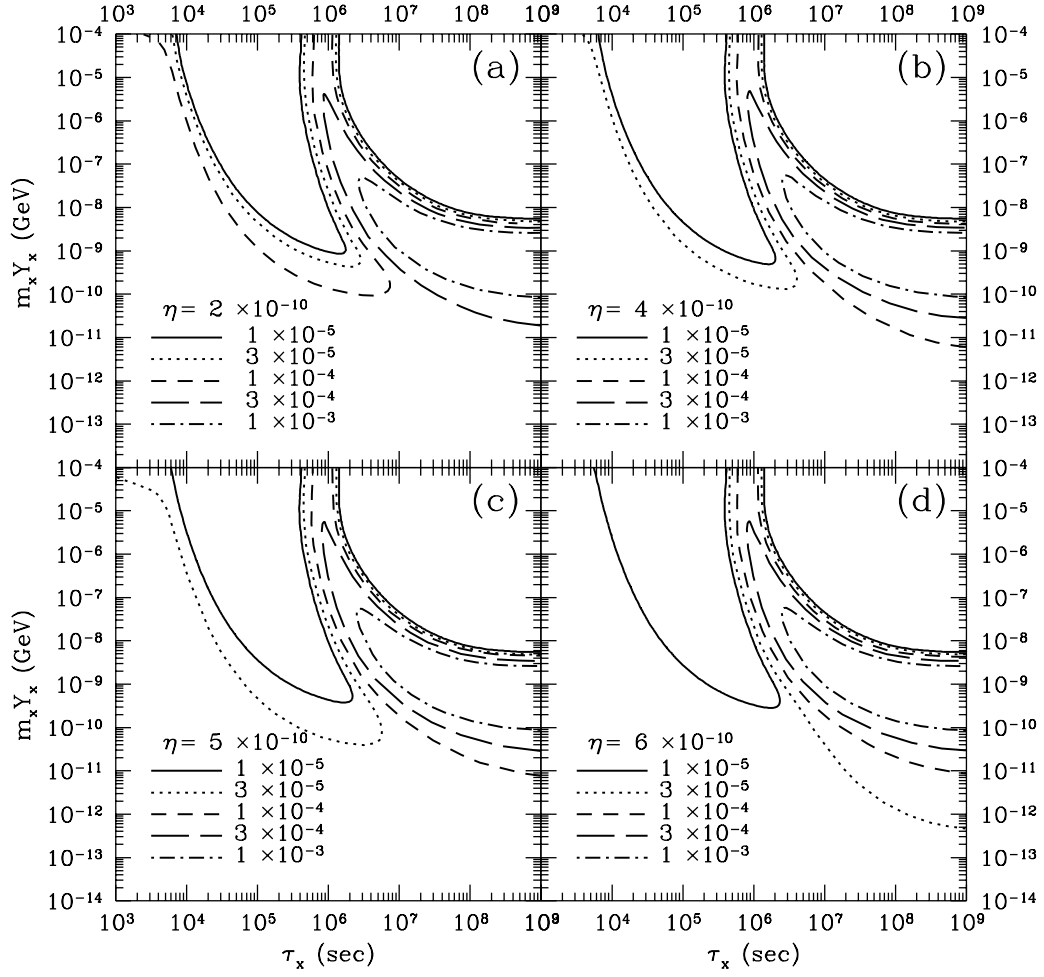


Figure 2.3: Same as Fig. 2.2, except for ${}^3\text{He}$.

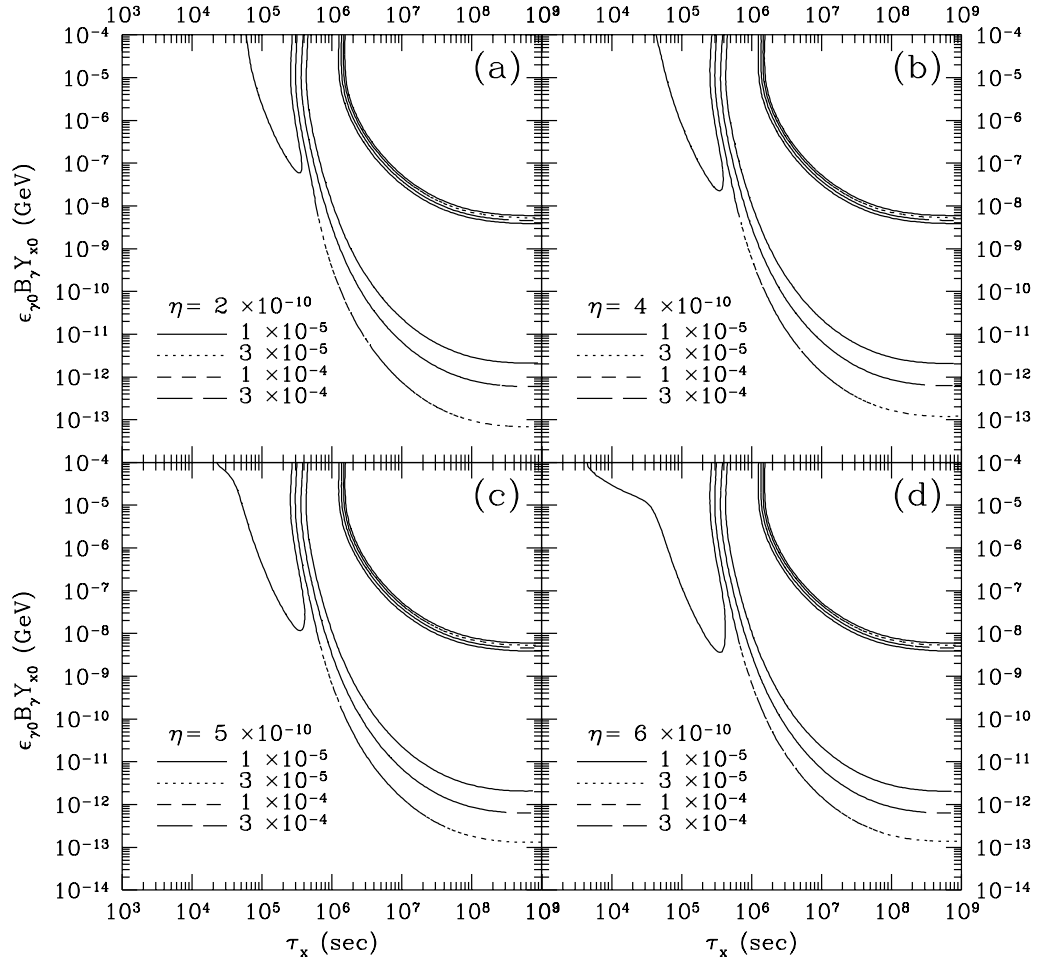


Figure 2.4: Same as Fig. 2.2, except for ${}^4\text{He}$.

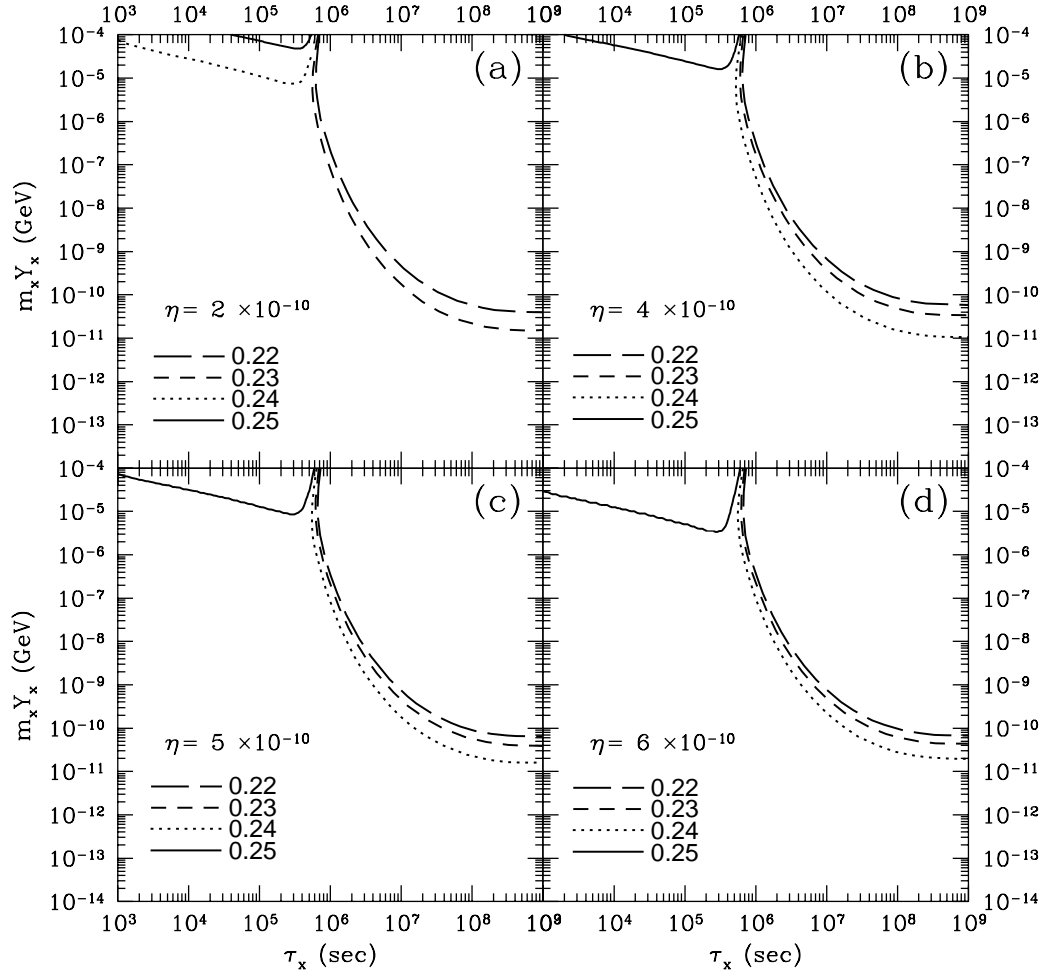


Figure 2.5: Same as Fig. 2.2, except for ${}^6\text{Li}$.

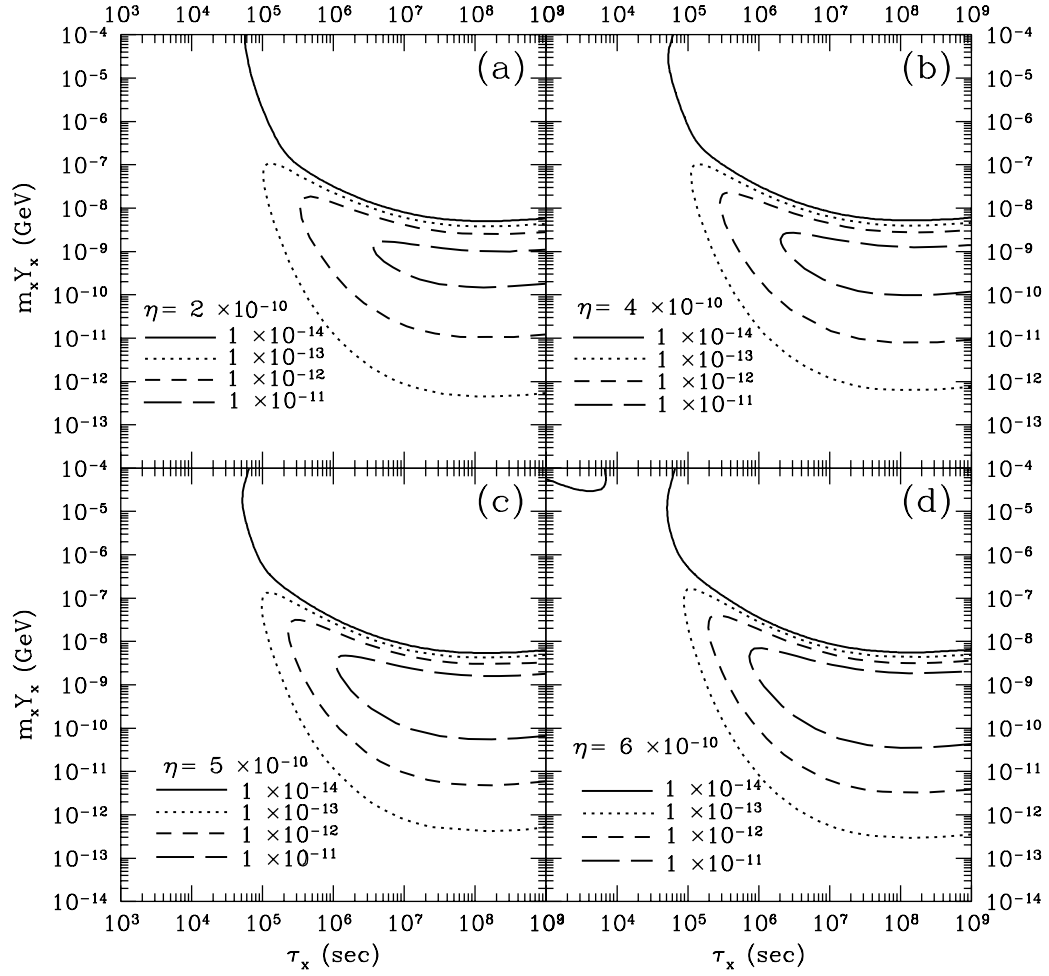
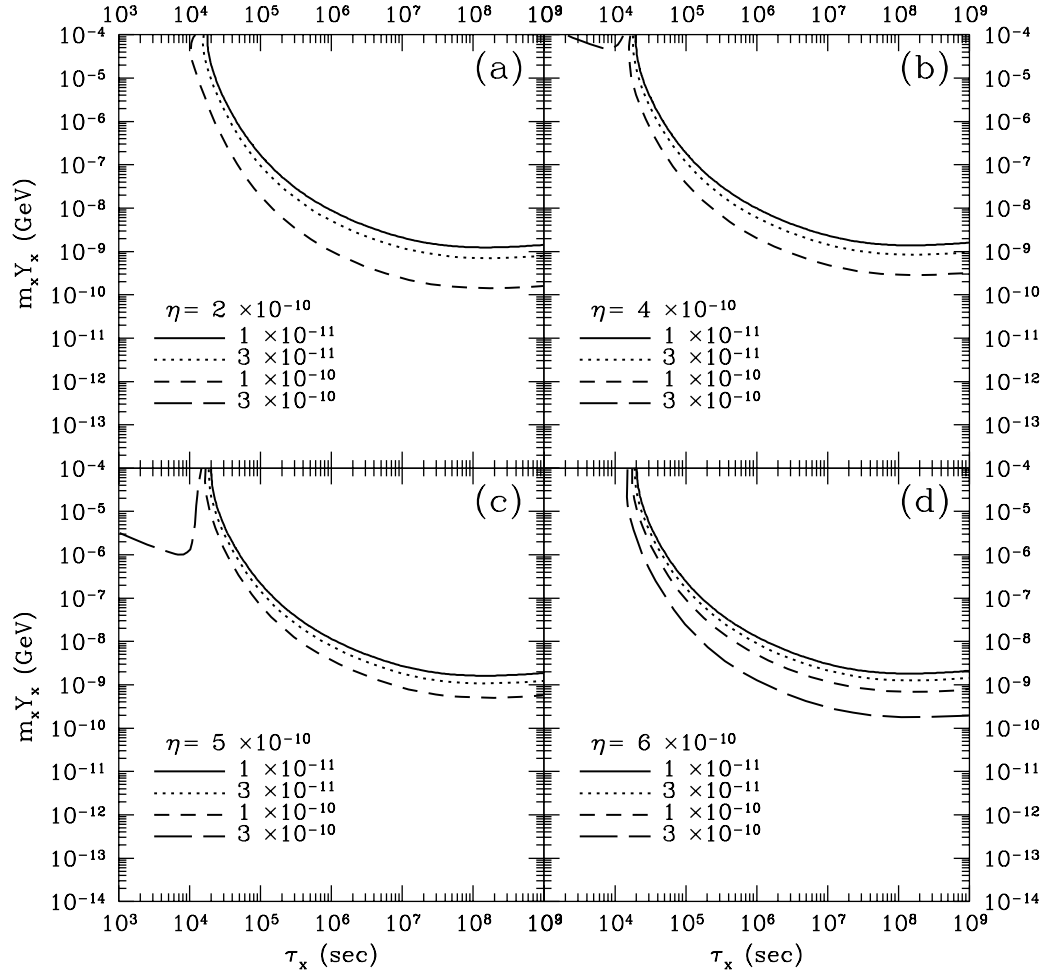


Figure 2.6: Same as Fig. 2.2, except for ${}^7\text{Li}$.



Chapter 3

Observed Light-Element Abundances

I now review the observations of the light-element abundances. Two factors complicate the interpretation of the observations of the light-element abundances. First, there are several observational results (both for D/H and for ^4He) that are not consistent with each other, within the quoted errors. This fact suggests that some groups have underestimated their systematic error.¹ Deuterium has special problems in this regard; hence, in this chapter, I will discuss only the quasar absorption system (QAS) measurements of deuterium. (I will discuss other observations of deuterium in Ch. 5.) I believe it is premature to judge which measurements of D/H and ^4He are most reliable; hence, I consider all possible combinations of the observations when I test the consistency between theory and observation. Second, some guesswork is involved in the extrapolation from the observed values back to the primordial values, as I shall discuss below. Keeping these factors in mind, I review the estimations of the primordial abundances of D, ^4He , ^6Li , and ^7Li .

¹It is also possible that primordial nucleosynthesis was truly inhomogeneous [58]. This inhomogeneous case with a late-decaying particle has been discussed in the literature [59]. However, in this work I adopt the conventional belief that BBN was homogeneous.

3.1 D/H in Quasar Absorption Systems

D/H has been measured in the absorption lines of highly red-shifted (and therefore presumably primordial) H_I (neutral hydrogen) clouds that are backlit by quasars. However, the D/H measurements from these QAS generally fall into two classes, *viz.*, high and low, that differ by almost an order of magnitude.

The first three measurements (all in the direction of QSO 0014+813) were high [60, 61, 62], in the range $y_2 \equiv n_\text{D}/n_\text{H} = (1.9 - 2.5) \times 10^{-4}$. Since these original observations, there have been additional measurements [63, 64] of high D/H in this and other QAS. However, Carswell *et al.* state that there is a significant likelihood that their “deuterium” may actually be Doppler-shifted hydrogen [61] in an interloping H_I cloud. Steigman [65] claims that this may be the case in other measurements as well, although Rugers and Hogan [62] say that an interloper is very unlikely. Finally, Tytler, Burles, and Kirkman [66] reobserved QSO 0014+813 and found that their higher-quality data yield a very large uncertainty in D/H.

On the other hand, Tytler *et al.* [67] have found much smaller values of D/H, *viz.* $y_2 \sim (2.4 \pm 0.4) \times 10^{-5}$ in the directions of QSO 1937-1009 and QSO 1009-2956. However, a reanalysis [68] of Tytler’s QSO 1937-1009 data yields a much higher D/H value. Similarly, new data for QSO 1937-1009 [69] also yield higher D/H.

The weight of opinion in the astrophysics community seems to favor the low values of Tytler *et al.*, because they have observed more QAS and seem to have

higher-resolution spectrographs. In personal communications with the author, S. Burles stated that he believed his lower value was correct, while C. Hogan believes that both his own higher value and other groups' lower values are equally plausible. Because the situation still seems unclear, I will perform my analysis for both values.

For the low value of D/H, I use the recent determination of Burles and Tytler [70]. This value is slightly higher than their original measurement, because they use an improved model of the cloud and have a better measurement of the neutral hydrogen:

$$\text{Low: } y_2^{obs} = (3.39 \pm 0.25) \times 10^{-5}. \quad (3.1)$$

I take the high value of D/H from Rugers and Hogan [62]:

$$\text{High: } y_2^{obs} = (1.9 \pm 0.5) \times 10^{-4}. \quad (3.2)$$

I have plotted both of these one- σ ranges as black boxes on the theoretical curve of D/H as a function of η in Fig. 1.2. The high D/H value favors $\eta \simeq 1 \times 10^{-10}$, while the low value favors $\eta \simeq 5 \times 10^{-10}$.

In this chapter, I do not consider the proto-solar and interstellar-medium measurements of D and ^3He . Because of the difficulty involved in extrapolating back to the primordial abundances, I will defer discussion of these observations until Ch. 5.

3.2 ^4He

The primordial ${}^4\text{He}$ abundance is deduced from observations of extragalactic H_{II} regions (clouds of ionized hydrogen). Currently, there are two classes of $Y^{obs} = \rho_{{}^4\text{He}}/\rho_{\text{baryon}}$ reported by several independent groups of observers. Hence, I consider two cases: one low and one high.

I take my low ${}^4\text{He}$ abundance from Olive, Skillman, and Steigman [41]. They used measurements of ${}^4\text{He}$ and O/H in 62 extragalactic H_{II} regions, and linearly extrapolated back to $\text{O}/\text{H} = 0$ to deduce the primordial value:

$$\text{Low: } Y^{obs} = 0.234 \pm (0.002)_{stat} \pm (0.005)_{syst}. \quad (3.3)$$

(When they restrict their data set to only the lowest metallicity data, they obtain $Y^{obs} = 0.230 \pm 0.003$.) Their systematic error comes from numerous sources, but they claim that no source is expected to be much more than 2%. In particular, they estimate that stellar absorption is of order 1% or less.

I take my high ${}^4\text{He}$ abundance from Thuan and Izotov [43]. They used measurements of ${}^4\text{He}$ and O/H in a new sample of 45 blue compact dwarf galaxies to obtain

$$\text{High: } Y^{obs} = 0.244 \pm (0.002)_{stat} \pm (0.005)_{syst}. \quad (3.4)$$

The last error is an estimate of the systematic error taken from Izotov, Thuan, and Lipovetsky [44]. Thuan and Izotov claim that He_{I} stellar absorption is an important effect; this explains some of the difference between their result and that of Olive, Skillman, and Steigman.

Rather than attempting to judge which group has done a better job of choosing

their sample and correcting for systematic errors, I prefer to remain open-minded. Hence, I shall use both the high and low ${}^4\text{He}$ abundances, without expressing a preference for one over the other. Fig. 1.2 shows both of the one- σ ranges for ${}^4\text{He}$ as boxes on the ${}^4\text{He}$ *vs.* η curve. The high ${}^4\text{He}$ measurement favors $\eta \simeq 1 - 3 \times 10^{-10}$, while the low measurement favors $\eta \simeq 2 - 7 \times 10^{-10}$. Although both the high and low abundance have the same uncertainties, the high value leads to a much larger uncertainty in η , because the ${}^4\text{He}$ *vs.* η curve flattens out for high η .

3.3 $\log({}^7\text{Li}/\text{H})$

The ${}^7\text{Li}/\text{H}$ abundance is taken from observations of the surfaces of Pop II (old generation) halo stars. ${}^7\text{Li}$ is a fragile isotope and is easily destroyed in the warmer, interior layers of a star. Since more massive (or equivalently, hotter) stars are mixed less, one might hope that the surfaces of old, hot stars consist of primordial material. Indeed, Spite and Spite [71] discovered a “plateau” in the graph of ${}^7\text{Li}$ abundance *vs.* temperature of old halo stars, at high temperature. This plateau is interpreted as evidence that truly primordial ${}^7\text{Li}$ has been detected. Using data from 41 plateau stars, Bonifacio and Molaro [72] determine the primordial value $\log_{10}(y_7^{obs}) = -9.762 \pm (0.012)_{stat} \pm (0.05)_{syst}$. Bonifacio and Molaro argue that the data provide no evidence for ${}^7\text{Li}/\text{H}$ depletion in the stellar atmospheres (caused by, *e.g.*, stellar winds, rotational mixing, or diffusion). However, for my analysis, I shall adopt the more cautious estimate of Hogan [73] that ${}^7\text{Li}$ may have been supplemented (by production in cosmic-ray spallation) or depleted (by

nucleosynthesis in stars) by a factor of two: [74]

$$\log_{10}(y_7^{obs}) = -9.76 \pm (0.012)_{stat} \pm (0.05)_{syst} \pm (0.3)_{factor\ of\ 2}. \quad (3.5)$$

Again, I have plotted the one- σ observational range for ${}^7\text{Li}/\text{H}$ on top of the theoretical abundance curve in Fig. 1.2. Because I have allowed for the possibility of a large, factor-of-two error in ${}^7\text{Li}/\text{H}$, this constraint is much weaker than D/H and ${}^4\text{He}$, and agrees with both the high and low values of both elements. However, even if I had chosen a smaller error for ${}^7\text{Li}/\text{H}$, the trough-shaped theoretical abundance of ${}^7\text{Li}/\text{H}$ would lead to both high and low values of η .

3.4 $\log({}^6\text{Li}/\text{H})$

Because ${}^6\text{Li}$ is so much rarer than ${}^7\text{Li}$, it is much more difficult to observe. Currently, there are insufficient data to find the “Spite plateau” of ${}^6\text{Li}$. However, I can set an upper bound on ${}^6\text{Li}/{}^7\text{Li}$, since it is generally agreed that the evolution of ${}^6\text{Li}$ is dominated by production through spallation (reactions of cosmic rays with the interstellar medium). The upper bounds on ${}^6\text{Li}/{}^7\text{Li}$ observed in low-metallicity ($[\text{Fe}/\text{H}] \leq -2.0$) halo stars² range from [75] $y_6/y_7 \lesssim 0.045$ to $y_6/y_7 \lesssim 0.13$. (Note that the primordial ${}^6\text{Li}$ and ${}^7\text{Li}$ have both been destroyed in material that has been processed by stars and is therefore of higher metallicity.)

Rotational mixing models [76] yield a survival factor for ${}^7\text{Li}$ of order 0.05 and a survival factor for ${}^6\text{Li}$ of order 0.005. Therefore, the upper bound for primordial

²The notation $[\text{Fe}/\text{H}]$ means $\log_{10}(\text{Fe}/\text{H}) - \log_{10}(\text{Fe}/\text{H})_{solar}$.

${}^6\text{Li}/{}^7\text{Li}$ ranges approximately from

$$y_6^{obs}/y_7^{obs} \lesssim 0.5 \text{ to } 1.3. \quad (3.6)$$

Note that this constraint lies well above the theoretical ${}^6\text{Li}/\text{H}$ curve in Fig. 1.2 for the entire range of η . Since I have only a rough range of upper bounds on ${}^6\text{Li}$, and no lower bound, I will not use ${}^6\text{Li}$ in my statistical analysis to test the concordance between observation and theory. Instead, I will just check the consistency of my theoretical results with the above constraint.

Chapter 4

Statistical Analysis of Theory and Observation

In this chapter, I describe how I compare my theoretical calculations from Ch. 2 with the observed abundances from Ch. 3 to arrive at meaningful bounds on the properties of the radiatively-decaying X particle. I dwell at some length on this topic, because there has been confusion in the literature as to how to compare theory and observation, and what such comparisons mean. I then discuss my results.

4.1 Analysis

In this section, I seek to answer the question, “How well does my simulation of BBN agree with the observed light-element abundances?” To be more precise, I rephrase the question as, “At what confidence level is my simulation of BBN excluded by the observed light-element abundances?”

From my Monte-Carlo BBN simulation, I obtain the theoretical probability density function (p.d.f.) $p^{th}(\mathbf{a}^{th})$ of the simulated light-element abundances $\mathbf{a}^{th} = (y_2^{th}, Y^{th}, \log_{10} y_7^{th})$. I find that $p^{th}(\mathbf{a}^{th})$ is well-approximated by the product of independent, Gaussian probability distribution functions. [See Eqs. (2.5) and (2.6).] Note that $p^{th}(\mathbf{a}^{th})$ depends upon the parameters \mathbf{p} of my theory, *e.g.* \mathbf{p}

$= (\eta, \dots)$. (The ellipses refer to parameters in non-standard BBN, *e.g.*, m_X , Y_X and τ_X .) In particular, the means and standard deviations of $p^{th}(\mathbf{a}^{th})$ are functions of \mathbf{p} .

I also construct the p.d.f. $p^{obs}(\mathbf{a}^{obs})$ for the observed light-element abundances, *viz.*, $\mathbf{a}^{obs} = (y_2^{obs}, Y^{obs}, \log_{10} y_7^{obs})$. Since the observations of the light element abundances are independent, I can factor the joint probability density:

$$p^{obs}(\mathbf{a}^{obs}) = p_2^{obs}(y_2^{obs}) \times p_4^{obs}(Y^{obs}) \times p_7^{obs}(\log_{10} y_7^{obs}). \quad (4.1)$$

I assume Gaussian p.d.f.'s for y_2^{obs} , Y^{obs} , and $\log_{10} y_7^{obs}$. I use the mean abundances and standard deviations given in Equations (3.1)–(3.5). Since I have two discordant values of D/H and two discordant values of ^4He , I considered all four cases.

Consider now $\Delta\mathbf{a} = \mathbf{a}^{th} - \mathbf{a}^{obs}$. This quantity has a p.d.f. given by

$$\begin{aligned} p^\Delta(\Delta\mathbf{a}) &= \int d\mathbf{a}^{obs} p^{obs}(\mathbf{a}^{obs}) \int d\mathbf{a}^{th} p^{th}(\mathbf{a}^{th}) \delta(\Delta\mathbf{a} - (\mathbf{a}^{th} - \mathbf{a}^{obs})) \\ &= \int d\mathbf{a} p^{th}(\mathbf{a}) p^{obs}(\mathbf{a} - \Delta\mathbf{a}), \end{aligned} \quad (4.2)$$

where I have suppressed the dependence of $p^\Delta(\Delta\mathbf{a})$ and $p^{th}(\mathbf{a}^{th})$ on the theory parameters \mathbf{p} . Note that when all p_i^{th} and p_i^{obs} are Gaussian, Eq. (4.2) is easily integrated to yield a product of three Gaussian p.d.f.'s.:

$$p^\Delta(\Delta\mathbf{a}) = \prod_i \frac{1}{\sqrt{2\pi}\sigma_i} \exp\left[-\frac{(\Delta a_i - \Delta \bar{a}_i)^2}{2\sigma_i^2}\right], \quad (4.3)$$

where $\Delta \bar{a}_i = \bar{a}_i^{th} - \bar{a}_i^{obs}$, $\sigma_i^2 = (\sigma_i^{th})^2 + (\sigma_i^{obs})^2$ and i runs over $(y_2, Y, \log_{10} y_7)$.

My question can now be rephrased as, “At what confidence level (C.L.) is

$\Delta \mathbf{a} = 0$ excluded?" The answer,

$$\text{C.L.}(\mathbf{p}) = \int_{\{\Delta \mathbf{a}: p^\Delta(\Delta \mathbf{a}; \mathbf{p}) > p^\Delta(0; \mathbf{p})\}} d(\Delta \mathbf{a}) p^\Delta(\Delta \mathbf{a}; \mathbf{p}), \quad (4.4)$$

is used in this dissertation to constrain various scenarios of BBN. Since I have assumed Gaussian p.d.f.'s, I can easily evaluate this integral. The result is conveniently expressed in terms of a χ^2 function of the abundances:

$$\text{C.L.} = \int_0^{\chi^2} \frac{1}{2^{3/2} \Gamma(\frac{3}{2})} y^{\frac{1}{2}} e^{-\frac{y}{2}} dy \quad (4.5)$$

$$= -\sqrt{\frac{2\chi^2}{\pi}} \exp\left(-\frac{\chi^2}{2}\right) + \text{erf}\left(\sqrt{\frac{\chi^2}{2}}\right), \quad (4.6)$$

where

$$\chi^2 = \sum_i \frac{(a_i^{th} - a_i^{obs})^2}{(\sigma_i^{th})^2 + (\sigma_i^{obs})^2}, \quad (4.7)$$

for $a_i = (y_2, Y, \log_{10} y_7)$, and $(\sigma_i^{obs})^2 = (\sigma_i^{sys})^2 + (\sigma_i^{stat})^2$.

The confidence level is calculated for three degrees of freedom Δa_i . It denotes the certainty that a given point \mathbf{p} in the parameter space of the theory is excluded by the observed abundances. In order to compare my theory with a late-decaying particle (three parameters \mathbf{p} : $\tau_X, m_X Y_X$, and η) to a theory with a different number of parameters (*e.g.*, only one in SBBN), one would want to use a χ^2 variable in these parameters. This transformation would be possible if the abundances a_i were linear in the theory parameters \mathbf{p} . In that case, I could integrate out a theory parameter such as η and set a C.L. exclusion limit (with a reduced number of degrees of freedom) on the remaining parameters. However, the a_i turn out to be highly non-linear functions of \mathbf{p} , so integrating out a theory parameter turns

out to have little meaning. Instead, I shall project out various theory parameters (as explained in Section 4.2.1) to present my results as graphs.

4.2 Results

As I mentioned in Section 3.1, I have two ${}^4\text{He}$ values that have been inferred from various observed data to be the primordial components. I also have two primordial D/H values, which are deduced from the spectra of quasar absorption systems (QAS). In this section, I compare the theoretical calculations with these observed abundances and show how I can constrain the model parameters in each of the four cases.

4.2.1 Low ${}^4\text{He}$ ($Y^{obs} = 0.234 \pm (0.002)_{stat} \pm (0.005)_{sys}$)

Recalling that the low observed ${}^4\text{He}$ value [Eq. (3.3)] is consistent with the theoretical calculation at low η in the case of SBBN, I expect that I can obtain rigid constraints on the model parameters for the high observed D/H value [Eq. (3.2)]. On the other hand, for the low observed D/H value [Eq. (3.1)], I search the parameter space for regions of better fit than I can obtain with SBBN.

Low QAS D/H ($y_2^{obs} = (3.39 \pm 0.25) \times 10^{-5}$)

In Fig. 4.1, I show the contours of the confidence level computed using three elements (D, ${}^4\text{He}$, and ${}^7\text{Li}$) for some representative η values (2×10^{-10} , 4×10^{-10} , 5×10^{-10} , 6×10^{-10}). The region of parameter space that is allowed at the 68%

C.L. extends down to low η (see Fig. 4.1a). Near $\eta = 2 \times 10^{-10}$, deuterium is destroyed by an order of magnitude (without net destruction of ${}^4\text{He}$), so that the remaining deuterium agrees with the calculated low ${}^4\text{He}$. I also plotted the regions excluded by the observational upper bounds on ${}^6\text{Li}/{}^7\text{Li}$. The shaded regions are $y_6/y_7 \gtrsim 0.5$, and the darker shaded regions are $y_6/y_7 \gtrsim 1.3$. Even if I adopt the stronger bound $y_6/y_7 \lesssim 0.5$, my constraints from the other elements are consistent with the observed ${}^6\text{Li}$ value.

In Fig. 4.2, I show the contours of the confidence levels for various lifetimes, $\tau_X = 10^4, 10^5, 10^6$ sec. As the lifetime decreases, the background temperature at the time of decay increases, so the threshold energy of double-photon pair creation decreases. Then, for a fixed $m_X Y_X$, the number of photons contributing to D destruction decreases. Thus, for shorter lifetimes, I need larger $m_X Y_X$ in order to destroy sufficient amounts of D. The observed abundances prefer non-vanishing $m_X Y_X$.

In Fig. 4.3, I show the edges of the projections of the C.L. regions into the $m_X Y_X$ *vs.* τ_X plane. By projection, I mean taking the lowest C.L. value for a fixed point $(\tau_X, m_X Y_X)$ as η varies.

The lower $m_X Y_X$ region, *i.e.*, $m_X Y_X \sim 10^{-14}$ GeV, corresponds to SBBN, since there are not enough high-energy photons to affect the light-element abundances. It is notable that these regions are outside of the 68% C.L. This fact may suggest the existence of a long-lived massive particle X , and may be regarded as a hint of physics beyond the standard model or standard big-bang cosmology.

For example, in Fig. 4.4 I show the predicted abundances of ${}^4\text{He}$, D/H , ${}^7\text{Li}/\text{H}$, and ${}^6\text{Li}/\text{H}$, adopting the model parameters $\tau_X = 10^6$ sec and $m_X Y_X = 5 \times 10^{-10}$ GeV. This point lies within the 68% C.L., as seen in Fig. 4.3. The predicted abundances of ${}^4\text{He}$ and ${}^7\text{Li}$ are nearly the same as in SBBN. Only D is significantly destroyed; its abundance decreases by about 80%. At low $\eta \sim (1.7 - 2.3) \times 10^{-10}$ in this model, the predicted abundances of these three elements agree with the observed values. It is interesting that the produced ${}^6\text{Li}$ abundance can be two orders of magnitude larger than the SBBN prediction in this parameter region. The origin of the observed ${}^6\text{Li}$ abundance ${}^6\text{Li}/\text{H} \sim O(10^{-12})$ is usually explained by cosmic ray spallation; however, my model demonstrates the possibility that ${}^6\text{Li}$ may have been produced by the photodissociation of ${}^7\text{Li}$ at an early epoch. My ${}^6\text{Li}$ prediction is consistent with the upper bound Eq. (3.6).

Although $m_X Y_X \gtrsim 10^{-10}$ GeV is preferred, it is worth noting that SBBN lies within the 95% C.L. agreement between theory and observation. In Fig. 4.3, the 95% bound for $\tau_X \lesssim 10^6$ sec comes from the constraint that not much more than 90% of the deuterium should be destroyed; for $\tau_X \gtrsim 10^6$ sec the constraint is that deuterium should not be produced from ${}^4\text{He}$ photofission. In Table 4.1, I show the representative values of $m_X Y_X$ that correspond to the 68% and 95% confidence levels respectively, for $\tau_X = 10^4 - 10^9$ sec.

High QAS D/H ($y_2^{obs} = (1.9 \pm 0.5) \times 10^{-4}$)

In the case of low ${}^4\text{He}$ and high D/H, SBBN (*i.e.*, low $m_X Y_X$) works quite well

$\tau_X =$	10^4 sec	10^5 sec	10^6 sec	10^7 sec	10^8 sec	10^9 sec
95% C.L.	9×10^{-6}	9×10^{-9}	1×10^{-9}	7×10^{-11}	2×10^{-12}	7×10^{-13}
68% C.L.	$\{1\} \times 10^{-6}$	$\{1\} \times 10^{-9}$	$\{2\} \times 10^{-10}$			

Table 4.1: Upper or (lower – upper) bound on $m_X Y_X$ in units of GeV for the case of low ${}^4\text{He}$ and low D/H. Note that the C.L. is for three degrees of freedom, and η is varied to give the extreme values for $m_X Y_X$.

for $\eta \sim 2 \times 10^{-10}$. Thus, I expect that I can strongly bound the parameter space of the X -decay model. In Fig. 4.5, I show the 68% and 95% C.L. contours for some representative values of η . At low η , I obtain an upper bound on ${}^4\text{He}$, primarily from the constraint on D/H (Fig. 4.5a).

There are also allowed (at better than the 68% C.L.) regions of parameter space at higher values of η (see Figs. 4.5b–4.5d). These allowed regions lie at $\tau_X \gtrsim 10^6$ sec where a small amount of ${}^4\text{He}$ is broken down into D. However, these allowed regions are small, because the parameters must be finely tuned to target the D/H abundance to $\sim O(10^{-4})$.

In Fig. 4.6, I show the contour plots for some representative τ_X in the same manner as in Fig. 4.2.

In Fig. 4.7, I plot the contours projected along the η axis in a fashion similar to Fig. 4.3. Comparing the constraints on τ_X and $m_X Y_X$ with the case of low D/H (Fig. 4.3), I find that the 95% boundary is moved to higher $m_X Y_X$, for $\tau_X \gtrsim 10^6$ sec. This is because D (produced by ${}^4\text{He}$ destruction) is permitted to be an order of magnitude more abundant than in the case of the low D/H observation. I show the 68% and 95% C.L. upper bounds on $m_X Y_X$ in Table 4.2 for various

$\tau_X =$	10^4 sec	10^5 sec	10^6 sec	10^7 sec	10^8 sec	10^9 sec
95% C.L.	5×10^{-6}	5×10^{-9}	6×10^{-10}	5×10^{-10}	7×10^{-11}	4×10^{-11}
68% C.L.	3×10^{-6}	3×10^{-9}	3×10^{-10}	4×10^{-10}	5×10^{-11}	3×10^{-11}

Table 4.2: Same as Table 4.1, except for low ${}^4\text{He}$ and high D/H.

lifetimes τ_X .

4.2.2 High ${}^4\text{He}$ ($Y^{obs} = 0.244 \pm (0.002)_{stat} \pm (0.005)_{syst}$)

The high observed ${}^4\text{He}$ abundance [Eq. (3.4)] is consistent with the SBBN theoretical calculations for both the low and high observed D/H abundances [Eqs. (3.1) and (3.2)]. Therefore, I expect to be able to constrain the model parameters in both cases.

Low QAS D/H ($y_2^{obs} = (3.39 \pm 0.25) \times 10^{-5}$)

For four representative η values ($2 \times 10^{-10}, 4 \times 10^{-10}, 5 \times 10^{-10}, 6 \times 10^{-10}$), I plot the contours of the confidence level in Fig. 4.8. In Fig. 1.2, one can see that the SBBN calculations agree with the observed abundances for mid-range values of the baryon-to-photon ratio ($\eta \sim 5 \times 10^{-10}$). Thus, the upper bound for $m_X Y_X$ is plotted in Fig. 4.8c. Even at a low η (where the SBBN calculation disagrees with the low observed D/H value), the theoretical calculations can match observed data in the region $10^4 \text{ sec} \lesssim \tau_X \lesssim 10^6 \text{ sec}$ and $m_X Y_X \gtrsim 10^{-10}$ because of the significant destruction of D. In Fig. 4.9, I show the C.L. plots for three typical lifetimes, $\tau_X = 10^4, 10^5, 10^6 \text{ sec}$. Finally, I show the C.L. contours projected along the η

$\tau_X =$	10^4 sec	10^5 sec	10^6 sec	10^7 sec	10^8 sec	10^9 sec
95% C.L.	7×10^{-6}	7×10^{-9}	8×10^{-10}	1×10^{-10}	8×10^{-12}	3×10^{-12}
68% C.L.	5×10^{-6}	5×10^{-9}	6×10^{-10}	8×10^{-11}	4×10^{-12}	2×10^{-12}

Table 4.3: Same as Table 4.1, except for high ${}^4\text{He}$ and low D/H.

axis into the $m_X Y_X$ vs. τ_X plane (Fig. 4.10). Table 4.3 gives the upper bounds on $m_X Y_X$ (in GeV) that correspond to the 68% and 95% C.L., for some typical values of the lifetime.

High QAS D/H ($y_2^{obs} = (1.9 \pm 0.5) \times 10^{-4}$)

As in the low D/H case, I now plot C.L. contours for high D/H for four typical values of η in Fig. 4.11. Since the high ${}^4\text{He}$ and high D/H observed values are consistent with SBBN calculations for low η , I expect to obtain bounds on τ_X and $m_X Y_X$ (e.g., , Fig. 4.11a). In Figs. 4.11b – 4.11d, I see that I also have allowed regions for $\tau_X \gtrsim 10^6$ sec. The reason is same as in the case of low ${}^4\text{He}$ and high D/H; the final D/H abundances are well-balanced between production and destruction.

In Fig. 4.12, I plot the confidence level for $\tau_X = 10^4, 10^5$, and 10^6 sec. The range of preferred η at the 68% C.L. is relatively narrow, compared to the case of high D/H and low ${}^4\text{He}$. This is because the case of high D/H and high ${}^4\text{He}$ is only consistent in SBBN for low values of η , and in the lifetime range $\tau_X \sim 10^4 - 10^6$, the ${}^4\text{He}$ abundance is not affected by the radiative decay of X .

Next, I show the 68% and 95% C.L. contours projected along the η axis

$\tau_X =$	10^4 sec	10^5 sec	10^6 sec	10^7 sec	10^8 sec	10^9 sec
95% C.L.	2×10^{-6}	3×10^{-9}	3×10^{-10}	4×10^{-10}	5×10^{-11}	3×10^{-11}
68% C.L.	5×10^{-7}	6×10^{-10}	7×10^{-11}	2×10^{-11}	1×10^{-11}	2×10^{-11}

Table 4.4: Same as Table 4.1, except for high ${}^4\text{He}$ and high D/H.

(Fig. 4.13). There is a large region between the 68% C.L. and the 95% (for a fixed τ_X) for two reasons. First, the uncertainty in the high observed D/H value is large. Second, the η predicted from the high observed ${}^4\text{He}$ value has a wide spread. The overall shape of the 95% C.L. line is very similar to the case of low ${}^4\text{He}$ and high D/H. This is because the constraint for $\tau_X \gtrsim 10^6$ sec is particularly sensitive only to the observed D/H value.

Just as in the case of low ${}^4\text{He}$, the 95% C.L. contour for the high D/H value extends to higher $m_X Y_X$ than for the low D/H value, because the new D component produced by ${}^4\text{He}$ destruction is allowed to be one order of magnitude larger than in the case of low D/H. In Table 4.4, I list the upper bounds on $m_X Y_X$ at the 68% and 95% confidence levels, for various values of τ_X .

4.3 Additional Constraints

I now mention additional constraints on my model. First, the the cosmic microwave background radiation (CMBR) was observed by COBE [2] to very closely follow a blackbody spectrum. This gives us a severe constraint on particles with lifetime longer than $\sim 10^6$ sec [77], which is when the double Compton

process $(\gamma + e^- \rightleftharpoons \gamma + \gamma + e^-)$ freezes out [78].¹ After this time, photon number is conserved, so photon injection from a radiatively decaying particle would cause the spectrum of the CMBR to assume a Bose-Einstein distribution with a finite chemical potential μ . COBE [2] observations give us the constraint $|\mu| \lesssim 9.0 \times 10^{-5}$. For small μ , the ratio of the injected to total photon energy density is given by $\delta\rho_\gamma/\rho_\gamma \sim 0.71\mu$. Thus, I have the constraint

$$m_X Y_X \lesssim 6 \times 10^{-10} \text{ GeV} \left(\frac{\tau_X}{10^6 \text{ sec}} \right)^{-\frac{1}{2}} \quad \text{for } 10^6 \text{ sec} \lesssim \tau_X \lesssim 4 \times 10^{10} \text{ sec}. \quad (4.8)$$

Note that for lifetimes τ_X longer than 10^6 sec, the CMBR constraint is comparable to or slightly stricter than the bounds from BBN that I have discussed above.

In this thesis, I have considered only radiative decays, *i.e.*, decays to photons and invisible particles. If X decays to charged leptons, the effect is similar to decay to photons, because the charged leptons also generate soft photons in electromagnetic cascade showers. On the other hand, if X decays only to neutrinos, the constraints becomes much weaker. If, for example, X is the gravitino in the minimal supersymmetric standard model, then it decays into a neutrino and its superpartner, the sneutrino. The emitted neutrinos scatter off the background neutrinos, producing electron-positron pairs that trigger electromagnetic cascades. But because the interaction between the emitted neutrino and the background neutrinos is weak, the destruction of the light elements does not occur very effi-

¹This constraint applies only to particles with lifetime shorter than $\sim 4 \times 10^{10}$ sec, which corresponds to the decoupling time of Compton/inverse Compton scattering. After this time, injected photons do not thermalize with the CMBR.

ciently [79]. On the other hand, if X decays to hadrons, I expect that my bounds would tighten, because hadronic showers could be a significant source of D, ^3He , ^6Li , ^7Li , and ^7Be [10]. In fact, even though I have assumed that X decays only to photons, these photons may convert to hadrons in loop diagrams. Thus, the branching ratio to hadrons is at least of order 1%, if kinematically allowed [11]. Therefore, my photodissociation bounds in this dissertation are conservative.

Figure 4.1: C.L. in the $m_X Y_X$ vs. τ_X plane, for low value of ${}^4\text{He}$ and low value of D/H. I take (a) $\eta = 2 \times 10^{-10}$, (b) $\eta = 4 \times 10^{-10}$, (c) $\eta = 5 \times 10^{-10}$, and (d) $\eta = 6 \times 10^{-10}$. The shaded regions are $y_6/y_7 \gtrsim 0.5$, and the darker shaded regions are $y_6/y_7 \gtrsim 1.3$.

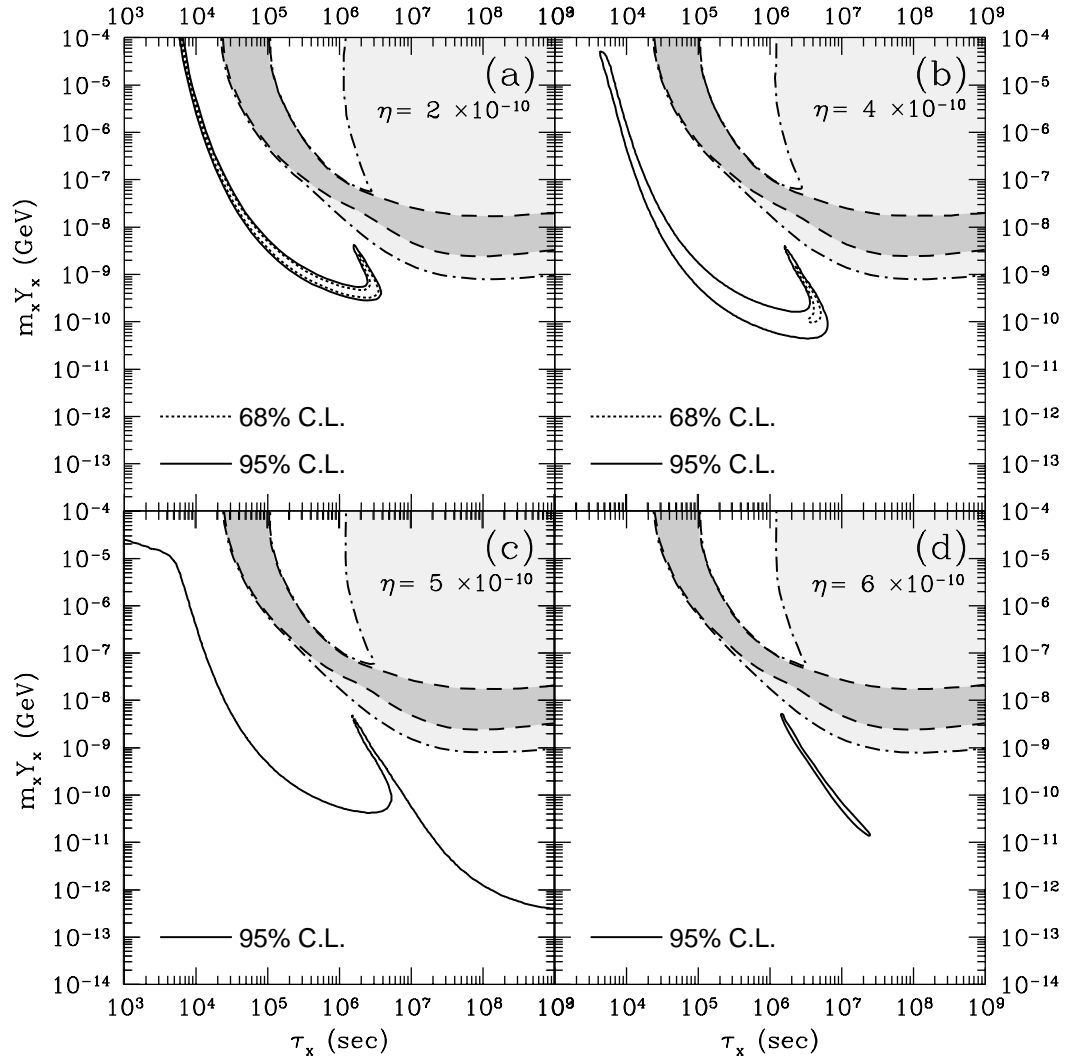


Figure 4.2: C.L. in the $m_X Y_X$ vs. η plane for various values of τ_X , for low value of ${}^4\text{He}$ and low value of D/H.

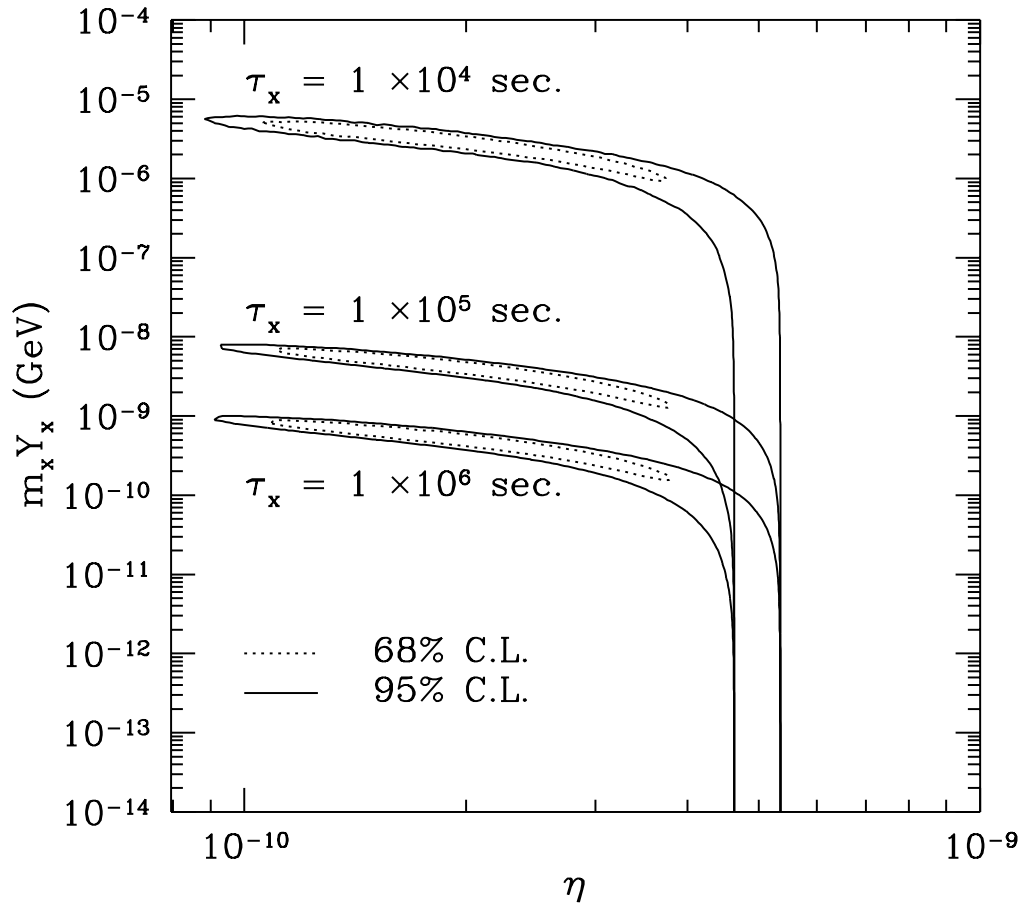


Figure 4.3: Contours of C.L. projected along the η axis, for low value of ${}^4\text{He}$ and low value of D/H .

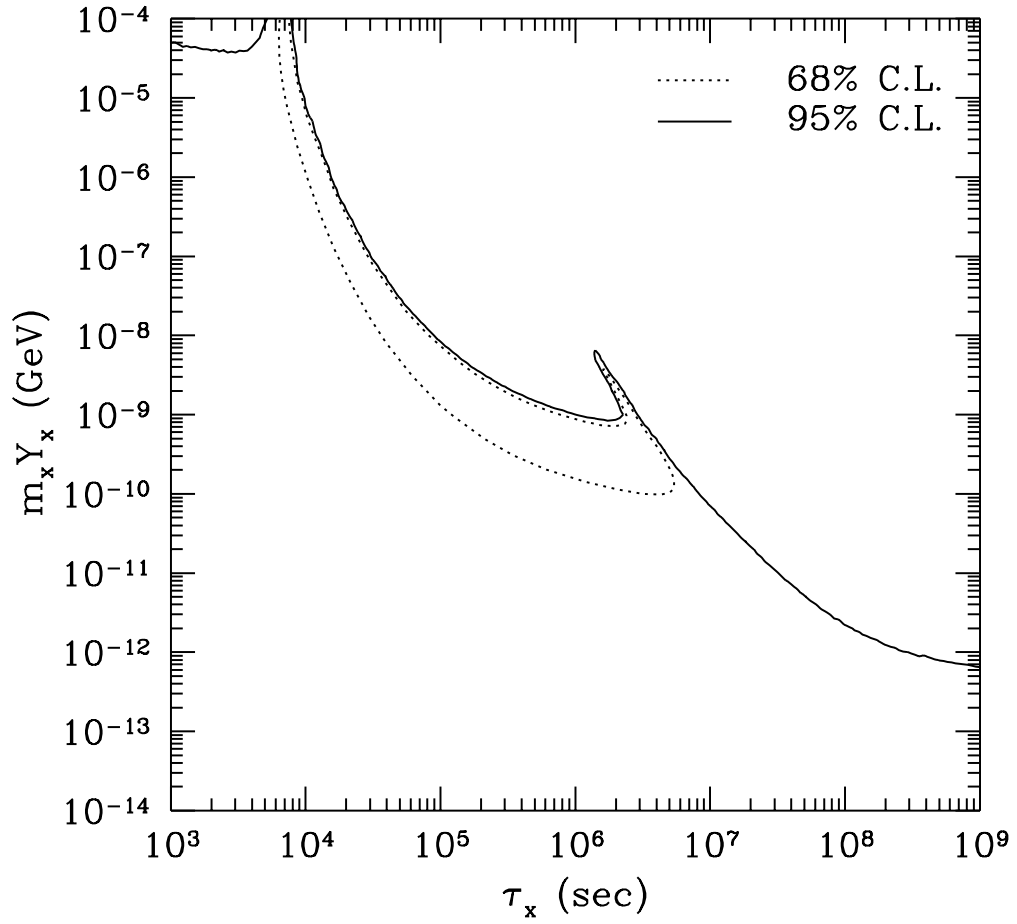


Figure 4.4: Predicted abundances of ${}^4\text{He}$, D/H , ${}^7\text{Li}/\text{H}$ and ${}^6\text{Li}/\text{H}$ at $\tau_X = 10^6$ sec and $m_X Y_X = 5 \times 10^{-10}$ GeV. I have indicated the regions that are favored by the low ${}^4\text{He}$ and low D/H observations. The dotted line denotes the 95% C.L., and the shaded region denotes the 68% C.L. The predicted ${}^6\text{Li}$ abundance is two orders of magnitude larger than it is in SBBN.

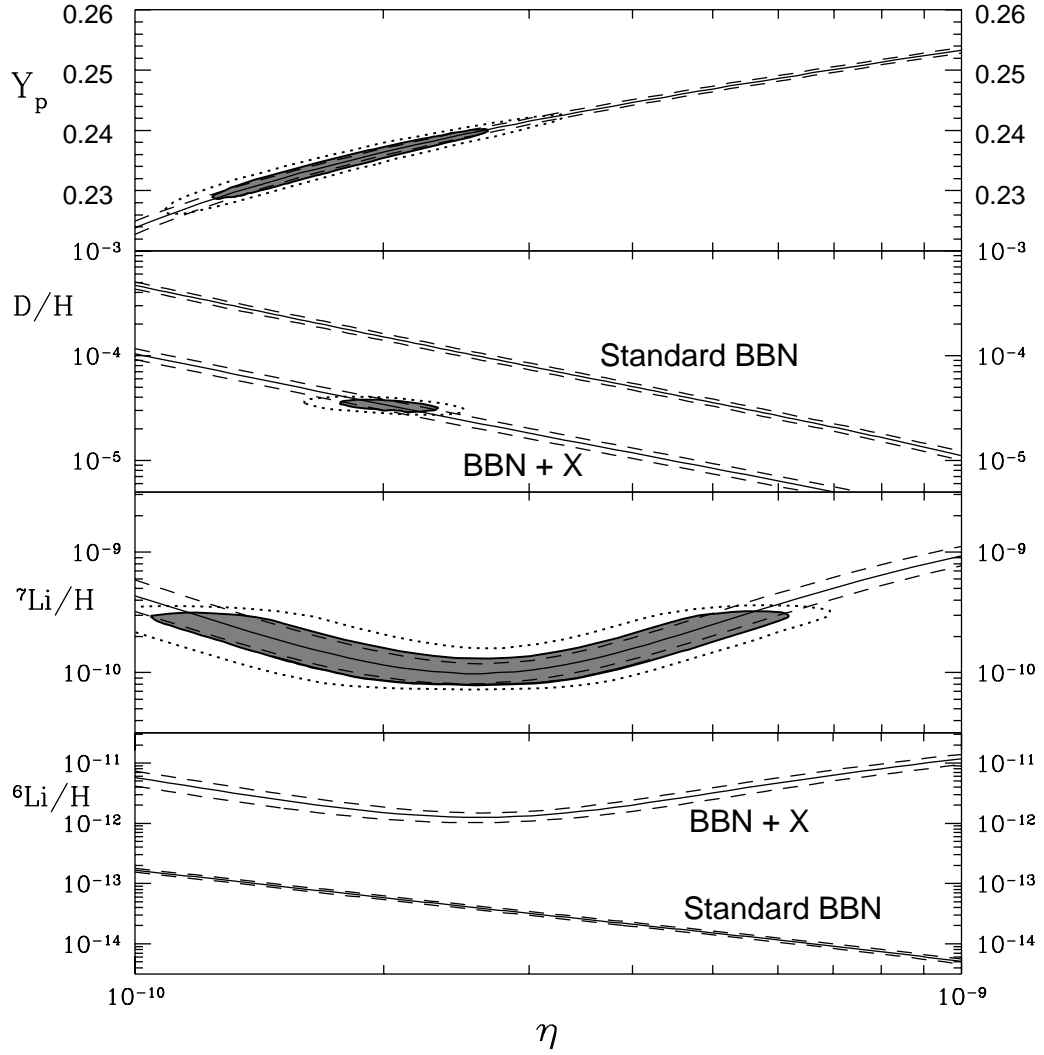


Figure 4.5: Same as Fig. 4.1, except for low value of ${}^4\text{He}$ and high value of D/H .

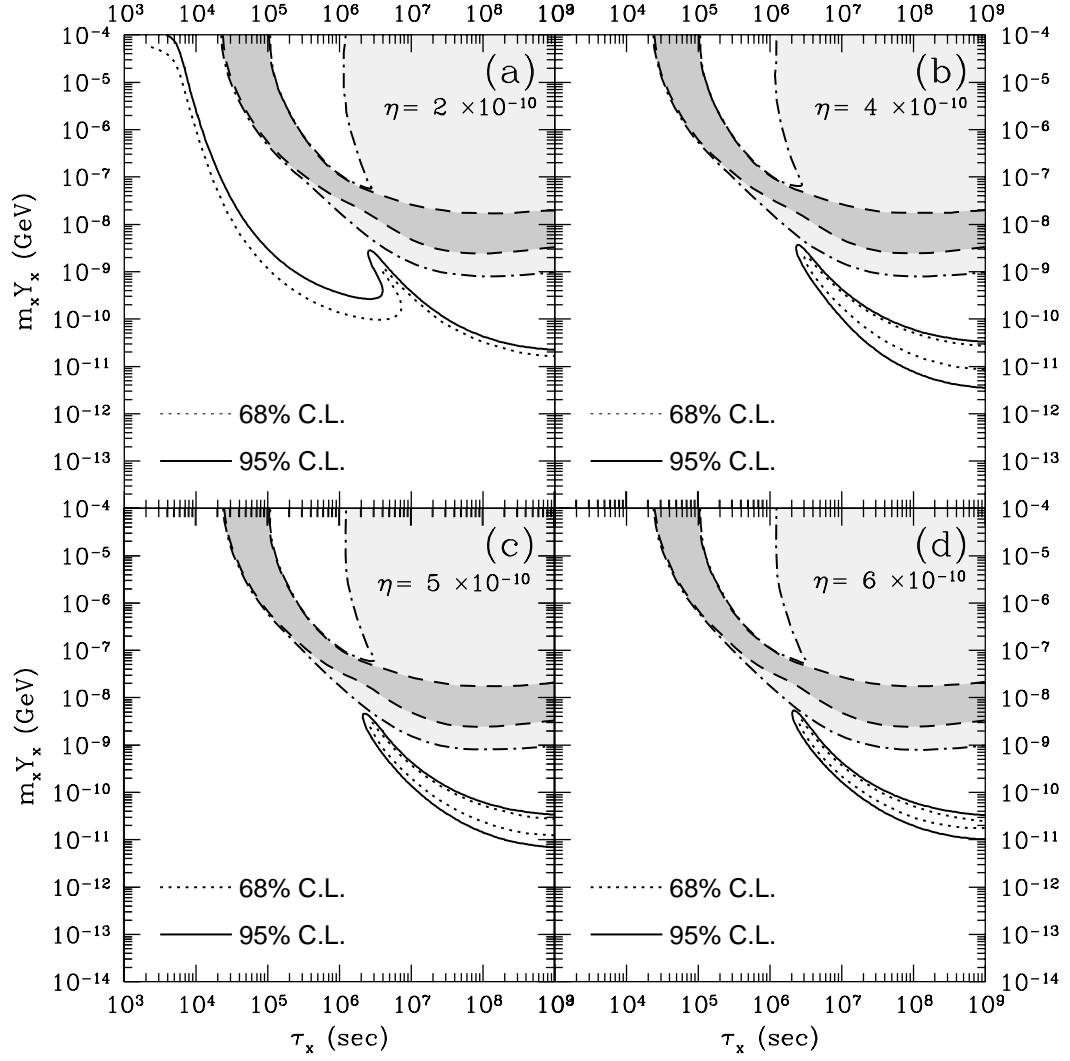


Figure 4.6: Same as Fig. 4.2, except for low value of ${}^4\text{He}$ and high value of D/H .

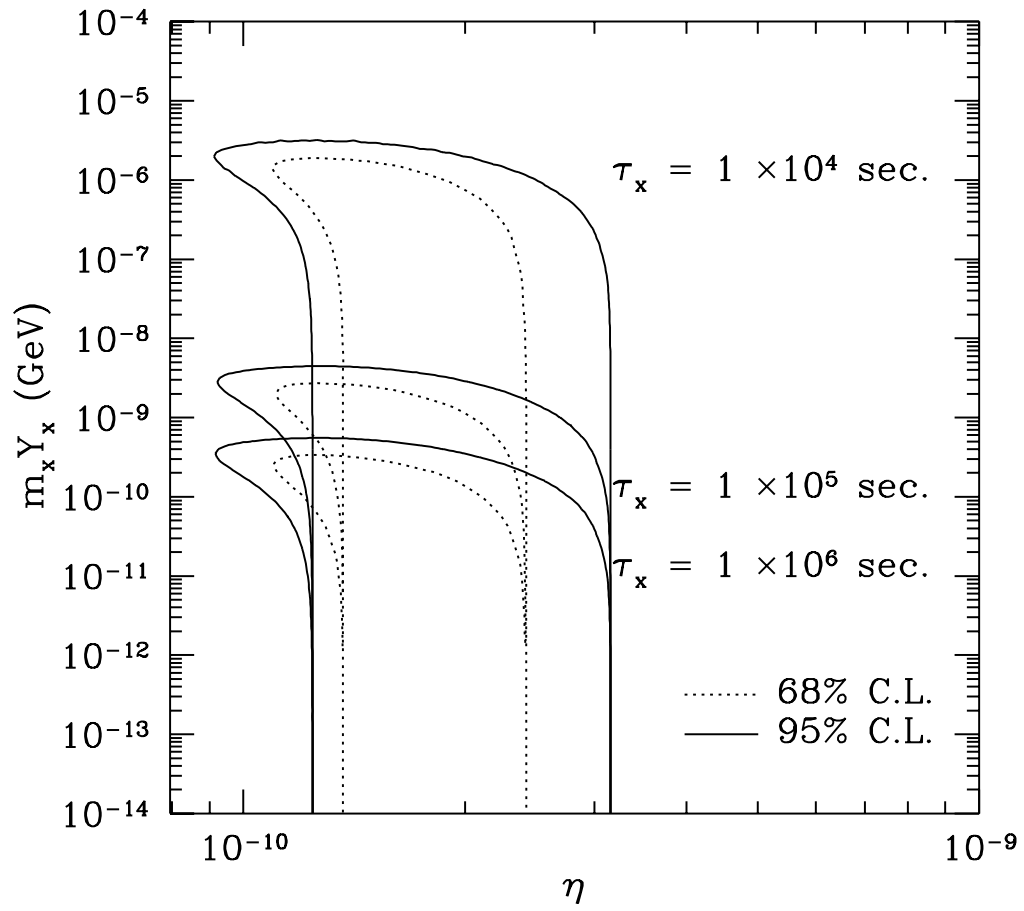


Figure 4.7: Same as Fig. 4.3, except for low value of ${}^4\text{He}$ and high value D/H .

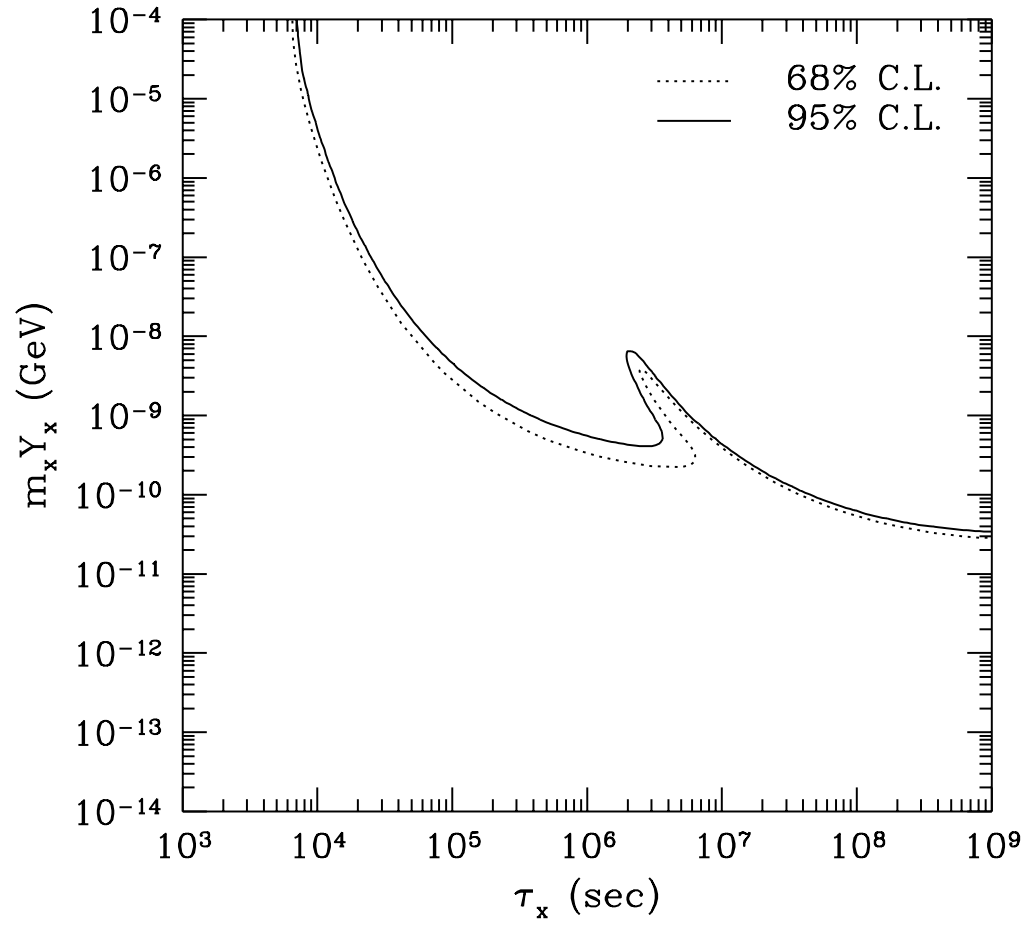


Figure 4.8: Same as Fig. 4.1, except for high value of ${}^4\text{He}$ and low value of D/H .

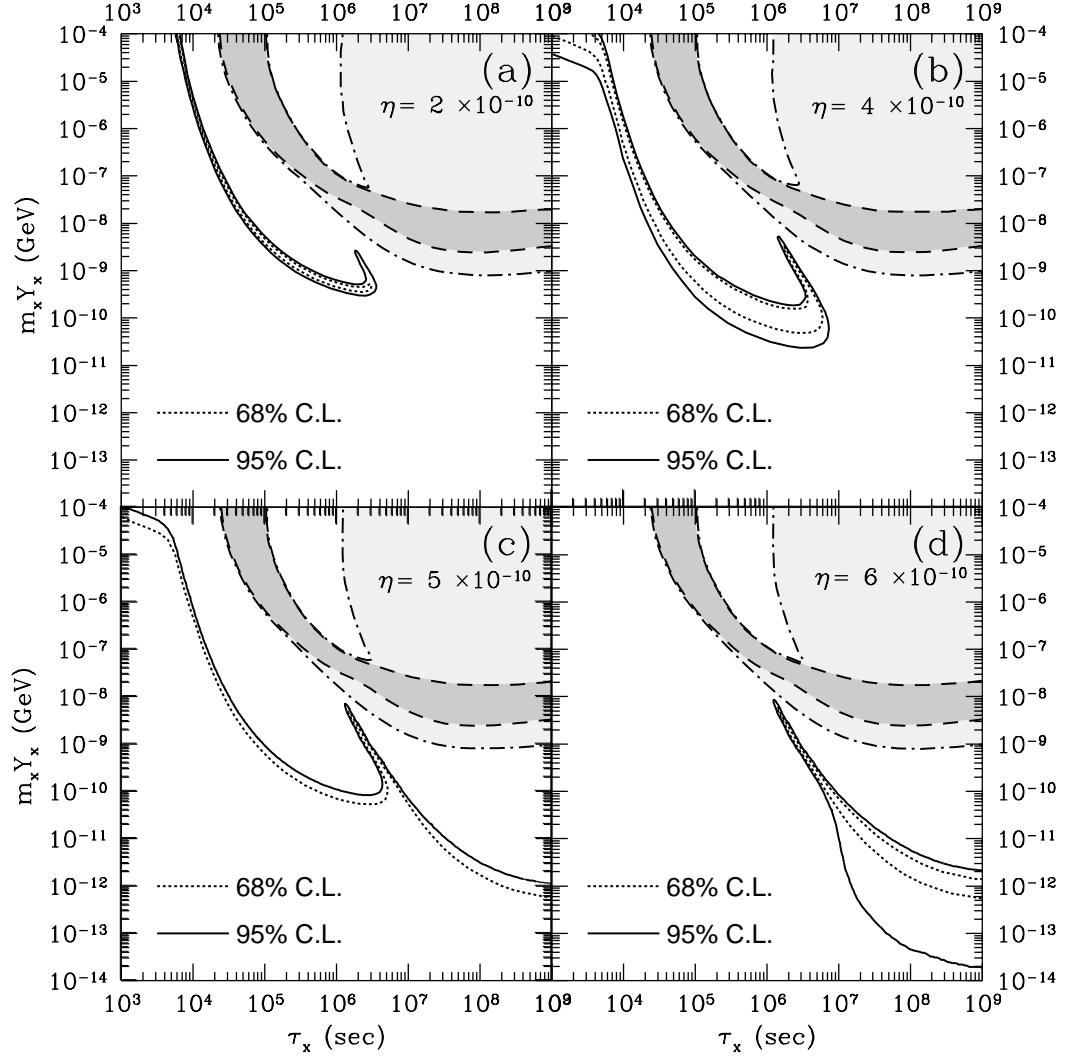


Figure 4.9: Same as Fig. 4.2, except for high value of ${}^4\text{He}$ and low value of D/H .

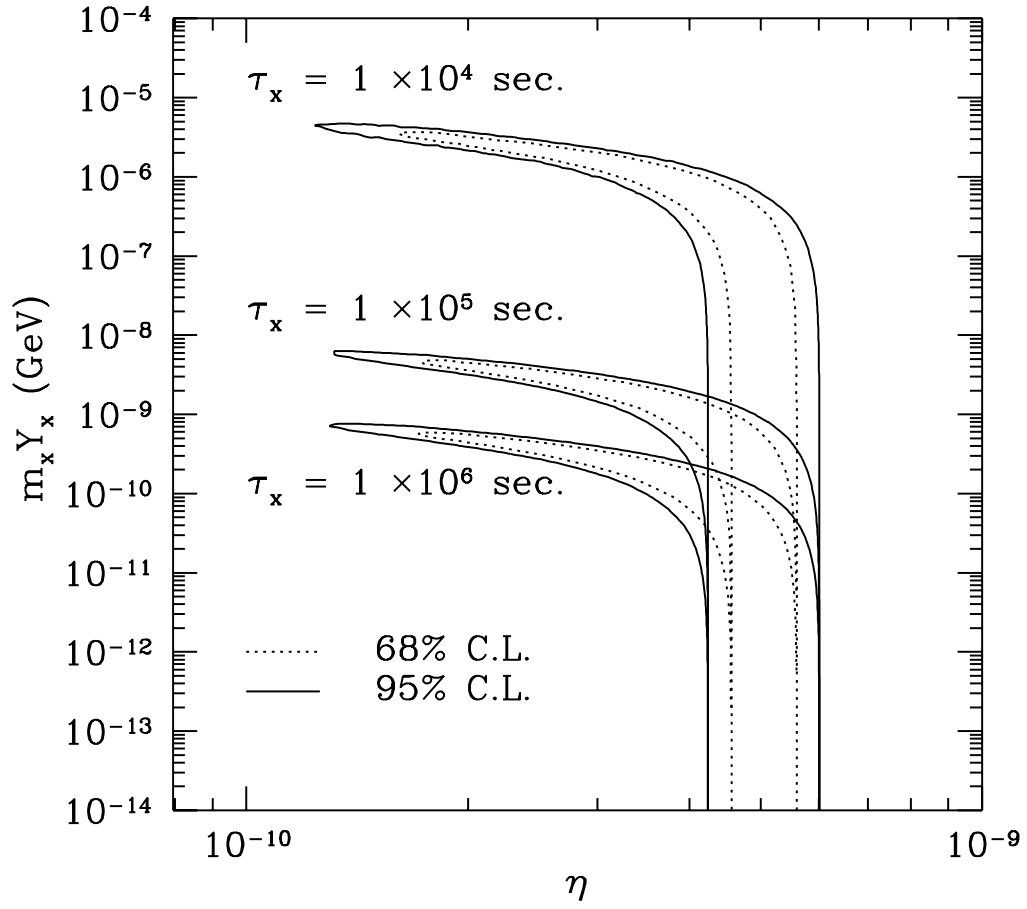


Figure 4.10: Same as Fig. 4.3, except for high value of ${}^4\text{He}$ and low value of D/H .

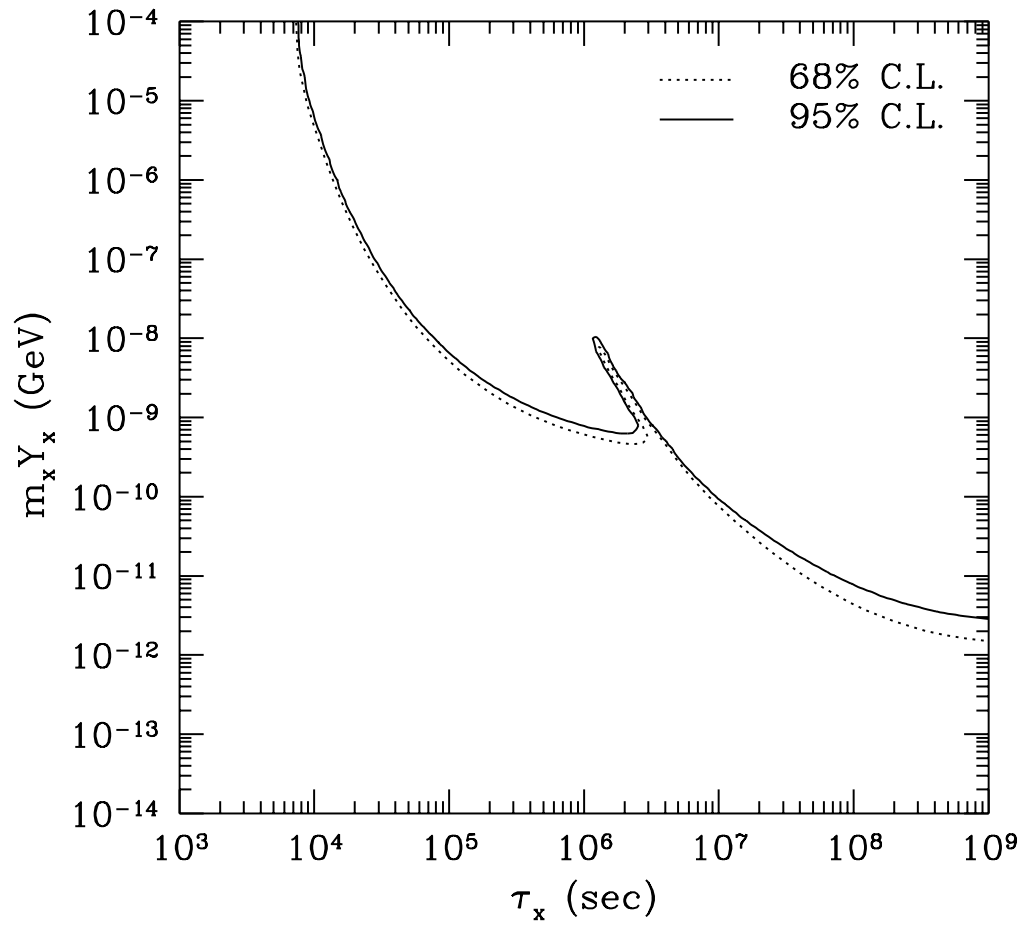


Figure 4.11: Same as Fig. 4.1, except for high value of ${}^4\text{He}$ and high value of D/H .

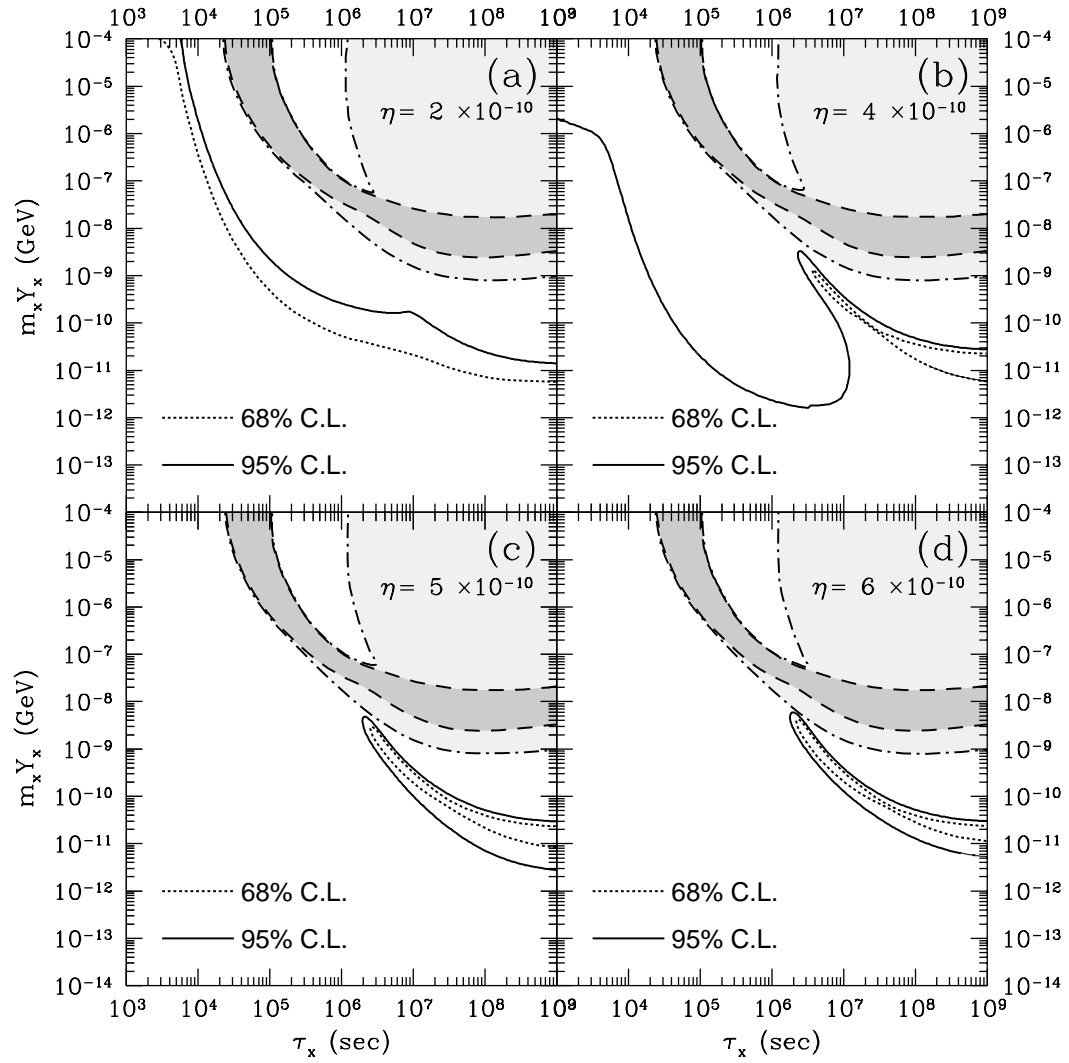


Figure 4.12: Same as Fig. 4.2, except for high value of ${}^4\text{He}$ and high value of D/H .

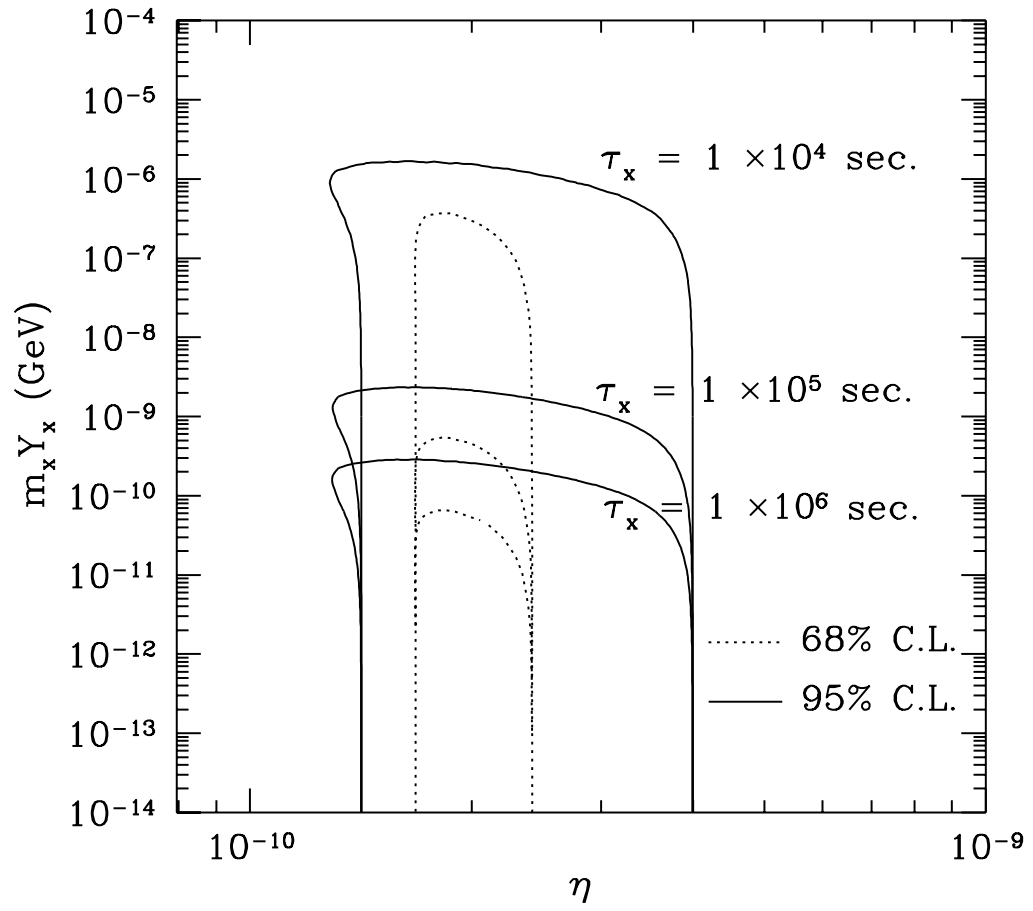
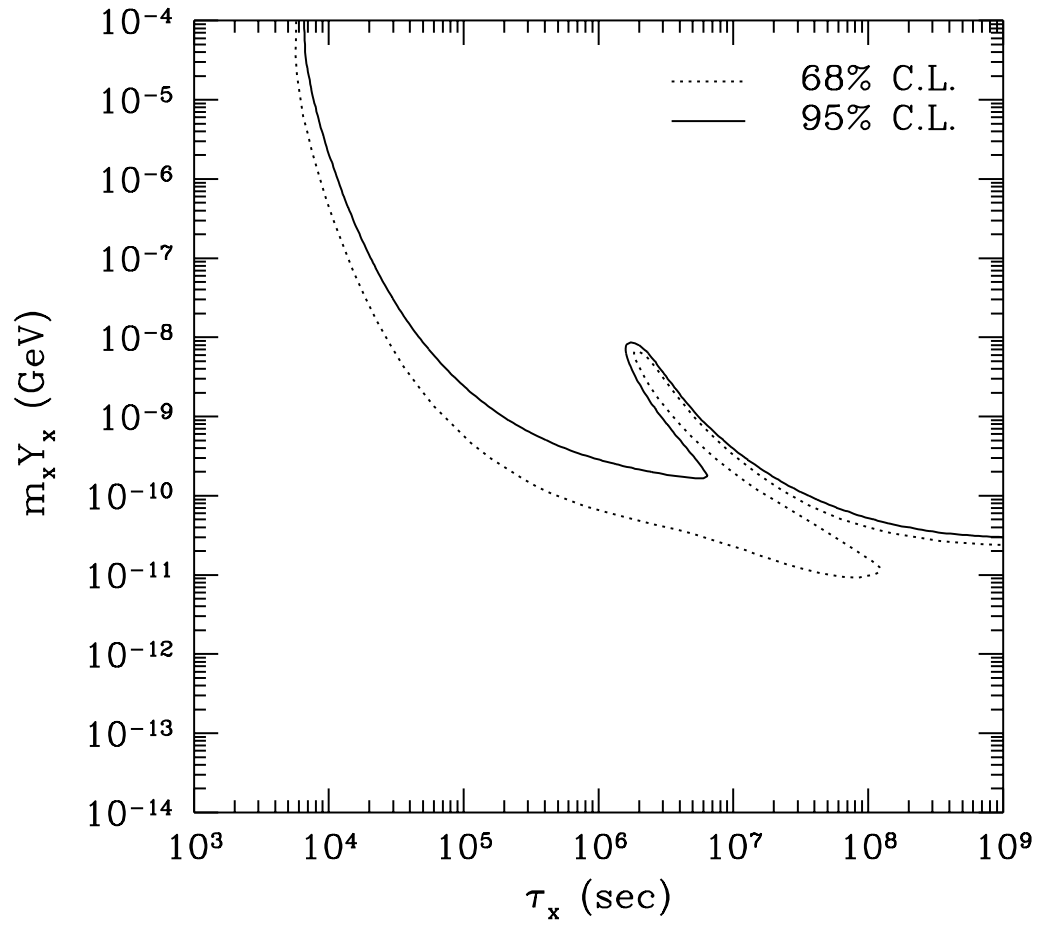


Figure 4.13: Same as Fig. 4.3, except for high value of ${}^4\text{He}$ and high value of D/H .



Chapter 5

Analysis Based on Proto-Solar Observations

In the preceding chapters, I have set BBN constraints on a long-lived, radiatively-decaying particle by comparing the predictions of my theory to the observed light-element abundances. I have taken my deuterium abundance from observations of highly red-shifted quasar absorption systems. However, I was not able to use ^3He , because there are no primordial observations of that isotope. Moreover, the existence of incompatible high and low measurements of deuterium in quasar absorption systems (QAS) casts some doubt on the QAS data.

In this chapter, I will repeat my analysis of BBN with a radiatively decaying particle. However, this time I use proto-solar and interstellar-medium (ISM) observations of D and ^3He (instead of QAS observations of D). Since proto-solar and ISM material is not primordial, I will have to make a few general assumptions about the chemical evolution of D and ^3He . In return for these assumptions, I will get another constraint (^3He) on the parameters $(\tau_X, m_X Y_X, \eta)$ of my theory. I begin by reviewing the proto-solar and ISM measurements of $(\text{D}+^3\text{He})/\text{H}$ and $^3\text{He}/\text{H}$. Next, I explain how I modify my analysis to account for the chemical evolution of D and ^3He . Finally, I present my results (for both high and low ^4He , as in the previous chapter).

5.1 Proto-Solar Data on $(D+{}^3\text{He})/\text{H}$ and ${}^3\text{He}/\text{H}$

Deuterium is very fragile, with a binding energy of just 2.2 MeV. Young stars convert all of their D to ${}^3\text{He}$ through $D(p, \gamma){}^3\text{He}$. Because of this, $(D+{}^3\text{He})/\text{H}$ is an easier quantity to evolve back in time than D/H .

In its pre-main-sequence phase, before ${}^3\text{He}$ began to be converted into ${}^4\text{He}$, the sun was fully convective. All D was mixed down into the warmer, interior layers of the sun, where it was converted into ${}^3\text{He}$. But 30 Myr before the sun became a main-sequence star, the convection zone had shrunk to its present depth, *viz.*, the outer 30% of the sun [80]. Since then, the ${}^3\text{He}/{}^4\text{He}$ ratio on the surface of the sun has remained constant. This ${}^3\text{He}$ on the surface of the sun today is the sum of the proto-solar (indicated by \odot) D and ${}^3\text{He}$:

$$y_{23}^{\odot} \equiv y_2^{\odot} + y_3^{\odot} \quad (5.1)$$

$$= \left(\frac{n_{{}^4\text{He}}}{n_{\text{H}}} \right)_{\odot} \left(\frac{n_{{}^3\text{He}}}{n_{{}^4\text{He}}} \right)_{\text{today}}. \quad (5.2)$$

$({}^3\text{He}/{}^4\text{He})_{\text{today}}$ is measured in the solar wind; the proto-solar ${}^4\text{He}/\text{H}$ is measured in the sun's surface [81]. The resulting value for the proto-solar abundance of D and ${}^3\text{He}$ is [82, 12]

$$y_{23}^{\odot} = (4.09 \pm 0.92) \times 10^{-5}. \quad (5.3)$$

As can be seen in Fig. 1.2, this value (gray box) favors high η , if it is representative of the primordial value.

The proto-solar ${}^3\text{He}/\text{H}$ abundance is taken from trapped gases found in meteorites. One has to be careful to take the “planetary” gases, which originated in

the pre-solar nebula, rather than the “solar” gases, which were captured from the solar wind, and hence have been processed in the sun. I use the value [82, 12]

$$y_3^\odot = (1.52 \pm 0.34) \times 10^{-5}. \quad (5.4)$$

I have plotted the upper bound as gray arrows in Fig. 1.2, since the proto-solar value is likely to be greater than the primordial value. The figure shows that ${}^3\text{He}/\text{H}$ seems to exclude very small η . This is only an intuitive argument; in the next section, I describe my proper analysis that includes the joint evolution of D and ${}^3\text{He}$.

In addition to the proto-solar abundances of D and ${}^3\text{He}$, I will use the interstellar-medium abundance of deuterium in my analysis. This abundance is deduced through measurements of Lyman absorption lines to be [83]

$$y_2^{ism} = (1.6 \pm 0.2) \times 10^{-5}. \quad (5.5)$$

Finally, I need the primordial and proto-solar mass fractions of ${}^1\text{H}$ [12]:

$$X = 0.76 \pm 0.02, \quad (5.6)$$

$$X^\odot = 0.70 \pm 0.02. \quad (5.7)$$

Their ratio is

$$\alpha \equiv X^\odot/X = (0.92 \pm 0.04). \quad (5.8)$$

5.2 Proto-Solar Analysis

As in the QAS analysis in Ch. 4, I will find the confidence level at which my theoretical calculations of the abundances $\mathbf{a}^{th} = (y_2^{th}, y_3^{th}, Y^{th}, \log_{10} y_7^{th})$ agree with the abundances $\mathbf{a}^{obs} = (y_2^{obs}, y_3^{obs}, Y^{obs}, \log_{10} y_7^{obs})$ deduced from observation. The C.L. is again given by the integral (4.4) over the probability distribution function (p.d.f.) $p^\Delta(\Delta\mathbf{a})$ of the difference between the theoretical and observed abundances (see Eq. (4.2)).

Instead of making the standard assumption (as I did in Ch. 4) that the theoretical abundances are independent, here I will allow them to have a general multivariate p.d.f.:

$$p^{th}(\mathbf{a}^{th}; \mathbf{a}^{th}, [\sigma^2]_{ij}) = \left(\frac{1}{\sqrt{2\pi}} \right)^4 \frac{1}{\sqrt{\det([\sigma^2]_{ij})}} \exp \left[-\frac{1}{2} [\mathbf{a}^{th} - \mathbf{a}^{th}]_i [\sigma^{-2}]_{ij} [\mathbf{a}^{th} - \mathbf{a}^{th}]_j \right], \quad (5.9)$$

where $[\sigma^{-2}]_{ij}$ is the inverse of the covariance matrix from Sec. 2.3.

The p.d.f. of the observed abundances is more complicated, because I need to account for the chemical evolution of D and ^3He . However, I can simplify the problem somewhat, because ^4He and ^7Li still have independent, Gaussian p.d.f.'s:

$$p^{obs}(\mathbf{a}^{obs}) = p_{23}(y_2^{obs}, y_3^{obs}) \times p_4^{Gauss}(Y^{obs}) \times p_7^{Gauss}(\log_{10} y_7^{obs}), \quad (5.10)$$

where the means and standard deviations of p_4^{Gauss} and p_7^{Gauss} depend upon the parameters $\mathbf{p} = (\tau_X, m_X Y_X, \eta)$ of the theory. To find the joint p.d.f. of the primordial abundances y_2^{obs} and y_3^{obs} , I use an analysis similar to that of Hata *et al.* [84], which is based on the chemical evolution model of Steigman and Tosi [12,

85]. First, I assume that stars convert all of their deuterium into ^3He . Therefore, the ratio of the proto-solar abundance of D (mass fraction X_2^\odot) to the primordial abundance of D (mass fraction X_2) is equal to the fraction $f \leq 1$ of gas that was never part of a star: $X_2^\odot/X_2 = f$. My second assumption is that an unknown amount of ^3He (primordial mass fraction X_3 , proto-solar mass fraction X_3^\odot) is produced in stars (in excess of the D that is destroyed), and that the amount of ^3He that survives stellar processing and is returned to the interstellar medium is given by the “survival fraction” g_3 , which is plausibly in the range [84]

$$0.25 < g_3 < 0.50. \quad (5.11)$$

This gives me a constraint on the proto-solar ^3He :

$$X_3^\odot \geq fX_3 + (1 - f)g_3(X_3 + 3X_2/2). \quad (5.12)$$

Thus, I derive the following constraints on the primordial abundances y_2^{obs}, y_3^{obs} of D/H and $^3\text{He}/\text{H}$:

$$\alpha y_2^\odot \leq y_2^{obs}, \quad (5.13)$$

$$\begin{aligned} 0 \geq & (y_2^{obs})^2 + (y_3^{obs} - \alpha y_2^\odot - \frac{\alpha y_3^\odot}{g_3}) y_2^{obs} \\ & + y_3^{obs} y_2^\odot \alpha (\frac{1}{g_3} - 1), \end{aligned} \quad (5.14)$$

where $\alpha = X^\odot/X$ is the ratio of the proto-solar and primordial mass fractions of hydrogen. Since D decreases monotonically with time, I also have

$$\alpha y_2^{ism} \leq y_2^{obs}, \quad (5.15)$$

where y_2^{ism} is the present-day D/H ratio in the interstellar medium.

For fixed $g_3, \alpha, y_3^\odot, y_2^{ism}$, and $y_2^\odot = y_{23}^\odot - y_3^\odot$, I assume a flat p.d.f. for y_2^{obs}, y_3^{obs} , subject to the constraints (5.13), (5.14), and (5.15). I weight these flat p.d.f.'s by a top-hat p.d.f. for g_3 (see Eq. (5.11)) and by Gaussian p.d.f.'s for $y_{23}^\odot, y_3^\odot, y_2^{ism}$, and α , where the means and standard deviations of these quantities are given in Eqs. (5.3), (5.4), (5.5), and (5.8). This gives me the p.d.f. for y_2^{obs}, y_3^{obs} .

My confidence level is now calculated for *four* degrees of freedom a_i , rather than the three degrees of freedom in Ch. 4, because of the inclusion of ^3He . Again, the abundances a_i^{th} are highly non-linear functions of the theory parameters $\mathbf{p} = (\tau_X, m_X Y_X, \eta)$, so it does not make sense to integrate out a theory parameter to reduce the number of degrees of freedom. Instead, I shall present my results using the same projection procedure as in the previous chapter.

5.3 Results

The proto-solar measurements of D and ^3He favor high η . Therefore, SBBN works well in the case of high ^4He , but not in the case of low SBBN. In the former case, I can place upper bounds on my model parameters, while in the latter, I investigate whether a non-standard scenario of BBN can work significantly better than SBBN.

5.3.1 Low ^4He ($Y^{obs} = 0.234 \pm (0.002)_{stat} \pm (0.005)_{syst}$)

Fig. 5.1 shows the 95% C.L. contour computed using four elements (D, ^3He ,

^4He , and ^7Li). The contour is shown in the $m_X Y_X$ vs. τ_X plane for several representative baryon-to-photon ratios ($\eta = 2 \times 10^{-10}, 4 \times 10^{-10}, 5 \times 10^{-10}, 6 \times 10^{-10}$). The disjoint regions in Fig. 5.1a are an artifact of the low resolution of the plot; the true allowed region is a single, long, thin strip. Note that for $\eta = 6 \times 10^{-10}$, no region is allowed at the 95% C.L. Moreover, no region is allowed at the 68% C.L. for any η . As in Ch. 4, the allowed region is consistent with the constraints from $^6\text{Li}/^7\text{Li}$.

Since the proto-solar data favor high η , as indicated by the gray lines in Fig. 1.2, this case is similar to that of the low QAS data (*c.f.* Fig. 4.1). In both cases, the most favored region of parameter space is at $\tau_X \lesssim 10^6$ sec, $m_X Y_X \gtrsim 10^{-10}$ GeV, and $\eta = 2$ to 4×10^{-10} (see Fig. 5.1a).

Another way to see the allowed region is in the $m_X Y_X$ vs. η plane at fixed τ_X , as in Fig. 5.2. The SBBN allowed range of η is shown at small $m_X Y_X$. In the proto-solar case, lower η is allowed than in the low QAS case (*c.f.* Fig. 4.2), because the uncertainty in D/H is larger. At larger $m_X Y_X$, a lower η is allowed (which produces more D and ^3He), because high-energy photons photodissociate D and ^3He . However, the upper bound on $^3\text{He}/\text{H}$ excludes $\eta \lesssim 2 \times 10^{-10}$. At still larger $m_X Y_X$, all elements are overly photodissociated.

Fig. 5.3 shows the edge of the projection of the 95% C.L. region into the $m_X Y_X$ vs. τ_X plane. As in Ch. 4, I project by taking the lowest C.L. value as I vary η for each $(\tau_X, m_X Y_X)$. In Table 5.1, I show representative values of $m_X Y_X$ that correspond to the 95% C.L. upper bound for $\tau_X = 10^4 - 10^9$ sec.

$\tau_X =$	10^4 sec	10^5 sec	10^6 sec	10^7 sec	10^8 sec	10^9 sec
95% C.L.	3×10^{-5}	1×10^{-8}	6×10^{-10}	2×10^{-13}	3×10^{-14}	$< 1 \times 10^{-14}$

Table 5.1: Upper bound on $m_X Y_X$ in units of GeV for the case of low value of ${}^4\text{He}$, and proto-solar $(\text{D}+{}^3\text{He})/\text{H}$ and ${}^3\text{He}/\text{H}$. Note that the C.L. is for four degrees of freedom, and η is varied to give the maximum values for $m_X Y_X$.

There are two main differences between the proto-solar and low QAS cases. First, because of their low binding energies, D and ${}^3\text{He}$ together yield a stronger constraint at high τ_X than D alone, and they exclude the “finger” in Fig. 4.3 at $\tau_X \sim 3 \times 10^6$ sec and $m_X Y_X \sim 10^{-10}$ GeV. Second, the four elements in the proto-solar case provide a stronger constraint than the three elements in the QAS case, so that no region is allowed at the 68% C.L. Thus, a radiatively decaying particle does not provide a very good solution to the “crisis” of Hata *et al.* [84].

5.3.2 High ${}^4\text{He}$ ($Y^{obs} = 0.244 \pm (0.002)_{stat} \pm (0.005)_{sys}$)

High observed ${}^4\text{He}$ favors high η , so it is consistent with the proto-solar $(\text{D}+{}^3\text{He})/\text{H}$ and ${}^3\text{He}/\text{H}$ in SBBN (see Fig. 1.2). This case is similar to that of high ${}^4\text{He}$ and low QAS D/H. Thus, I shall constrain my model parameters in this case.

In Fig. 5.4, I show the 68% and 95% C.L. contours at (a) $\eta = 2 \times 10^{-10}$, (b) $\eta = 4 \times 10^{-10}$, (c) $\eta = 5 \times 10^{-10}$, and (d) $\eta = 6 \times 10^{-10}$. Note that again, my constraints are consistent with the shaded upper bounds from ${}^6\text{Li}/{}^7\text{Li}$.

I predicted that this case would be similar to that of high ${}^4\text{He}$ and low QAS D/H; however, Fig. 5.4 appears rather different from Fig. 4.8, especially panels

$\tau_X =$	10^4 sec	10^5 sec	10^6 sec	10^7 sec	10^8 sec	10^9 sec
95% C.L.	3×10^{-5}	6×10^{-9}	6×10^{-10}	1×10^{-12}	1×10^{-13}	$< 1 \times 10^{-14}$
68% C.L.	1×10^{-5}	3×10^{-9}	3×10^{-10}	3×10^{-13}	3×10^{-14}	$< 1 \times 10^{-14}$

Table 5.2: Same as Table 5.1, except for high ${}^4\text{He}$.

(b) and (d). The proto-solar case is more easily compared to the QAS case at constant τ_X , as in Fig. 5.5. Comparing this to Fig. 4.9, one can see that in SBBN (low $m_X Y_X$), both cases favor $\eta \sim 5 \times 10^{-10}$, although the proto-solar case allows a much wider range of η . This is because the low QAS D/H value has extremely small error bars. The other main difference between the two cases is that low η is not allowed by the proto-solar data, even for the non-standard regions ($m_X Y_X \gtrsim 10^{-10}$ GeV). This is because of the upper bound on ${}^3\text{He}/\text{H}$ (see the gray lines in Fig. 1.2).

Fig. 5.6 shows the C.L. contours projected along the η axis into the $m_X Y_X$ vs. τ_X plane. Note that the combination of $(\text{D}+{}^3\text{He})/\text{H}$ and ${}^3\text{He}/\text{H}$ provides a strong bound at long lifetimes and forbids a “finger” near the center of the plot (*c.f.* Fig. 4.10). Table 5.2 gives the 68% and 95% C.L. upper bounds on $m_X Y_X$ for various of τ_X .

As I discussed in Section 4.3, the blackbody spectrum of the cosmic microwave background radiation imposes an additional constraint on X , for lifetimes τ_X longer than 10^6 sec (see Eqn (4.8)). However, the CMBR constraint is not as strong as the limits set by the combination of $(\text{D}+{}^3\text{He})/\text{H}$ and ${}^3\text{He}/\text{H}$ for both high and low ${}^4\text{He}$. Hadronic decays of X would lead to stricter constraints on the

model parameters $m_X Y_X$, τ_X , and η , because hadronic showers lead to efficient production of the light elements.

Figure 5.1: 95% C.L. in the $m_X Y_X$ vs. τ_X plane, for low value of ${}^4\text{He}$, and proto-solar $(\text{D}+{}^3\text{He})/\text{H}$ and ${}^3\text{He}/\text{H}$. The allowed regions lie (a) inside the contours, and (b,c) below and to the left of the contours. I take (a) $\eta = 2 \times 10^{-10}$, (b) $\eta = 4 \times 10^{-10}$, (c) $\eta = 5 \times 10^{-10}$, and (d) $\eta = 6 \times 10^{-10}$. The shaded regions are $y_6/y_7 \gtrsim 0.5$, and the darker shaded regions are $y_6/y_7 \gtrsim 1.3$.

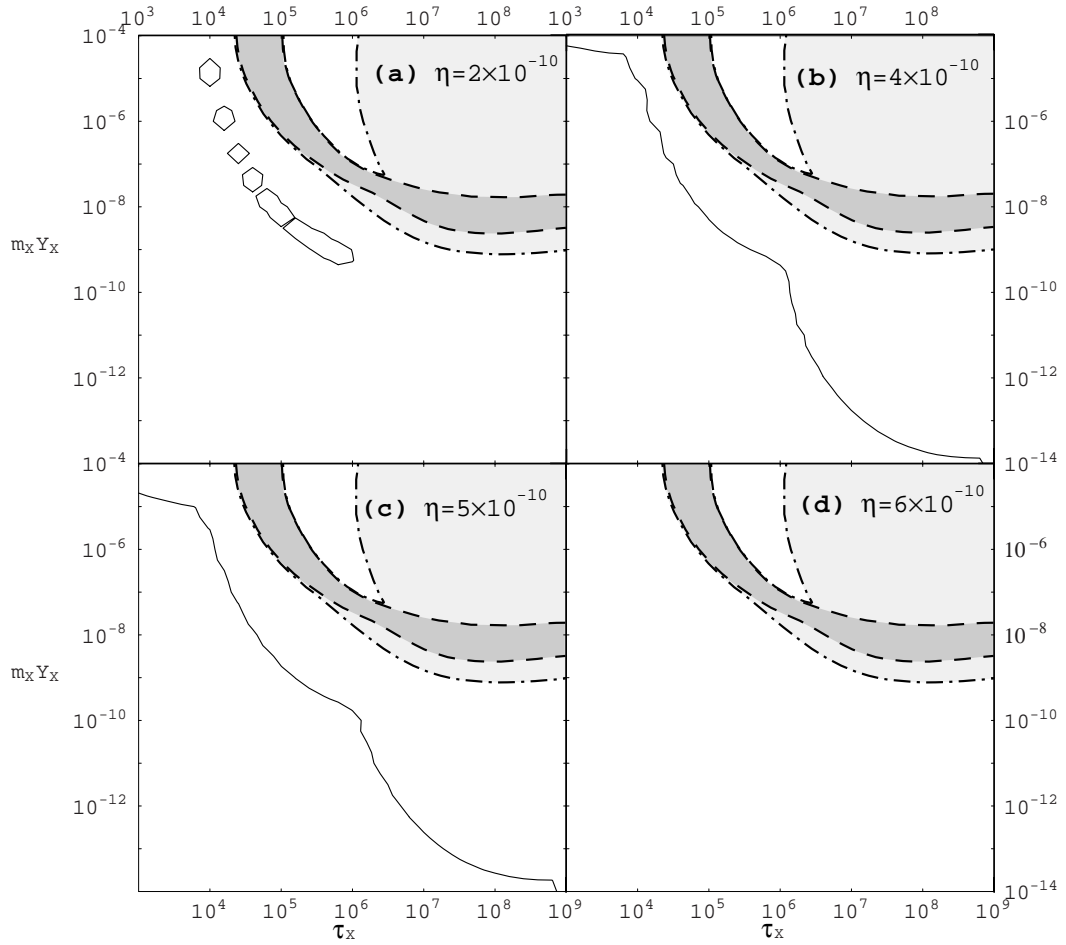


Figure 5.2: 95% C.L. in the $m_X Y_X$ vs. η plane for various values of τ_X , for low value of ${}^4\text{He}$, and proto-solar $(\text{D}+{}^3\text{He})/\text{H}$ and ${}^3\text{He}/\text{H}$. The allowed regions lie within the contours.

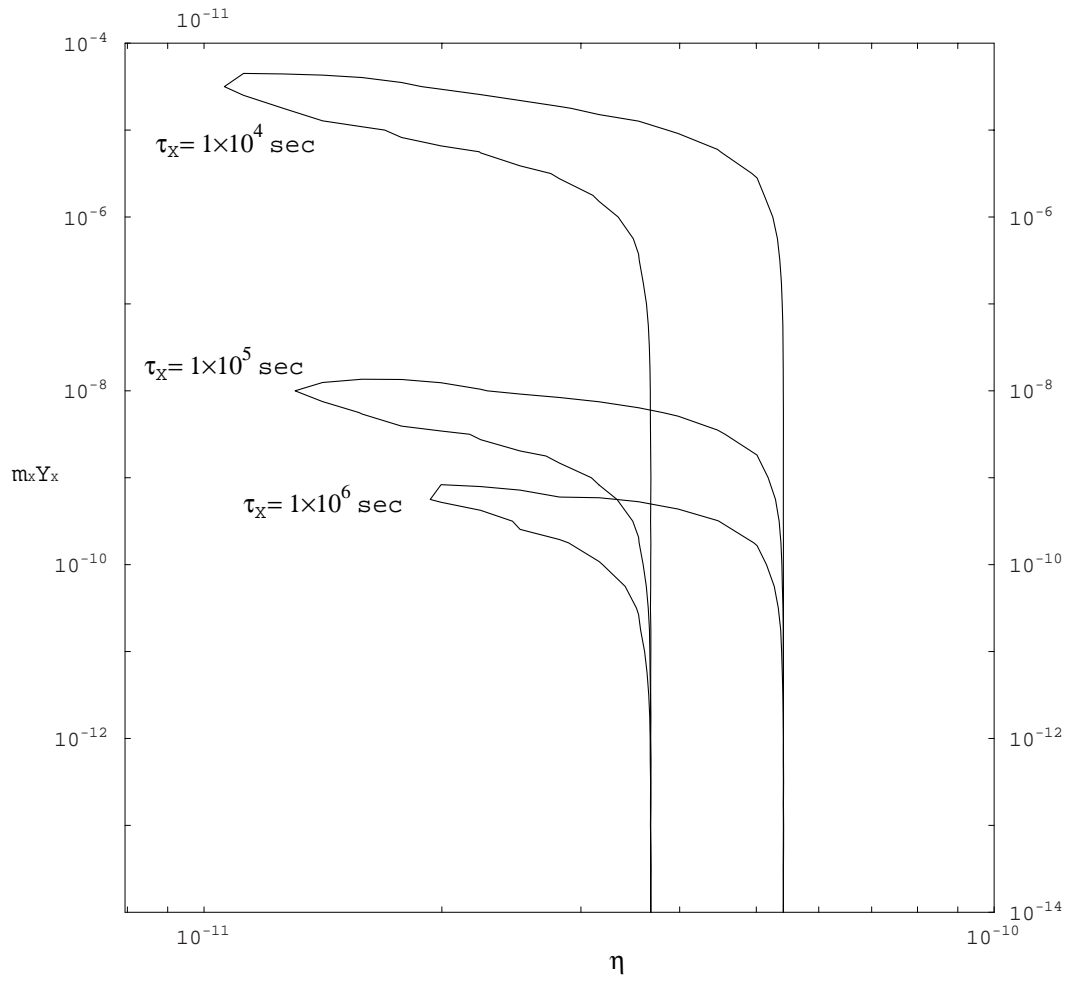


Figure 5.3: 95% C.L. contour projected along the η axis, for low value of ${}^4\text{He}$, and proto-solar $(\text{D}+{}^3\text{He})/\text{H}$ and ${}^3\text{He}/\text{H}$. The allowed region lies below and to the left of the contour.

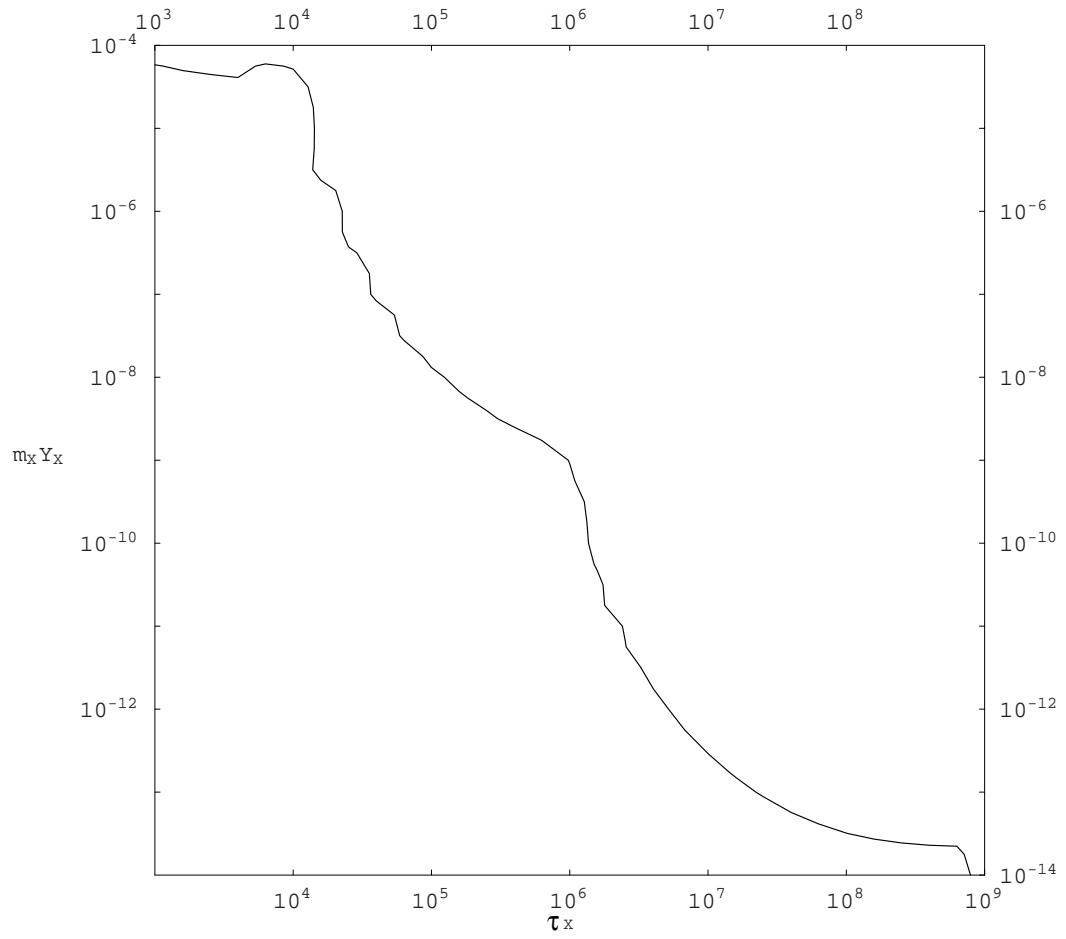


Figure 5.4: Same as Fig. 5.1, except for high value of ${}^4\text{He}$. The solid line is the 95% C.L.; the dotted line is the 68% C.L.

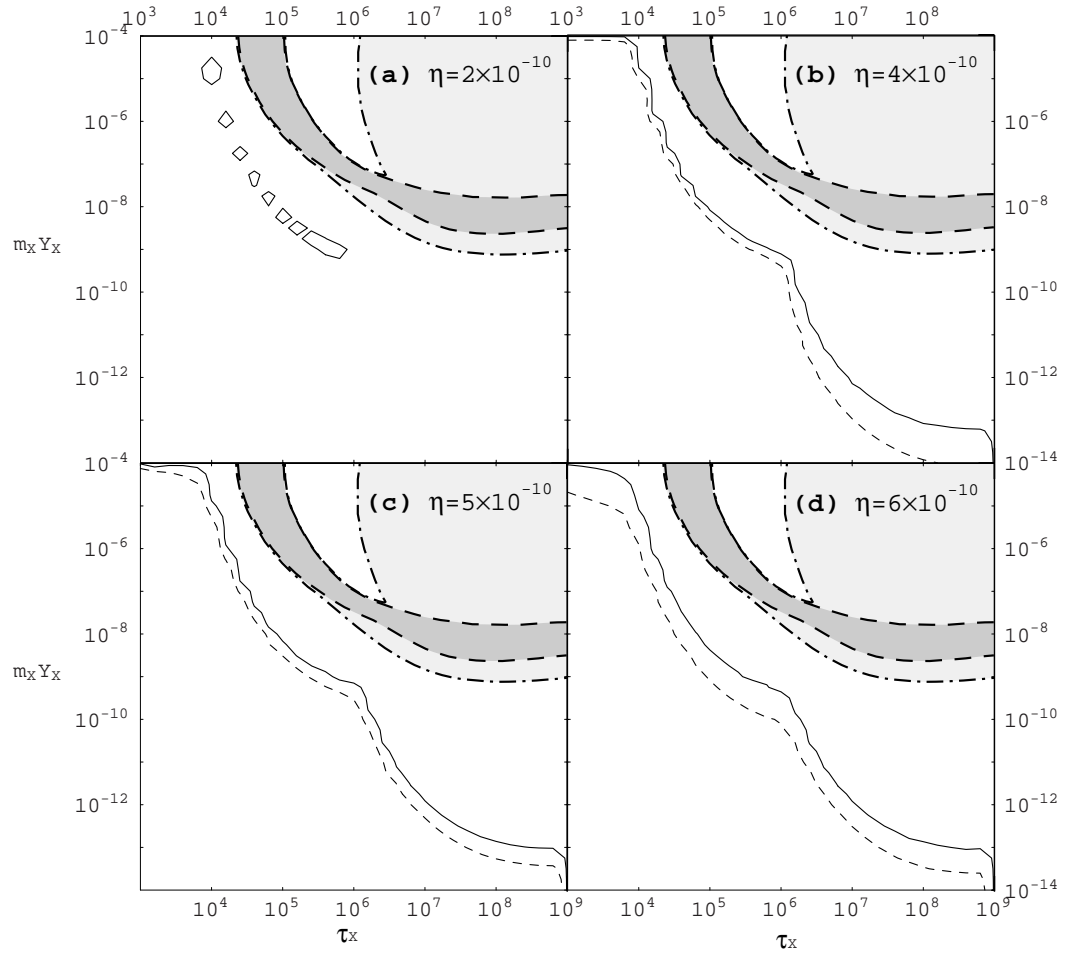


Figure 5.5: Same as Fig. 5.2, except for high value of ${}^4\text{He}$. The solid line is the 95% C.L.; the dotted line is the 68% C.L.

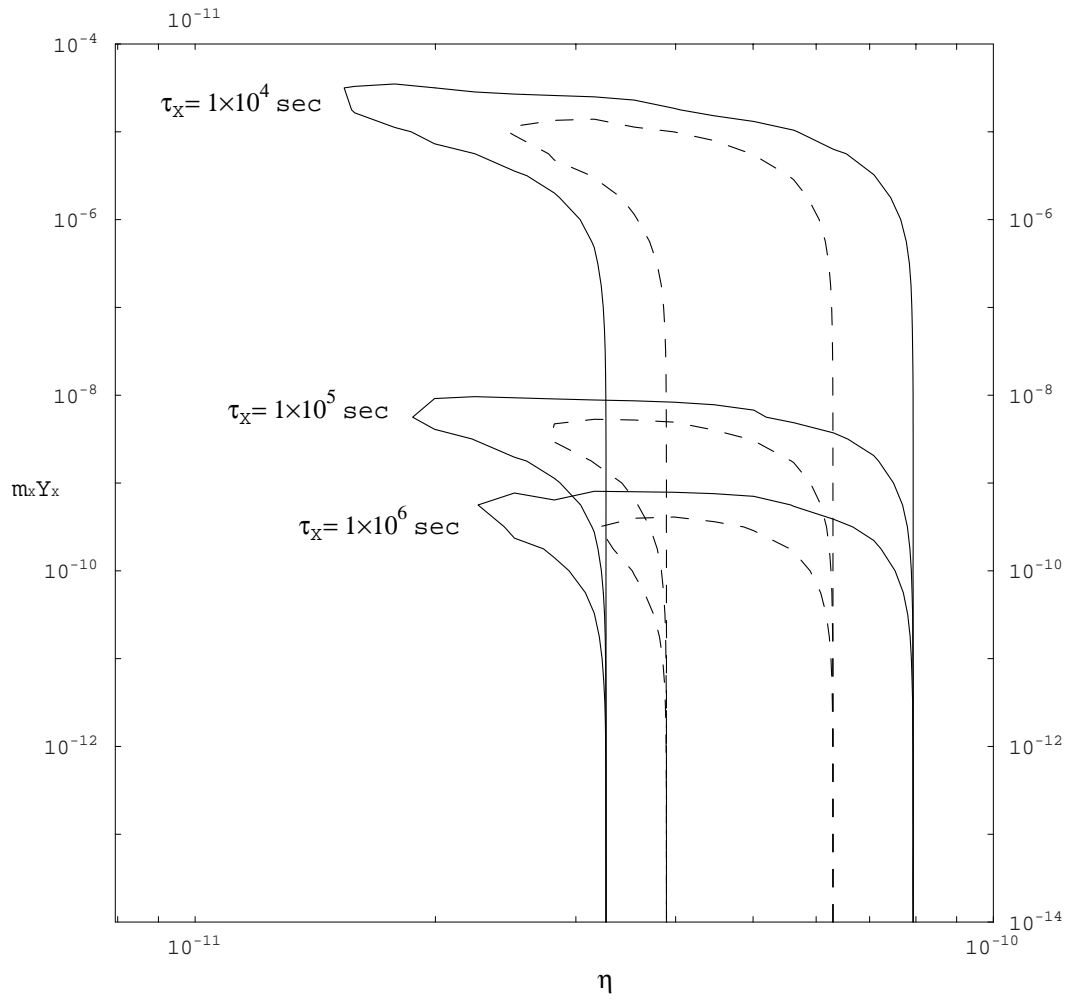
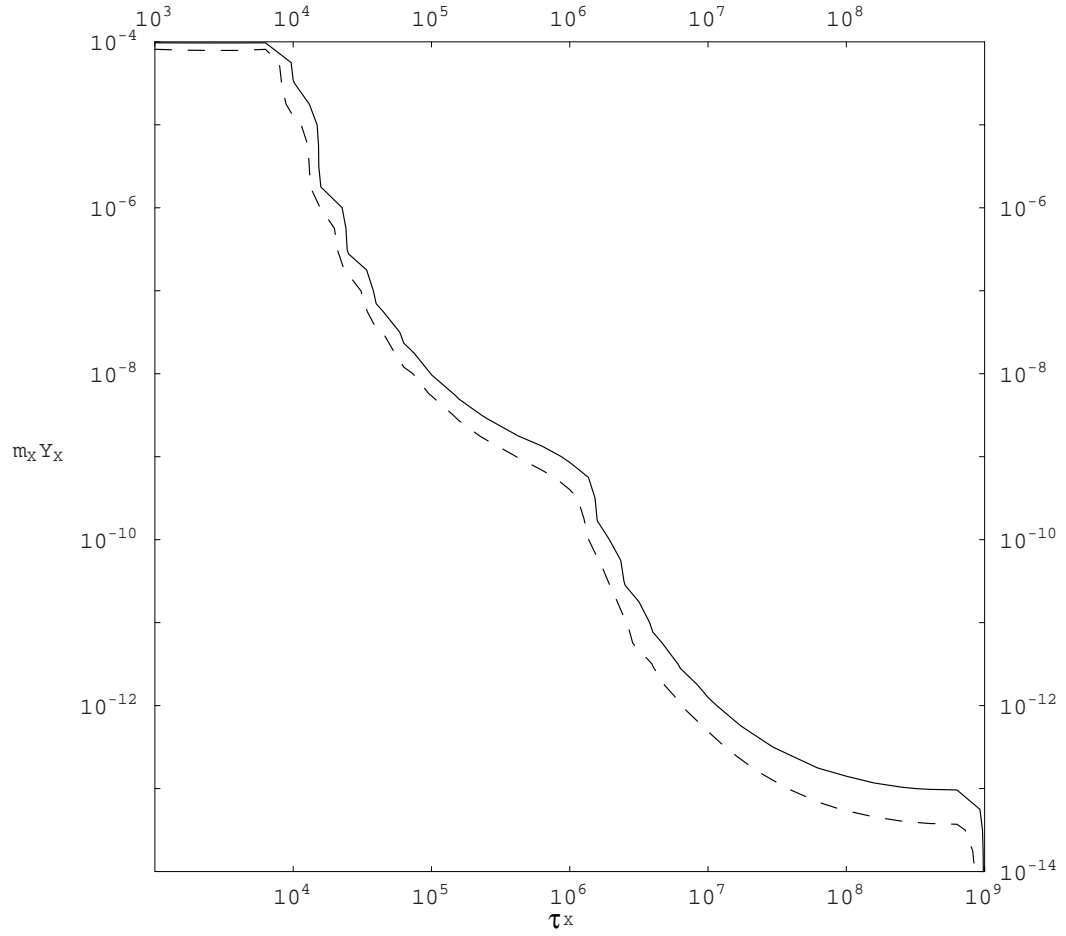


Figure 5.6: Same as Fig. 5.3, except for high value of ${}^4\text{He}$. The solid line is the 95% C.L.; the dotted line is the 68% C.L.



Chapter 6

Models

So far, I have discussed general constraints from BBN on radiatively decaying particles. In the minimal standard model, there is no such particle. However, some extensions of the standard model naturally result in such exotic particles, and the light-element abundances may be affected significantly in these cases. In this section, I present several examples of such radiatively decaying particles, and discuss the constraints.

In particular, I will consider particles in supergravity models [86]. Global supersymmetry (SUSY), a symmetry between fermions and bosons, is attractive because it can solve the gauge hierarchy problem (*viz.*, how the electroweak scale can be so much smaller than the Planck scale, despite renormalization). Supersymmetry solves this problem because positive contributions from bosonic loop integrals are precisely canceled by negative contributions from the corresponding fermionic loop integrals. When SUSY is gauged, it automatically includes gravity; hence, local supersymmetry is known as “supergravity.”

6.1 Gravitino

My first example of a long-lived particle is the gravitino ψ , which appears in

all the supergravity models. The gravitino is the superpartner of the graviton, and its interactions are suppressed by inverse powers of the reduced Planck scale $M_* \simeq 2.4 \times 10^{18}$ GeV [87]. Because of this suppression, the lifetime of the gravitino is very long. Assuming that the gravitino's dominant decay mode is to a photon and its superpartner (the photino), the gravitino's lifetime is given by

$$\tau_{3/2} \simeq \frac{8\pi M_*^2}{m_{3/2}^3} \simeq 4 \times 10^5 \text{ sec} \times (m_{3/2}/1 \text{ TeV})^{-3}, \quad (6.1)$$

where $m_{3/2}$ is the gravitino mass. Notice that the gravitino mass is $O(100 \text{ GeV} - 1 \text{ TeV})$ in models in which SUSY breaking is communicated by gravity from a hidden sector to the SUSY sector. Such a mass for the gravitino results in a lifetime that may affect the primordial light-element abundances.

If the gravitino is in thermal equilibrium in the early universe, then its energy density is of order T^4 , as given in Eq. (1.16). If the gravitino is not diluted, then it matter-dominates the universe when the temperature falls below $m_{3/2}$. This completely spoils the (near) success of BBN theory. Usually, this problem is solved by introducing inflation, which dilutes away the primordial gravitinos. After reheating at the end of inflation, a smaller number of gravitinos are produced through the scattering processes of thermal particles. The abundance $Y_{3/2} = n_{3/2}/n_\gamma$ of gravitinos depends on the reheating temperature T_R , and is given by [8]

$$Y_{3/2} \simeq 3 \times 10^{-11} \times (T_R/10^{10} \text{ GeV}). \quad (6.2)$$

Therefore, if the reheating temperature is too high, then gravitinos are overproduced, and too many light nuclei are photodissociated when the gravitinos decay.

My constraints on $(\tau_X, m_X Y_X)$ from Chapters 4 and 5 can be transformed into constraints on $(m_{3/2}, T_R)$. In Figures 6.1 and 6.2, I show the transformations of the projected 95% C.L. boundaries from Figs. 4.3, 4.7, 4.10, 4.13, 5.3, and 5.6. The proto-solar data yield tighter constraints on T_R for all $m_{3/2}$ than the QAS data, particularly at low $m_{3/2}$ (long lifetimes). For several values of the gravitino mass, I quote the most conservative (*i.e.*, weakest) upper bound on the reheating temperature from Figs. 6.1 and 6.2:

$$\begin{aligned} m_{3/2} = 100 \text{ GeV} \quad (\tau_{3/2} \simeq 4 \times 10^8 \text{ sec}) & : T_R \lesssim 3 \times 10^8 \text{ GeV}, \\ m_{3/2} = 1 \text{ TeV} \quad (\tau_{3/2} \simeq 4 \times 10^5 \text{ sec}) & : T_R \lesssim 1 \times 10^9 \text{ GeV}, \\ m_{3/2} = 3 \text{ TeV} \quad (\tau_{3/2} \simeq 1 \times 10^4 \text{ sec}) & : T_R \lesssim 3 \times 10^{11} \text{ GeV}. \end{aligned}$$

If the gravitino is heavy enough ($m_{3/2} \gtrsim 5 \text{ TeV}$), then its lifetime is too short to destroy even D. In this case, my only constraint is from the overproduction of ${}^4\text{He}$. If the gravitino mass is lighter, then the lifetime is long enough to destroy D or even ${}^4\text{He}$. In this case, my constraint on the reheating temperature is more severe.

6.2 Bino

Another example of my decaying particle is the lightest superparticle in the minimal supersymmetric standard model (MSSM) sector¹, if it is heavier than the gravitino. In many theories, the lightest superparticle is the “neutralino”—a

¹The MSSM consists of the standard model particles, their superpartners, two Higgs bosons, and their superpartners.

linear combination of the superpartners of the photon, Z boson, and Higgs bosons. In these theories, the lightest neutralino can decay into a high-energy photon and a gravitino. Thus, I may use BBN to constrain the MSSM.

The abundance (1.20) of the lightest neutralino is determined by the temperature T_F at which it freezes out of the thermal bath. In a theory with heavier sfermions², the neutralino (mass m) has a smaller annihilation cross section σ , so it freezes out at a higher temperature (when the annihilation rate falls below the expansion rate: $\sigma(mT_F)^{3/2} \exp(-m/T_F) \sim \Gamma \lesssim H \sim T_F^2/M_*$), with a higher thermal abundance. Thus, the upper bound on $m_X Y_X$ can be translated into an upper bound on the mass scale of the sfermions.

In order to investigate this scenario, I consider the simplest case where the lightest neutralino is (almost) purely bino \tilde{B} (the superpartner of the $U(1)$ gauge boson B). In this case, the lightest neutralino pair-annihilates through squark and slepton exchange. In particular, if the right-handed sleptons are the lightest sfermions, then the dominant annihilation is $\tilde{B} + \tilde{B} \rightarrow l^+ + l^-$. The annihilation cross section of this process is given by [88]

$$\langle \sigma v_{\text{rel}} \rangle = 8\pi\alpha_1^2 \langle v^2 \rangle \left\{ \frac{m_{\tilde{B}}^2}{(m_{\tilde{B}}^2 + m_{l_R}^2)^2} - \frac{2m_{\tilde{B}}^4}{(m_{\tilde{B}}^2 + m_{l_R}^2)^3} + \frac{2m_{\tilde{B}}^6}{(m_{\tilde{B}}^2 + m_{l_R}^2)^4} \right\}, \quad (6.3)$$

where $\langle v^2 \rangle$ is the thermal average of the square of the velocity of the bino, and I have added the contributions from all three generations by assuming that the

²Squarks, sleptons, and sfermions are the respective superpartners of the quarks, leptons, and standard model fermions.

right-handed sleptons are degenerate.³ With this annihilation cross section, the Boltzmann equation for the number density of binos is given by

$$\dot{n}_{\tilde{B}} + 3Hn_{\tilde{B}} = -2\langle\sigma v_{\text{rel}}\rangle(n_{\tilde{B}}^2 - (n_{\tilde{B}}^{\text{EQ}})^2), \quad (6.4)$$

where $n_{\tilde{B}}^{\text{EQ}}$ is the equilibrium number density of binos. The factor 2 is present because two binos annihilate into leptons in each interaction. I solved this equation and obtained the mass density of the bino as a function of the bino mass and the right-handed slepton mass. (For details, see *e.g.*, Ref. [14]). Numerically, for $m_{\tilde{B}} = 100$ GeV, $m_X Y_X$ ranges from $\sim 10^{-9}$ GeV to $\sim 10^{-5}$ GeV as I vary $m_{\tilde{l}_R}$ from 100 GeV to 1 TeV. If $m_X Y_X$ is in this range, the primordial light-element abundances are affected significantly, unless the lifetime of the bino is shorter than $10^4 - 10^5$ sec (see Figs. 2.2 – 2.6). The lifetime of the bino is given by

$$\tau_{\tilde{B}} = \left[\frac{1}{48\pi} \frac{m_{\tilde{B}}^5 \cos^2 \theta_W}{m_{3/2}^2 M_*^2} \right]^{-1} \simeq 7 \times 10^4 \text{ sec} \times \left(\frac{m_{\tilde{B}}}{100 \text{ GeV}} \right)^{-5} \left(\frac{m_{3/2}}{1 \text{ GeV}} \right)^2. \quad (6.5)$$

Notice that the lifetime becomes shorter as the gravitino mass decreases; hence, too much D and ^7Li are destroyed if the gravitino mass is too large. The constraints given in Figs. 4.3, 4.7, 4.10, 4.13, 5.3, and 5.6 therefore become upper bounds on the gravitino mass. Since the abundance of the bino is an increasing function of the slepton mass $m_{\tilde{l}_R}$, the upper bound on the gravitino mass is more severe for larger slepton masses. For example, for $m_{\tilde{B}} = 100$ GeV, the upper bounds on the gravitino mass are shown in Fig. 6.3 and Fig. 6.4. For all values of the

³If the bino is heavier than the top quark, then the *s*-wave contribution annihilating into top quarks becomes important. In this work, I do not consider this case.

slepton mass, the QAS data give a much stronger constraint than the proto-solar data. For some representative values of the slepton mass, the most conservative constraints are:

$$m_{\tilde{l}_R} = 100 \text{ GeV} \quad : \quad m_{3/2} \lesssim 4 \text{ GeV},$$

$$m_{\tilde{l}_R} = 300 \text{ GeV} \quad : \quad m_{3/2} \lesssim 2 \text{ GeV},$$

$$m_{\tilde{l}_R} = 1 \text{ TeV} \quad : \quad m_{3/2} \lesssim 700 \text{ MeV}.$$

As expected, for a larger value of the slepton mass, the primordial abundance of the bino gets larger, and the upper bound on the gravitino mass becomes smaller.

6.3 Modulus

Another interesting source of high-energy photons is a modulus field ϕ . Moduli are massless scalars that arise in string-inspired supergravity theories due the compactification of extra spatial dimensions. A modulus field acquires mass from SUSY breaking. In many models, the modulus mass m_ϕ is of the same order as the gravitino mass (see for example [89]); with such a mass, the modulus is a candidate for my long-lived, massive X particle.

The equation of motion of a modulus with a simple quadratic potential in an expanding universe follows from conservation of energy-stress $T^\mu{}_{\nu;\mu} = 0$ [14]:

$$\ddot{\phi} + 3H\dot{\phi} + \Gamma_\phi\dot{\phi} + m_\phi^2\phi = 0 \tag{6.6}$$

In the early universe, the mass of the modulus field is negligible compared to the expansion rate of the universe. Thus, the modulus field is a strongly-overdamped

harmonic oscillator, so the modulus amplitude may sit far from the minimum of its potential. Since the only scale parameter in supergravity is the Planck scale M_* , the initial amplitude ϕ_0 is naively expected to be of $O(M_*)$. However, this initial amplitude is too large; the modulus would matter-dominate the universe, and photons from its decay would distort the spectrum of the cosmic microwave background radiation. In this model, I regard ϕ_0 as a free parameter on which I can set an upper bound.

Once the expansion rate becomes smaller than the mass of the modulus field, the modulus field begins to oscillate. Assuming homogeneity, the energy density and pressure are

$$\rho_\phi = \frac{1}{2}\dot{\phi}^2 + \frac{m^2}{2}\phi^2 \quad (6.7)$$

$$p_\phi = \frac{1}{2}\dot{\phi}^2 - \frac{m^2}{2}\phi^2 \quad (6.8)$$

The average of the pressure over a period is zero; the average of the energy density is $\langle\dot{\phi}^2\rangle$, so the averaged energy density evolves as

$$\dot{\rho}_\phi + 3H\rho_\phi + \Gamma_\phi\rho_\phi = 0. \quad (6.9)$$

Therefore, ρ_ϕ red-shifts as a^{-3} (where a is the scale factor), and the oscillating modulus behaves as non-relativistic matter. The modulus eventually decays when the expansion rate becomes comparable to its decay rate

$$\Gamma_\phi = \frac{1}{\tau_\phi} \simeq \frac{m_{3/2}^3}{8\pi M_*^2} \simeq \frac{1}{4 \times 10^5 \text{ sec}} \times \left(\frac{m_{3/2}}{1 \text{ TeV}}\right)^3. \quad (6.10)$$

Without entropy production from another source, the modulus density at the

decay time is approximately

$$m_\phi Y_\phi = \frac{\rho_\phi}{n_\gamma} \sim 5 \times 10^{10} \text{ GeV} \times (m_\phi/1 \text{ TeV})^{1/2} (\phi_0/M_*)^2. \quad (6.11)$$

As in my other models, I can convert my constraints on $(\tau_X, m_X Y_X)$ (Figs. 4.3, 4.7, 4.10, 4.13, 5.3, and 5.6) into constraints on (m_ϕ, ϕ_0) . For small $m_{3/2}$ (long lifetimes), the proto-solar data give a tighter constraint, because too much ^3He is dissociated. But for higher masses, the QAS data give a slightly stronger constraint. Using the most conservative of these 95% C.L. constraints from Figs. 6.5 and Figs. 6.6, I still obtain very stringent bounds on the initial amplitude of the modulus field ϕ_0 :

$$m_\phi = 100 \text{ GeV} \quad (\tau_\phi \sim 4 \times 10^8 \text{ sec}) \quad : \quad \phi_0 \lesssim 1 \times 10^8 \text{ GeV},$$

$$m_\phi = 1 \text{ TeV} \quad (\tau_\phi \sim 4 \times 10^5 \text{ sec}) \quad : \quad \phi_0 \lesssim 5 \times 10^8 \text{ GeV},$$

$$m_\phi = 3 \text{ TeV} \quad (\tau_\phi \sim 1 \times 10^4 \text{ sec}) \quad : \quad \phi_0 \lesssim 2 \times 10^{10} \text{ GeV}.$$

Clearly, my upper bound from BBN rules out the naive expectation that $\phi_0 \sim M_*$. It is important to notice that (conventional) inflation cannot solve this difficulty by diluting the coherent mode of the modulus field. This is because the expansion rate of the universe is usually much larger than the mass of the modulus field, so the modulus field has not yet begun to oscillate. Thus, the modulus has constant amplitude and energy density throughout an early inflationary epoch. One attractive solution is a thermal inflation model proposed by Lyth and Stewart [90]. In the thermal inflation model, a late mini-inflation of about 10 e -folds reduces the modulus density. Even if thermal inflation occurs, there may remain a significant

modulus energy density that decays to high-energy photons. Thus, BBN gives a stringent constraint on the thermal inflation model.

Figure 6.1: Contours of 95% C.L., yielding an upper bound on the reheating temperature, as a function of the gravitino mass. QAS data are used for the observed D/H ratio.

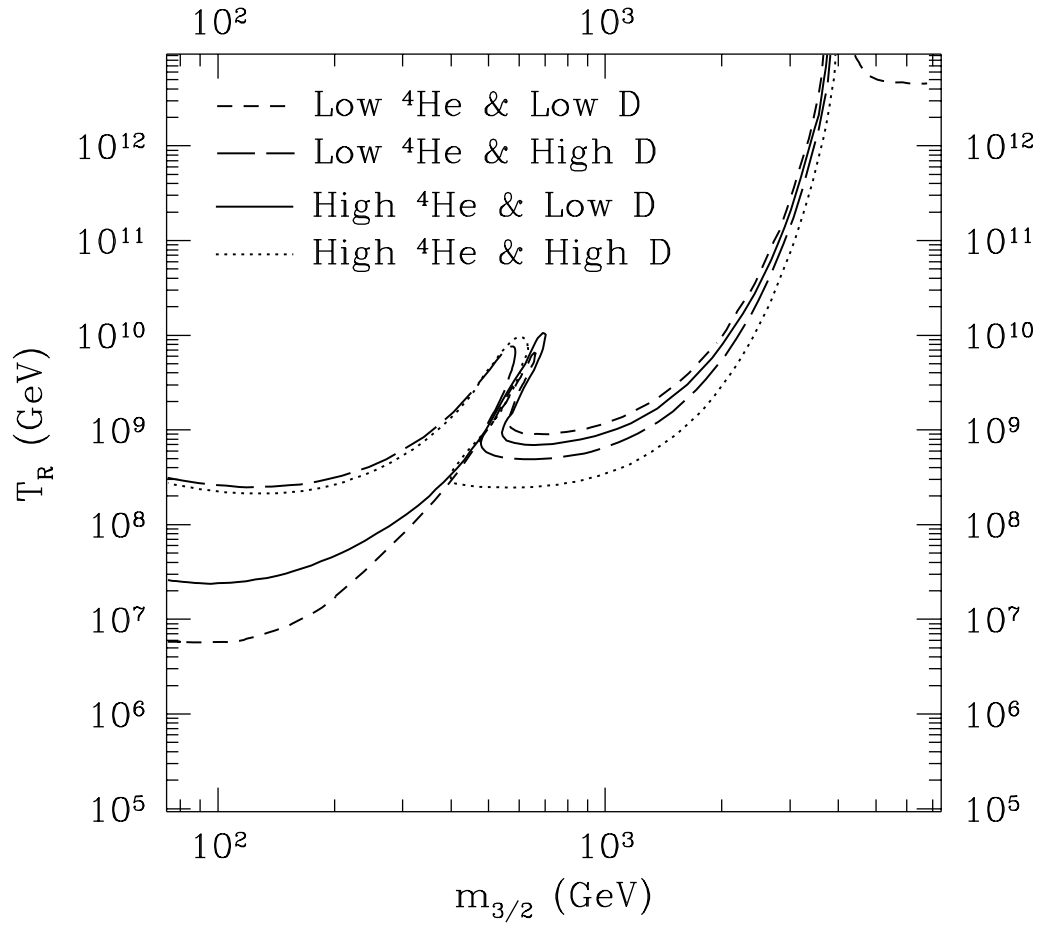


Figure 6.2: Contours of 95% C.L., yielding an upper bound on the reheating temperature, as a function of the gravitino mass. Proto-solar data are used for the observed D/H and (D+³He)/H ratios.

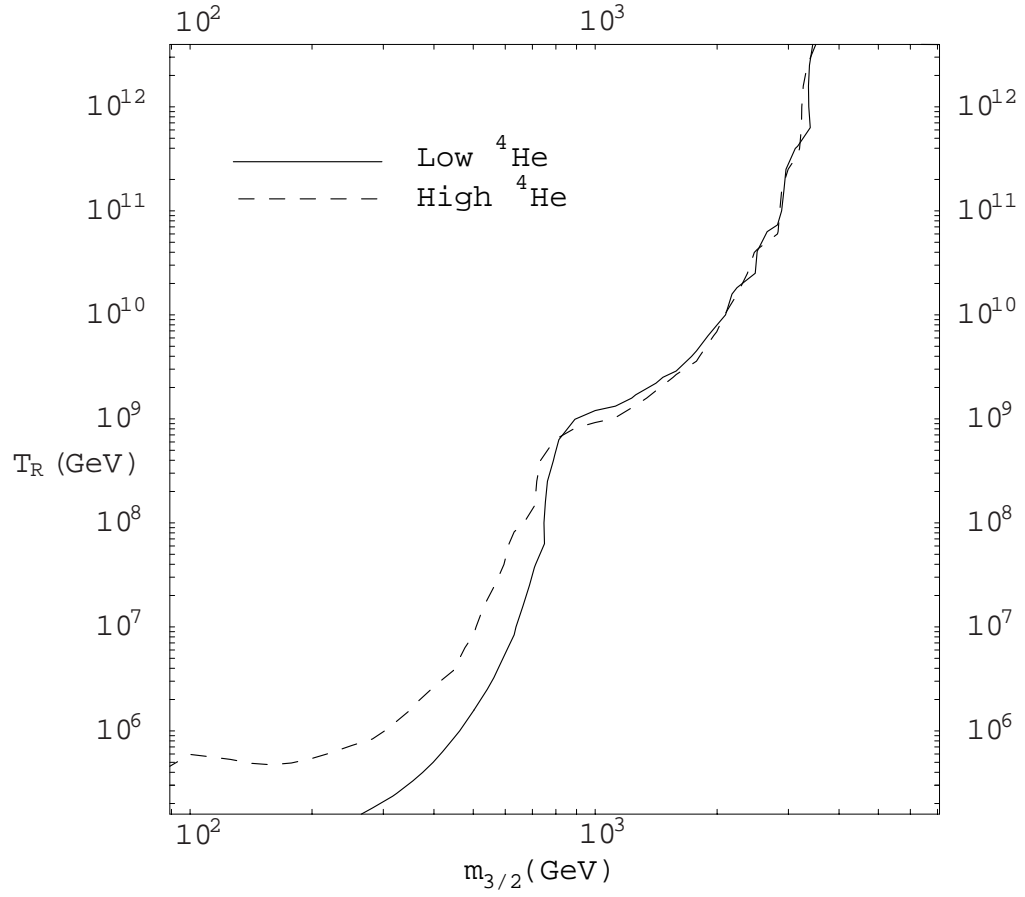


Figure 6.3: Contours of 95% C.L., yielding an upper bound on the gravitino mass, as a function of the right-handed slepton mass. QAS data are used for the observed D/H ratio.

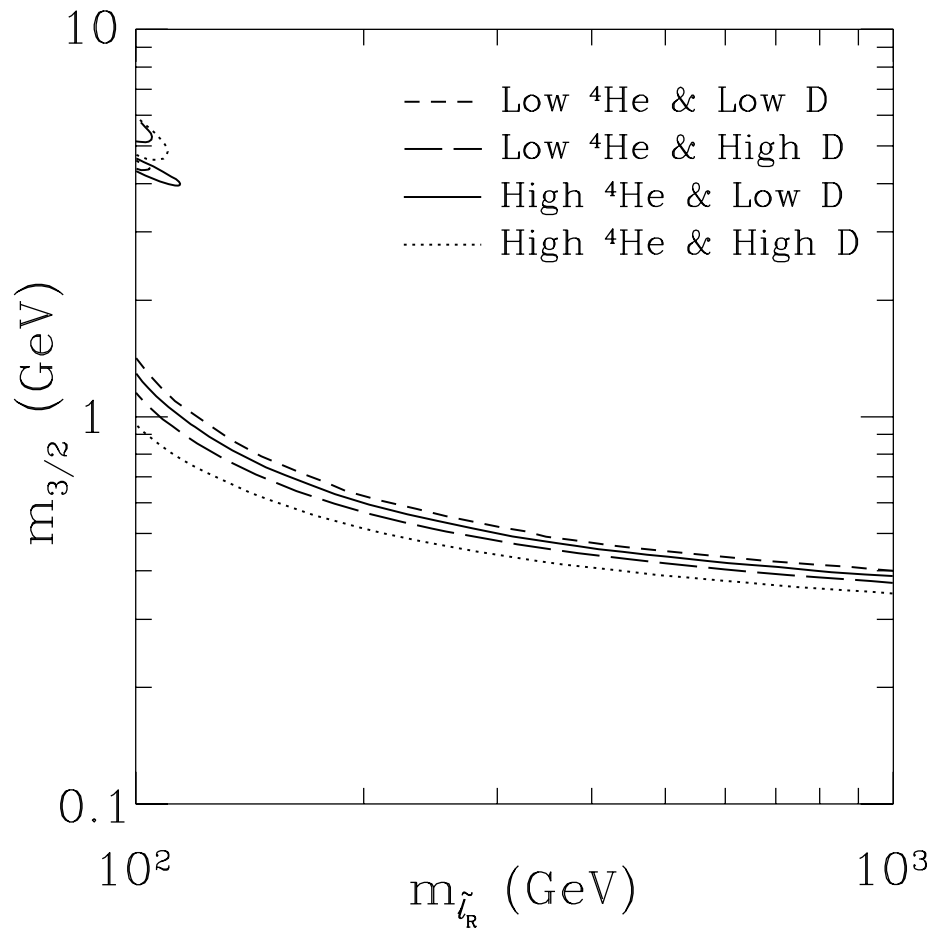


Figure 6.4: Contours of 95% C.L., yielding an upper bound on the gravitino mass, as a function of the right-handed slepton mass. Proto-solar data are used for the observed D/H and (D+³He)/H ratios.

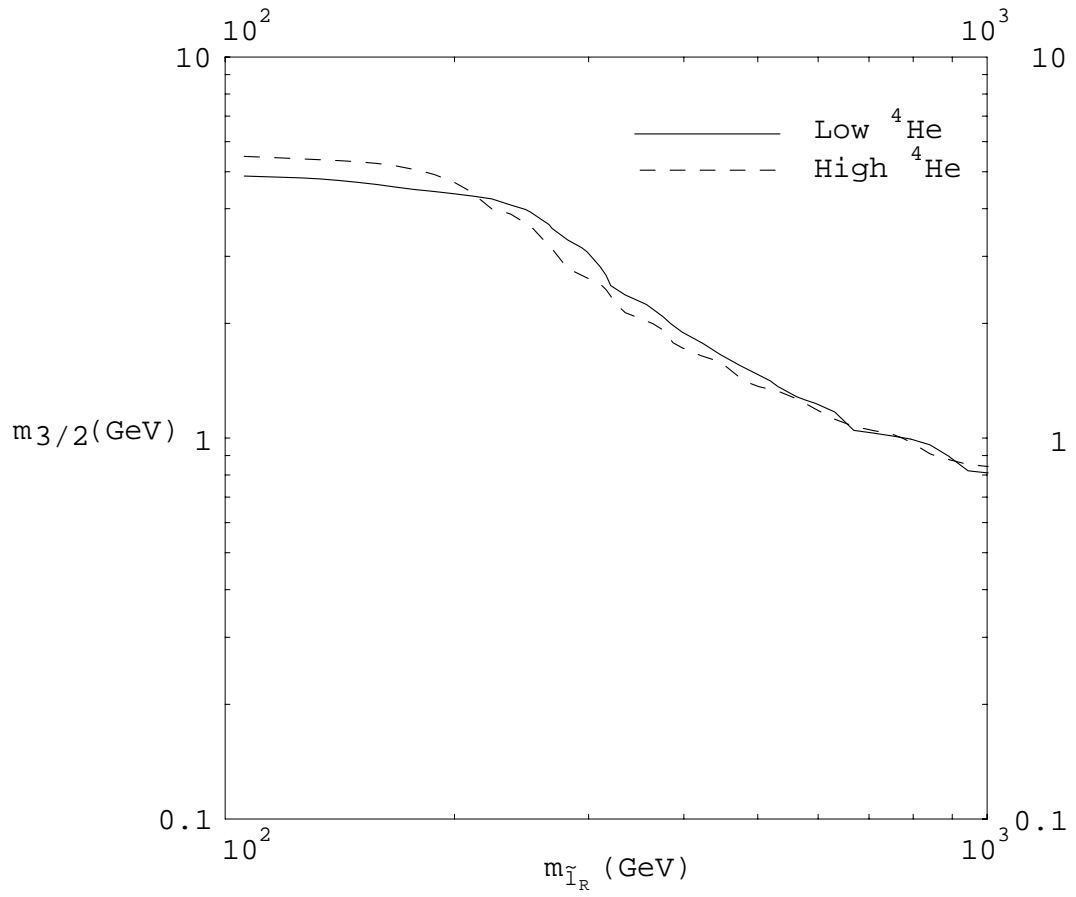


Figure 6.5: Contours of 95% C.L., yielding an upper bound on the the initial modulus amplitude ϕ_0 , as a function of the modulus mass. QAS data are used for the observed D/H ratio.

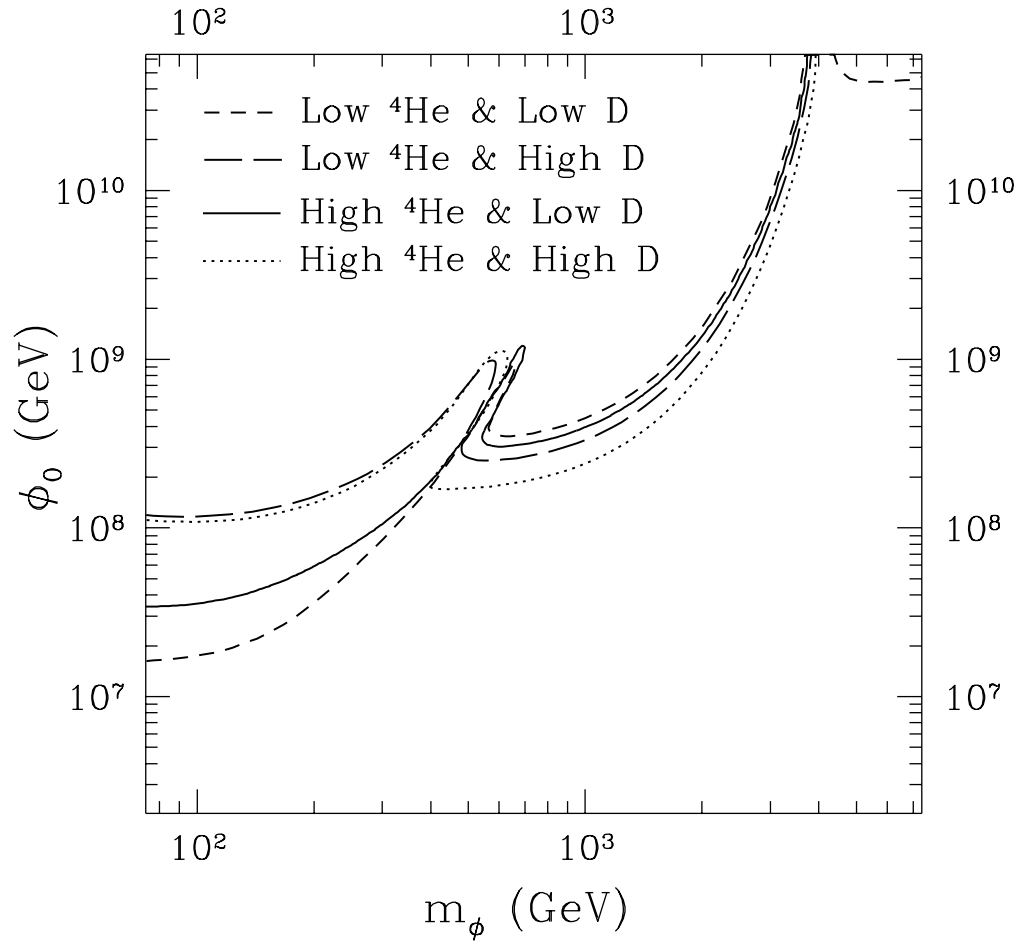
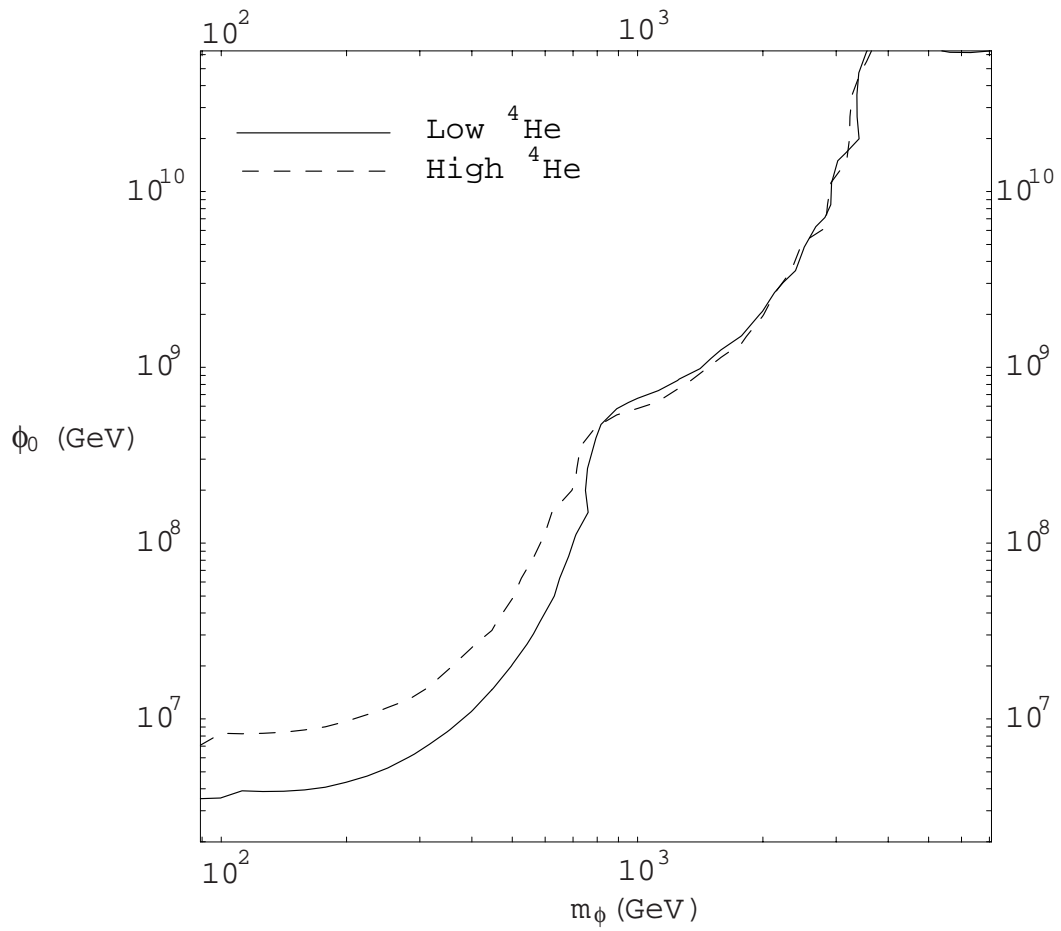


Figure 6.6: Contours of 95% C.L., yielding an upper bound on the the initial modulus amplitude ϕ_0 , as a function of the modulus mass. Proto-solar data are used for the observed D/H and (D+ ^3He)/H ratios.



Chapter 7

Conclusion

I have discussed the photodissociation of light elements due to the radiative decay of a massive particle, and I have shown how I can constrain my model parameters from the observed light-element abundances. I adopted two quasar absorption system (QAS) D/H values, as well as solar-system data for D/H and $^3\text{He}/\text{H}$. For each of these, I have used two ^4He values.

I present my results in terms of the confidence level at which each theoretical parameter set (*i.e.*, the set of properties of a radiatively decaying particle) is excluded by the observed abundances. My algorithm for computing the confidence level is consistent and general enough to apply not only to the scenarios investigated in this work, but also to many other non-standard theories of BBN.

When I adopt the low ^4He and low QAS D/H values, I find that a non-vanishing amount of such a long-lived, massive particle is preferred: $m_X Y_X \gtrsim 10^{-10}$ GeV for $10^4 \text{ sec} \lesssim \tau_X \lesssim 10^6 \text{ sec}$. On the other hand, consistency with the observations imposes upper bounds on $m_X Y_X$ in each of the four QAS cases.

Proto-solar $(\text{D}+^3\text{He})/\text{H}$ and proto-solar $^3\text{He}/\text{H}$ prefer high η , just as low QAS D/H, so these cases (both high and low ^4He) resemble my analyses for low QAS D/H. However, in order to compare these observations to my theoretical calcula-

tion of the primordial light-element abundances, I need to extrapolate the observations back to the primordial abundances. To this end, I use the very general chemical evolution model of Steigman and Tosi [12]. With only a few mild assumptions, I find that for low ^4He , a non-vanishing abundance of long-lived, massive particles is slightly preferred. And in both the high and low ^4He cases, I can impose upper bounds on $m_X Y_X$.

In deriving these results, I have included the uncertainties in the light-element abundances due to the uncertainties in the nuclear reaction rates. To accomplish this, I used two algorithms: Monte-Carlo, and linear propagation of errors. Linear propagation of errors is much faster, and I have demonstrated that it yields results comparable to those of the Monte-Carlo throughout my non-standard BBN parameter space (to within a 16% difference in the error).

Another issue I have investigated is the importance of the correlations between the abundances of various elements, as the reaction rates are varied. Conventional wisdom is that these correlations may be neglected, thus simplifying the calculation. However, it has been pointed out [56] that the correlations between elements can be quite large. To resolve this question for my model, I performed my analysis with and without correlations, and compared the results. I found that correlations can safely be neglected, because they are large only in regions that are excluded by a large disagreement between theory and observation.

I have also studied the photodissociation of ^7Li and ^6Li in this dissertation. These processes do not affect the D/H and ^4He abundances, because $^7\text{Li}/\text{H}$ and

${}^6\text{Li}/\text{H}$ are many orders of magnitude less abundant than D/H and ${}^4\text{He}$. When I examine the region of parameter space where the predicted abundances agree well with the observed ${}^7\text{Li}/\text{H}$, the low ${}^4\text{He}$, and the low QAS D/H or proto-solar $(\text{D}+{}^3\text{He})/\text{H}$ observations, I find that the produced ${}^6\text{Li}/\text{H}$ may be of order 10^{-12} , which is two orders of magnitude larger than the prediction of SBBN (see Figs. 2.5 and 4.4). The predicted ${}^6\text{Li}$ is consistent with the observed upper bound Eq. (3.6) throughout the region of parameter space in which I am interested. Although currently it is believed that the observed ${}^6\text{Li}$ is produced by spallation, my model suggests another origin: the observed ${}^6\text{Li}$ may be produced by the photodissociation of ${}^7\text{Li}$.

Finally, I have discussed candidates for my radiatively decaying particle. My first example is the gravitino. In this case, I can constrain the reheating temperature after inflation, because it determines the abundance of the gravitino. I obtained the stringent bounds $T_R \lesssim 10^8 \text{ GeV} - 10^9 \text{ GeV}$ for $100 \text{ GeV} \lesssim m_{3/2} \lesssim 1 \text{ TeV}$. My second example is the lightest neutralino that is heavier than the gravitino. When the neutralino is the lightest superparticle in the MSSM sector, it can decay into a photon and a gravitino. If I assume the lightest neutralino is pure bino, and its mass is about 100 GeV , then the relic number density of binos is related to the right-handed slepton mass, because binos annihilate mainly through right-handed slepton exchange. For this case, I obtained an upper bound on the gravitino mass, $m_{3/2} \lesssim 700 \text{ MeV} - 4 \text{ GeV}$ for $100 \text{ GeV} \lesssim m_{\tilde{l}_R} \lesssim 1 \text{ TeV}$. My third example is a modulus field. I obtained a severe constraint on its initial amplitude:

$\phi_0 \lesssim 10^8 \text{ GeV} - 10^9 \text{ GeV}$ for $100 \text{ GeV} \lesssim m_{3/2} \lesssim 1 \text{ TeV}$. This bound is well below the Planck scale, so it suggests the need for a dilution mechanism, such as thermal inflation.

Bibliography

- [1] G. Gamow, *Phys. Rev.* **70** (1946) 572; R.A. Alpher, H. Bethe, G. Gamow, *Phys. Rev.* **73** (1948) 803.
- [2] D.J. Fixsen *et al.*, *Astrophys. J* **473** (1996) 576.
- [3] A.G. Kim *et al.*, *Astrophys. J.* **476** (1997) L63.
- [4] Particle Data Group, *The European Physical Journal* **C3** (1998) 1.
- [5] T.P. Walker, G. Steigman, D.N. Schramm, K.A. Olive, and H.-S. Kang, *Astrophys. J.* **376** (1991) 51; Subir Sarkar, *Rept. Prog. Phys.* **59** (1996) 1493, hep-ph/9602260.
- [6] D. Lindley, *Mon. Not. Roy. Astron. Soc.* **188** (1979) 15P; D. Lindley, *Astrophys. J.* **294** (1985) 1.
- [7] H. Pagels and J.R. Primack, *Phys. Rev. Lett.* **48** (1982) 223; S. Weinberg, *Phys. Rev. Lett.* **48** (1982) 1303; L.M. Krauss, *Nucl. Phys.* **B227** (1983) 556; J. Ellis, E. Kim, and D.V. Nanopoulos, *Phys. Lett.* **B145** (1984) 181; R. Juszkiewicz, J. Silk, and A. Stebbins, *Phys. Lett.* **B158** (1985) 463; J. Ellis, E. Kim, and S. Sarkar, *Nucl. Phys.* **B259** (1985) 175; M. Kawasaki and K. Sato, *Phys. Lett.* **B189** (1987) 23; J. Ellis, G.B. Gelmini, J.L. Lopez, D.V. Nanopoulos, and S. Sarkar, *Nucl. Phys.* **B373** (1992) 399; T. Moroi, H. Murayama, and M. Yamaguchi, *Phys. Lett.* **B303** (1993) 289.

- [8] M. Kawasaki and T. Moroi, *Prog. Theor. Phys.* **93** (1995) 879, hep-ph/9403364.
- [9] M. Kawasaki and T. Moroi, *Astrophys. J.* **452** (1995) 506, astro-ph/9412055.
- [10] S. Dimopoulos, R. Esmailzadeh, L.J. Hall, and G.D. Starkman, *Astrophys. J.* **330** (1988) 545; *Nucl. Phys.* **B311** (1989) 699.
- [11] S. Dimopoulos, G. Dvali, R. Rattazzi, and G.F. Giudice, *Nucl. Phys.* **B510** (1998) 12, hep-ph/9705307.
- [12] G. Steigman and M. Tosi, *Astrophys. J.* **B453** (1995) 173.
- [13] S. Weinberg, *Gravitation and Cosmology: Principles and Applications of the General Theory of Relativity* (John Wiley & Sons, New York, 1972).
- [14] E.W. Kolb and M.S. Turner, *The Early Universe* (Addison-Wesley, Redwood City, CA, 1990).
- [15] K. Yamamoto and E. Bunn, *Astrophys. J.* **464** (1996) 8; M. White and D. Scott, *Astrophys. J.* **459** (1996) 415.
- [16] S. Perlmutter *et al.*, *Astrophys. J.* **483** (1997) 565; S. Perlmutter *et al.*, *B.A.A.S.* **29** (1997) 1351, astro-ph/9812473; B.P. Schmidt *et al.*, *Astrophys. J.* **507** (1998) 46, astro-ph/9805200.
- [17] G. Efstathiou *et al.*, to be published in *Mon. Not. R. Astron. Soc.* 7 May 1999, astro-ph/9812226.

- [18] D.R. Tilley, H.R. Weller, and H.H. Hasan, *Nucl. Phys.* **A474** (1987) 1.
- [19] F. Ajzenberg-Selove, *Nucl. Phys.* **A490** (1988) 1.
- [20] F. Ajzenberg-Selove, *Nucl. Phys.* **A506** (1990) 1.
- [21] F. Ajzenberg-Selove, *Nucl. Phys.* **A449** (1986) 1.
- [22] M.S. Smith, L.H. Kawano, and R.A. Malaney, *Astrophys. J. Suppl. Series* **85** (1993) 219.
- [23] R.V. Wagoner, *Astrophys. J. Suppl. Series* **18** (1969) 247.
- [24] R.A. Malaney and W.A. Fowler, *Astrophys. J.* **345** (1989) L5.
- [25] G.R. Caughlan and W.A. Fowler, *Atomic Data and Nuclear Data Tables* **40** (1988) 283.
- [26] L. Kawano, *Let's Go: Early Universe II*, Fermilab preprint Pub-92/04-A (unpublished).
- [27] J. Yang, M.S. Turner, G. Steigman, D.N. Schramm, and K.A. Olive, *Astrophys. J.* **281** (1984) 493.
- [28] R.A. Alpher, J.W. Follin, R.C. Herman, *Phys. Rev.* **92** (1953) 1347.
- [29] F. Hoyle and R.J. Tayler, *Nature* **203** (1964) 1108.
- [30] P.J.E. Peebles, *Astrophys. J.* **146** (1966) 542.
- [31] R.V. Wagoner, J.W. Follin, and F. Hoyle, *Astrophys. J.* **148** (1967) 3.

- [32] A. Yahil and G. Beaudet, *Astrophys. J.* **206** (1976) 26; B.V. Vainer, *et al.*, *Sov. Astron.* **22** (1976) 1; Y. David and H. Reeves, in *Physical Cosmology*, eds., R. Bailin, J. Audouze, and D.N. Schramm (North-Holland, Amsterdam, 1980); N. Terasawa and K. Sato, *Astrophys. J.* **294** (1985) 9.
- [33] R.V. Wagoner, *Astrophys. J.* **179** (1973) 343.
- [34] D.A. Dicus, *et al.*, *Phys. Rev.* **D26** (1982) 2694.
- [35] E. Holtmann, M. Kawasaki, K. Kohri, and T. Moroi, to be published in *Phys. Rev. D.*, hep-ph/9805405.
- [36] N. Hata, R.J. Scherrer, G. Steigman, D. Thomas, T.P. Walker, S. Bludman, and P. Langacker, *Phys. Rev. Lett.* **75** (1995) 3977, hep-ph/9505319.
- [37] K. Kohri, M. Kawasaki, and K. Sato, *Astrophys. J.* **490** (1997) 72, astro-ph/9612237.
- [38] M. Kawasaki, K. Kohri, and K. Sato, *Phys. Lett.* **B430** (1998) 132, astro-ph/9705148.
- [39] E. Holtmann, M. Kawasaki, and T. Moroi, *Phys. Rev. Lett.* **77** (1996) 3712, hep-ph/9603241.
- [40] B.E.J. Pagel *et al.*, *Mon. Not. R. Astron. Soc.* **255** (1992) 325.
- [41] K.A. Olive, G. Steigman, and E.D. Skillman, *Astrophys. J.* **483** (1997) 788.
- [42] Y.I. Izotov, T.X. Thuan, and V.A. Lipovetsky, *Astrophys. J.*, **435** (1994) 647.

- [43] T.X. Thuan and Y.I. Izotov, in *Primordial Nuclei and their Galactic Evolution*, edited by N. Prantzos, M. Tosi, and R. von Steiger (Kluwer Academic Publications, Dordrecht, 1998) in press.
- [44] Y.I. Izotov, T.X. Thuan, and V.A. Lipovetsky, *Astrophys. J. Suppl. Series*, **108** (1997) 1.
- [45] P.J. Kernan and S. Sarkar, *Phys. Rev.* **D54** (1996) R3681, astro-ph/960304.
- [46] A.A. Zdziarski, *Astrophys. J.* **335** (1988) 786; R. Svensson and A.A. Zdziarski, *Astrophys. J.* **349** (1990) 415.
- [47] R.D. Evans, *The Atomic Nucleus* (McGraw-Hill, New York, 1955).
- [48] R. Pfeiffer, *Z. Phys.* **208** (1968) 129.
- [49] D.D. Faul, B.L. Berman, P. Mayer, and D.L. Olson, *Phys. Rev. Lett.* **44** (1980) 129.
- [50] A.N. Gorbunov and A.T. Varfolomeev, *Phys. Lett.* **11** (1964) 137.
- [51] J.D. Irish, R.G. Johnson, B.L. Berman, B.J. Thomas, K.G. McNeill, and J.W. Jury, *Can. J. Phys.* **53** (1975) 802.
- [52] C.K. Malcom, D.V. Webb, Y.M. Shin, and D.M. Skopik, *Phys. Lett.* **B47** (1973) 433.
- [53] Yu.M. Arkatov, P.I. Vatset, V.I. Voloshchuk, V.A. Zolenko, I.M. Prokhorets, and V.I. Chimil', *Sov. J. Nucl. Phys.* **19** (1974) 598.

- [54] B.L. Berman, *Atomic Data and Nuclear Data Tables* **15** (1975) 319.
- [55] R.E. Lopez and M.S. Turner, submitted to *Phys. Rev. D*, astro-ph/9807279.
- [56] P.J. Kernan and L.M. Krauss, *Phys. Rev. Lett.* **72** (1994) 3309, astro-ph/9402010.
- [57] G. Fiorentini, E. Lisi, S. Sarkar, and F. L. Villante, astro-ph/9803177.
- [58] A.D. Dolgov and B.E.J. Pagel, astro-ph/9711202; K. Jedamzik and G.M. Fuller, *Astrophys. J.*, **452** (1995) 33.
- [59] J. Lòpez-Suàrez and R. Canal, submitted to *Astrophys. J. Lett.*, astro-ph/9804235.
- [60] A. Songaila, L.L. Cowie, C.J. Hogan, and M. Rugers, *Nature* **368** (1994) 599.
- [61] R.F. Carswell, M. Rauch, R.J. Weymann, A.J. Cooke, and J.K. Webb, *Mon. Not. Roy. Astron. Soc.* **268** (1994) L1.
- [62] M. Rugers and C.J. Hogan, *Astrophys. J., Lett.* **459** (1996) L1.
- [63] M. Rugers and C.J. Hogan, *Astron. J.* **111** (1996) 2135, astro-ph/9603084; J. K. Webb *et al.*, *Nature* **388** (1997) 250; D. Tytler, S. Burles, L. Lu, X.-M. Fan, and A. Wolfe, astro-ph/9810217.
- [64] R.F. Carswell, J.K. Webb, K.M. Lanzetta, *et al. Mon. Not. Roy. Astron. Soc.* **278** (1996) 506; M. Rugers and C. Hogan, *Astr. Soc. of the Pacific Conf. Series*

- 99** (1996) 100; E.J. Wampler, G.M. Williger, J.A. Baldwin, R.F. Carswell, C. Hazard, and R.G. McMahon *Astronomy and Astrophysics* **316** (1996) 33.
- [65] G. Steigman, in *Light Element Abundances. Proceedings of an ESO/EIPC Workshop*, edited by P. Crane, (Springer, Berlin, Germany, 1995), astro-ph/9410060.
- [66] D. Tytler, S. Burles, and D. Kirkman, submitted to *Astrophys. J.*, astro-ph/9612121.
- [67] D. Tytler, X.-M. Fan, and S. Burles, *Nature* **381** (1996) 207, astro-ph/9603069; S. Burles and D. Tytler, submitted to *Science*, astro-ph/9603070.
- [68] E.J. Wampler, *Nature* **383** (1996) 308.
- [69] A. Songaila, E.J. Wampler, and L.L. Cowie, *Nature* **385** (1997) 137, astro-ph/9611143.
- [70] S. Burles and D. Tytler, submitted to *Astrophys. J.*, astro-ph/9712109.
- [71] F. Spite and M. Spite, *Astronomy and Astrophysics* **115** (1982), 357.
- [72] P. Bonifacio and P. Molaro, *Mon. Not. Roy. Astron. Soc.* **285** (1997) 847.
- [73] C.J. Hogan, astro-ph/9609138.
- [74] B.D. Fields, K. Kainulainen, K.A. Olive, and D. Thomas, *New Astron.* **1** (1996) 77, astro-ph/9603009.

- [75] L.M. Hobbs and J.A. Thorburn, *Astrophys. J.* **491** (1997) 772.
- [76] V.V. Smith, D.L. Lambert, and P.E. Nissen, *Astrophys. J.* **408** (1993) 262.
- [77] W. Hu and J. Silk, *Phys. Rev. Lett.* **70** (1993) 2661.
- [78] A.P. Lightman, *Astrophys. J.* **244** (1981) 392.
- [79] J. Gratsias, R.J. Scherrer, and D.N. Spergel, *Phys. Lett.* **B262** (1991) 298;
M. Kawasaki and T. Moroi, *Phys. Lett.* **B346** (1995) 27, hep-ph/9408321.
- [80] D. Gautier and P. Morel, *Astronomy and Astrophysics* **B323** (1997) L9.
- [81] Turck-Chièze, S. Cahen, M. Cassé, and C. Doom *Astrophys. J.* **B335** (1988)
415.
- [82] J. Geiss, in *Origin and Evolution of the Elements*, edited by N. Prantzos,
E. Vangioni-Flam, and M. Cassé (Cambridge University Press, Cambridge,
1993).
- [83] J.L. Linsky *et al.*, *Astrophys. J.* **402** (1993) 694; P.R. McCullough, *Astrophys.*
J. **390** (1992) 213.
- [84] N. Hata, R.J. Scherrer, G. Steigman, D. Thomas, and T.P. Walker, *Astrophys.*
J. **458** (1996) 637, hep-ph/9412087.
- [85] G. Steigman and M. Tosi, *Astrophys. J.* **B401** (1992) 150.
- [86] D. Bailin and A. Love, *Supersymmetric Gauge Field Theory and String The-*
ory (Institute of Physics Publishing, Bristol, UK, 1994).

- [87] T. Moroi, *Effects of the Gravitino on the Inflationary Universe* (Ph.D. Thesis, Tohoku University, Japan, 1995), hep-ph/9503210.
- [88] K.A. Olive and M. Srednicki, *Phys. Lett.* **B230** (1989) 78.
- [89] B. de Carlos, J.A. Casas, F. Quevedo, and E. Roulet, *Phys. Lett.* **B318** (1993) 447, hep-ph/9308325.
- [90] D.H. Lyth and E.D. Stewart, *Phys. Rev. Lett.* **75** (1995) 201, hep-ph/9502417; *Phys. Rev.* **D53** (1996) 1784, hep-ph/9510204.